



저작자표시-비영리-변경금지 2.0 대한민국

이용자는 아래의 조건을 따르는 경우에 한하여 자유롭게

- 이 저작물을 복제, 배포, 전송, 전시, 공연 및 방송할 수 있습니다.

다음과 같은 조건을 따라야 합니다:



저작자표시. 귀하는 원저작자를 표시하여야 합니다.



비영리. 귀하는 이 저작물을 영리 목적으로 이용할 수 없습니다.



변경금지. 귀하는 이 저작물을 개작, 변형 또는 가공할 수 없습니다.

- 귀하는, 이 저작물의 재이용이나 배포의 경우, 이 저작물에 적용된 이용허락조건을 명확하게 나타내어야 합니다.
- 저작권자로부터 별도의 허가를 받으면 이러한 조건들은 적용되지 않습니다.

저작권법에 따른 이용자의 권리는 위의 내용에 의하여 영향을 받지 않습니다.

이것은 [이용허락규약\(Legal Code\)](#)을 이해하기 쉽게 요약한 것입니다.

[Disclaimer](#)

공학박사 학위논문

Development and Characterization of Powder Metallurgically Produced Chromium-Tungsten Dual-Phase Composites

분말야금학적으로 제조된 크롬-텅스텐 이상
복합재료의 개발 및 분석

2021 년 8 월

서울대학교 대학원

재료공학부

곽 노 준 (郭 魯 俊)

Development and Characterization of Powder Metallurgically Produced Chromium-Tungsten Dual-Phase Composites

지도 교수 한 홍 남

이 논문을 공학박사 학위논문으로 제출함

2021 년 8 월

서울대학교 대학원

재료공학부

곽 노 준

곽노준의 공학박사 학위논문을 인준함

2021 년 8 월

위 원 장	_____	홍 성 현
부위원장	_____	한 홍 남
위 원	_____	최 인 석
위 원	_____	김 형 찬
위 원	_____	유 정 하

ABSTRACT

In future fusion reactors, tungsten (W) is a favored candidate material for plasma-facing components (PFCs) due to an excellent combination of properties such as high hardness and excellent abrasion resistance at high temperatures. However, owing to the high ductile-brittle transition temperatures (DBTT), its inherent brittleness and the subsequent lack of damage tolerance strongly restrict the application in the extreme fusion environment. To overcome this drawback, the demand for research on structural design and the development of new composite and/or alloy material have been continuously increased. Despite such research efforts, the severe brittleness of W is still being a problem. Recently, due to the relatively low DBTT, studies for applying chromium (Cr), which shows a significant ductile behavior even at low temperature regions, and have advantages such as excellent corrosion resistance and low neutron activation, are attracting great attention as a plasma facing material (PFM). However, its low strength at high temperature limits the use of Cr in actual working environments. In this study, using above two materials, a new concept of chromium-tungsten (Cr-W) dual-phase composites was developed and proposed. In addition, the mechanical properties and deuterium resistance were evaluated to confirm the applicability as a PFM. Moreover, an issue that carbides generated inside the material due to the carbon (C) diffusion, which deteriorates the mechanical and deuterium resistance properties of the material, should be solved.

Firstly, the diffusion of C occurring during material production was suppressed. In general, high melting point materials such as W (3422 °C) and Cr (1907 °C) are fabricated using powder metallurgy to obtain a dense microstructure with desired properties. Spark plasma sintering (SPS), an effective powder metallurgy technique that can fabricate bulk samples with high density in a short time by directly applying a pulsed current along mechanical pressure, is used as the main production process. However, since a powder compact to be sintered is placed in a graphite mold (die and punches), the C uptake cannot be avoided during the production. What is noteworthy here is that W and Cr are strong carbide-forming elements. The inevitable C absorption during the SPS induces carbide segregation at the grain

boundaries of W and Cr, thereby reducing the ductility and leading to a brittle intergranular fracture. In order to solve this problem, W, molybdenum (Mo), and tantalum (Ta) foils were used as a C diffusion barrier of the sintered W. In particular, it was confirmed that the Ta foil can effectively suppress the C diffusion into W, while Mo foil is not an effective diffusion barrier. Thermodynamic-kinetic simulations demonstrate that the suppressed C diffusion in Ta is attributed to high solubility and low diffusivity. Furthermore, the thermodynamically stable Ta carbide prevents further C diffusion at the Ta/W interface. For the opposite reason, C diffuses faster not only in the Mo, but also at the Mo/W interface. The introduction of W foil only acts as a physical barrier for C diffusion, confirming that the effect was insufficient.

Secondly, the fabrication of Cr-W of dual-phase composites was performed. For the fabrication of Cr-W of dual-phase composites, two different powders were mixed using a high-energy mill and sintered. The developed composite material exhibits a unique microstructure in which coarse Cr particles are surrounded by a three-dimensional and continuously connected ultrafine-grained W network. In order to optimize the sintering condition, the effect of sintering variables such as sintering temperature, time, process, and powder conditions was explored. With that, it was confirmed that the high density can be achievable sintered at 1300 °C in the composition of Cr-10 vol.% W and Cr-20 vol.% W. Considering the sintering temperature of W is over 1700 °C, we could deduce that the sinterability of the W phase of the Cr-W dual-phase composites was significantly improved at a relatively low temperature. In order to investigate the evolution of this unique microstructure and the mechanism for improving sinterability, phase diagram and kinetic analysis were performed together with the results of electron microscopy and x-ray diffraction analysis. The accelerated sintering of Cr-W dual-phase composites is found to be due to the Cr diffusion in W during sintering process.

Thirdly, the properties of Cr-W dual-phase composites were characterized. In order to characterize the potential applicability of the Cr-W dual-phase composites developed in this study, mechanical properties and deuterium (D) retention behaviors were evaluated. In all experiments, pure Cr and W were compared together with the Cr-W dual-phase composites. A three-point bending tester was used to evaluate the mechanical properties, confirming that there is a possibility of improving mechanical

properties according to the strengthening effect of the W phase and the deformation dominated by the Cr phase near the DBTT of Cr (300 °C). In general, in order to be used as a low-radiation material in a nuclear fusion environment, it should have excellent D retention resistance. And since such retention behaviors can be further accelerated due to nano-defects generated during neutron irradiation, they must be evaluated before the use of the materials in actual working environments. In this study, D ions were exposed using plasma and ion source devices, and the amount of deuterium retention on the surface and the entire sample was quantified to understand diffusion behavior of D in material. In the Cr-W dual-phase composites, it was confirmed that the high thermodynamic stability of D with the Cr phase and the slow diffusion of deuterium in the W phase could have a significant effect on reducing the amount of D retention. In addition, this concept would also valid when the defect density on the surface is increased by pre-irradiation with neutron-like ions (W^{6+} ions), where a lower amount of deuterium retention than pure Cr and W is observed.

From this study, for the first time, Cr-W dual-phase composites, which can be proposed as a plasma facing material for a next-generation fusion reactor, was developed. The comprehensive research and microstructure design strategy for the material are expected to provide guidelines for the development of new material concepts along with securing potential properties. In addition, this study provides strategies to minimize the C diffusion during SPS as well as an intuition into developing structural materials for extreme carbonaceous environments. Finally, it is believed that this research will provide breakthrough in the field of materials for various extreme environments and to open up new field in the material development.

Keywords : Cr-W dual-phase composites, spark plasma sintering, diffusion, carbon, microstructure, mechanical properties, deuterium retention

Student Number : 2015-20798

CONTENTS

ABSTRACT	i
TABLE OF CONTENTS	iii
LIST OF FIGURES	vii
LIST OF TABLES	x
Chapter 1. Introduction	1
1.1 Fusion reactor and divertor	1
1.2 Issues in tungsten materials	6
1.3 Chromium-based materials for fusion application	8
1.4 Spark plasma sintering	9
1.5 Research objectives and structure of thesis	11
1.6 References	13
Chapter 2. Metallic foils as a C diffusion barrier	19
2.1 Introduction	19
2.2 Experimental procedures	20
2.2.1 Materials and methods	20
2.2.2 Characterization	21
2.3 Results and discussion	24
2.3.1 The effect of protective foils in W powders	24
2.3.2 Understanding of C diffusion in W through thermodynamic and kinetic data	

-----	31
2.3.3 The prediction of C diffusion by DICTRA simulation -----	35
2.3.4 The application to the Cr powders-----	37
2.4 Conclusions-----	40
2.5 References-----	41
Chapter 3. Fabrication of Cr-W Dual-Phase Composites-----	45
3.1 Introduction -----	45
3.2 Experimental procedures-----	47
3.2.1 Materials and methods-----	47
3.2.2 Characterization-----	48
3.3 Results and discussion-----	50
3.3.1 The powder size and milling times-----	50
3.3.2 The optimization of sintering temperature and W addition level -----	54
3.3.3 Initial microstructures and basic properties-----	60
3.3.4 Cr/W interface characterization-----	64
3.3.5 Sintering kinetics-----	67
3.4 Conclusions-----	72
3.5 References-----	73
Chapter 4. Characterization of Cr-W Dual-Phase Composites-----	75
4.1 Introduction -----	75
4.2 Experimental procedures-----	77
4.2.1 Materials and methods-----	77

4.2.1.1 Mechanical test (3-point bending test)-----	77
4.2.1.2 Deuterium retention behaviors-----	79
4.2.2 Characterization-----	83
4.2.2.1 Mechanical test (3-point bending test)-----	83
4.2.2.2 Deuterium retention behaviors-----	84
4.3 Results and discussion-----	86
4.3.1 Mechanical test (3-point bending test)-----	86
4.3.2 Deuterium retention behaviors-----	97
4.4 Conclusions-----	108
4.5 References-----	109
Chapter 5. Conclusions and Outlook-----	112
국문초록-----	114

LIST OF FIGURES

Figure 1 (a) ITER Tokamak cutaway (The dashed brown line indicates divertor area and is enlarged next to it) [25], (b) a typical mock-up type divertor component in ITER Tokamak fusion reactor.

Figure 2 (a) Schematic diagram of SPS system [49]; (b) The image for consolidation of powder in graphite mold during SPS

Figure 3 Variation of Gibbs free energy (ΔG) as a function of temperature for possible reactions during the sintering of the system.

Figure 4 Schematic illustration of graphite mold assembly used in SPS for (a) without a C diffusion barrier and (b) with W, Ta, or Mo as a C diffusion barrier. The sintered sample is cylindrical and (c) the microstructure is observed with the view in the AD of the cylindrical surface.

Figure 5 Cross-sectional SEM images of SPSed W samples with the view of the AD of cylindrical surface. The diffusion of C begins with the cylindrical surface and extends inside the samples, its direction is indicated by the black arrows, and the green dashed lines denote the region of direct contact with C: (a–c) W-C, (d–f) W-W-C, (g–i) W-Mo-C, and (j–l) W-Ta-C systems. Sintering temperatures of (a), (d), (g), (j) = 1700 °C ; (b), (e), (h), (k) = 1800 °C; (c), (f), (i), (l) = 1900 °C, and the dwell time = 10 min for all. The subsurfaces of the SPSed W affected by C flux are lined by white and green dashed lines for (a–c) and white and yellow dashed lines for (d–i), respectively. The original metallic foil regions are covered by yellow and green dashed lines for (d–l). The red squares of A and B in (g) show microstructural development in Ta foil during sintering (indicated by yellow, blue, and white arrows).

Figure 6 SEM images (up) and EPMA elemental mappings (down) of the W samples sintered at 1700 °C for 10 min. with the view in the AD of cylindrical surface: (a), (e) W-C, (b), (f) W-W-C, (c), (g) W-Mo-C, and (d), (h) W-Ta-C systems. Black arrows indicate the direction of C diffusion. In (a–d), the red squares denote EPMA map zones and various points (1 to 14) marked by orange circles indicate local regions distinguished by different phases. Local chemical compositions at various points are shown in Table 1.

Figure 7 Calculated ternary phase diagram using Thermo-Calc® (TCFE9 database): isothermal section of (a) W-Mo-C and (b) W-Ta-C system at 1700 °C.

Figure 8 Diffusivity of C in metal (a) and carbide (b) in the system as a function of temperature. All data are from previous reports. The semi-transparent green, red, and blue areas represent C diffusivity in Mo and its carbides, Ta and its carbides, and W and its carbides, respectively. The corresponding area highlighted by semi-transparent grey indicate C diffusivity in WC.

Figure 9 The C solubility curves of elements (Mo, Ta, and W) in the system as a function of temperature with the use of Thermo-Calc software (TCFE9 database).

Figure 10 DICTRA prediction of concentration profiles of depth by C diffusion: (a–d) W-Mo-C, and (e–h) W-Ta-C systems. The profiles are representative snapshots of specific times

(1, 50, 100, and 600 s)

Figure 11 SEM images (a, b) and EPMA elemental mappings (c, d) of the Cr samples sintered at 1300 °C for 10 min. with the view in the AD of cylindrical surface: (a), (c) Cr-C, (b), (d) Cr-Ta-C systems. Black arrows indicate the direction of C diffusion. In (a, b), the red squares denote EPMA map zones and various points (1 to 6) marked by orange circles indicate local regions distinguished by different phases. Local chemical compositions at various points are shown in Table 2.

Figure 12 The densification enhanced zones depending on the W powder size. (a) with 0.5 μm , (b) with 2.4 μm , and (c) with 8 μm . Yellow areas indicated diffusion enhanced zones in W.

Figure 13 Powder morphology evolution during mechanical milling. As-received (a) Cr powder and (b) W powder and mechanically milled at (c) 1 h, (d) 5 h, (e) 10 h, and (f) 20 h.

Figure 14 The Cr diffusion distances in W depending on different sintering temperatures. (a), (d) 1100 °C, (b), (e) 1200 °C, and (c), (f) 1300 °C.

Figure 15 XRD patterns of Cr-W composite with different sintering temperature.

Figure 16 SEM-EDS mapping results. Sintered at (a) 1300 °C, (b) 1500 °C.

Figure 17 Powder size distribution of as-received Cr powder.

Figure 18 SEM+EBSD IPF maps and corresponding grain size and hardness maps of each phase for the bulk samples: (a, e) Cr; (b, f) Cr-10W; (c, g) Cr-20W and (d, h) W. (i) EBSD IPF map of the Cr/W interface region in the Cr-20W sample. (j) Grain sizes and hardness ($HV_{0.1}$) of W and Cr each phase with respect to composition. Orange arrows in (a) indicates micron-sized pores.

Figure 19 (a) Density and (b) Hardness of the bulk specimens

Figure 20 STEM-HAADF Images of Cr-20W interface are shown in (a) and corresponding diffraction patterns of different area 1 and 2 are shown in (b) and (c). EDS Line scan and mapping marked by yellow line and red box in (a) are shown in (d) and (e), respectively.

Figure 21 (a) W-Cr phase diagram, (b) The solubility of Cr in W and W in Cr. The solubility on Cr in W at 1300 °C is approximately 18.6 at. %.

Figure 22 (a) Shrinkage curves of sintered compact and graphite during SPS. The actual shrinkage curve is obtained by subtracting graphite expansion from total shrinkage curve. (b) Evolution of relative density as a function of temperature for Cr, Cr-10W, Cr-20W, and W. (c) The mean residual squares as function of sintering activation energy. (d) normalized heating profiles at the best convergence activation energy denoted in (c).

Figure 23 The concept of applying Cr-based materials to the middle heat flux region of mock-up

Figure 24 (a) Three-point bending test configuration with the specimen on it; (b) Schematics

of the bending configuration and geometry with size.

Figure 25 Sputtering yields of W and Cr for D calculated by the SDTrimSP simulations.

Figure 26 Experimental strategy for deuterium exposures.

Figure 27 Flexural stress-strain curves obtained from 3PB test at (a) RT and (b) 300 °C. For each condition, at least more than three samples were tested.

Figure 28 SEM images of crack propagation for (a, b) and of fracture surfaces for (c, d). All samples are pure Cr and tested at RT. Green dotted lines indicate nano to micron-sized pores.

Figure 30 SEM images of crack propagation for (a, b) and of fracture surfaces for (c, d). All samples are Cr-10W and tested at RT.

Figure 31 SEM images of crack propagation for (a, b) and of fracture surfaces for (c, d). All samples are Cr-20W and tested at RT.

Figure 32 SEM images of crack propagation for (a, b) and of fracture surfaces for (c, d). All samples are Cr-10W and tested at 300 °C. Green arrow indicates the deformed region in Cr and Red dotted line indicates river pattern.

Figure 33 SEM images of crack propagation for (a, b) and of fracture surfaces for (c, d). All samples are Cr-20W and tested at 300 °C. Green arrows indicate the deformed region in Cr.

Figure 34 Strategy for the microstructures and corresponding mechanical properties.

Figure 35 SEM images for before and after D exposures. (a, d, g) initial microstructures of W, Cr, and Cr-20W. (b, e, h) after D exposures with 200eV/D energy. (c, f, i) after D exposures with 10 eV/D energy. All bottom left images displaced in the inset is CLSM images.

Figure 36 SEM images and EDS elemental mapping of the Cr-20W interface after D exposures. Yellow inset indicates enlarged area of white ash-like area. Cross-sectional SEM images are shown in (b, c).

Figure 37 D concentration depth profiles for undamaged samples of (a) 200 eV/D and (b) 10 eV/D for damaged samples of (c) 10 eV/D. TDS Spectra of D desorption flux from D₂ and HD signals for undamaged samples of (d) 200 eV/D and (e) 10 eV/D for damaged samples of (f) 10 eV/D.

Figure 38 D retention measured by NRA and TDS. The surface of D inventory was obtained by the NRA analysis, while the bulk of D inventory was obtained by subtracting the surface of D inventory from the total D inventory measured by TDS.

LIST OF TABLES

Table 1 Local chemical compositions (at.%) of W system at various points (1 to 14) indicated in Figure 6 (a–d) to identify the different phases after sintering at 1700 °C for 10 min.

Table 2 Local chemical compositions (at.%) of Cr systems at various points (1 to 6) indicated in Figure 11 (a–b) to identify the different phases after sintering at 1300 °C for 10 min.

Table 3 Activation energies obtained by MSC curves (up) and references (down).

Table 4 The activation energies for heat of solution, diffusion, and solubility of hydrogen in W and Cr.

Chapter 1. Introduction

1.1. Fusion reactor and divertor

While global energy consumption is growing up every year, the fossil fuel keeps being depleted during the recent decades [1]. However, consistent energy supply is one of the most important prerequisites for human life and development. To secure sustainable energy that meets our today's and future's demand, several attempts have been made to release energy through new energy sources. Among those, nuclear fusion energy is one of the most attractive solution to solve energy shortage issue [2, 3]. As a promising new energy source, the potential advantages of nuclear fusion energy are manifold, as it represents a long-term, sustainable, economical, and safe energy source for electricity generation. What is more, fuels are inexpensive and abundant in nature, and the amount of long-lived radioactive waste and greenhouse gases produced through fusion are minimal.

Nuclear fusion is the fusing of atomic nuclei which have a positive electric charge. In order to bond with other nuclei to form a new nucleus, the electric repulsive must be overcome. This only happens if a large number of atomic nuclei collide at high speed at very high temperatures. These conditions are found in the interior of the sun. Among many combinations of fusing reaction, recent research focuses on the fusing of deuterium ($D = {}^2_1\text{H}$) and tritium ($T = {}^3_1\text{H}$), which conditions of the fusion reaction are easier to realize than those required for other reacting agents [1, 3]. Deuterium is stable isotopes of hydrogen which can be extracted from the sea water and tritium is radioactive isotope of hydrogen (a half-life of 12.33 year) which should be artificially produced from the Li. The fusion of a deuteron (the nucleus of a deuterium atom) and a triton (the nucleus of a tritium atom) forms a helium nucleus and a neutron. In a nuclear fusion reactor, the difference in mass has been converted into the kinetic energy of final products (helium nuclei and neutrons) in accordance with Einstein's relationship ($\Delta E = \Delta mc^2$), where m is the increased relativistic mass, c is the speed of light, and E is the kinetic energy, generating electrical energy. The fusion reaction is as follows:



In order for a fusion reaction to take place, the plasma must be heated to a temperature of at least 100 million degrees.

A plasma at this high temperature would

- damage the walls of the plasma chamber, and
- too much energy would be lost through reactions with walls.

For this reason, the plasma is locked into a “magnetic cage”, and thus thermally insulated from the surrounding materials [1]. Power output is generated by fast neutrons and highly energetic particles impacting the walls. The heat produced and transferred to the blanket structures by the reaction neutron is then removed by coolant which, in turn, produce steam and the electrical energy by the way of turbines and generators. There are several concepts that a magnetic field produced inside the coil contain the plasma. Among these concepts, the tokamak (toroidal chamber with magnetic coils) is one of the most studied candidates as a magnetic confinement device for producing controlled thermonuclear fusion power [4]. The international thermonuclear experimental reactor (ITER) is an experimental tokamak reactor that is due to be built since 2008. The ITER project, the next step device, is currently under construction in collaboration with the EU, China, India, South Korea, Russia, Japan, and US, and aims to produce 10 times more output power than input power consumed. At the same time, an International Fusion Material Irradiation Facility (IFMIF) is being constructed and operated to qualify the structural materials required for the DEMOnstration power plant (DEMO) which will be ITER’s successor [5]. DEMO, the first fusion device to export electricity from fusion, will confirm the technological feasibility of fusion power and demonstrate its commercial viability to enable the rapid realization of a nuclear fusion reactor [6, 7].

Although the magnetic confinement minimizes the interaction of hot plasmas with the material surroundings, the plasma-material interactions cannot be completely avoided. In addition, neutrons can escape magnetic confinement, and then induce the damage and degradation of materials. The impurities in a burning plasma including helium the so-called “fusion ash” should also be removed from the plasma core [8]. All these missions can be solved by the device within a tokamak, called a divertor. The divertor is a key main in-vessel component that protects the

vessel from particles out of the plasma and, conversely, the plasma from impurities out of the wall. A special magnetic field directs the outer boundary layer of the plasma (particles and energy) towards specially equipped areas of the vessel wall, namely the divertor plates. It is thus possible to remove the disturbing impurities from the plasma. This secures good thermal insulation of the main plasma by preventing damage and degradation of the vessel wall.

Ever since Axially Symmetric Divertor Experiment (ASDEX), the first divertor tokamak, was first operated by the Max Planck Institute for Plasma Physics in Garching, as early as 1980, steady effort have been devoted toward developing the divertor [8]. Then, ITER divertor, next step device, has been successfully developed in terms of the design and technology [9]. However, its applicability for a DEMO is not necessarily assured yet because the materials performance from plasma expected for the DEMO divertor will be by at least an order of magnitude higher than that of the ITER divertor. Therefore, there still needs to break through many issues to realize the fusion technology. [4, 10–15]. In addition to plasma physics related issues, one of the topics that should be overcome is the material issues related to the first wall and divertor surfaces caused by power and particle exhaust of a fusion.

The material that should directly withstand the hot plasma is called plasma-facing materials (PFMs). PFMs require advanced capabilities such as mechanical strength and thermal properties of materials in extreme environments.

The main requirements that divertor should meet are:

- (a) the ability to withstand a peak thermal load of at least 10 MW/m^2 ;
- (b) the thermal stresses limitation due to modular design;
- (c) the realization of a heat conduction path between the plasma-facing surface and the cooling surface as short as possible;
- (d) a heat transfer coefficient between the cooling side and plasma side structure greater than $30 \text{ kW}/(\text{m}^2 \cdot \text{K})$;
- (e) a high lifetime due to erosion [7, 16].

As higher radiation doses and longer loading scenarios are expected, the requirements for a DEMO will be even greater [17]. In addition to higher radiation

doses, commercial reactor has more stringent requirements compared to DEMO as they require a longer run time and the longest possible maintenance intervals. Selecting a suitable material for the divertor is a special challenge due to the high heat load, which is why intensive work is being done on new and further development of existing material concepts [18–24].

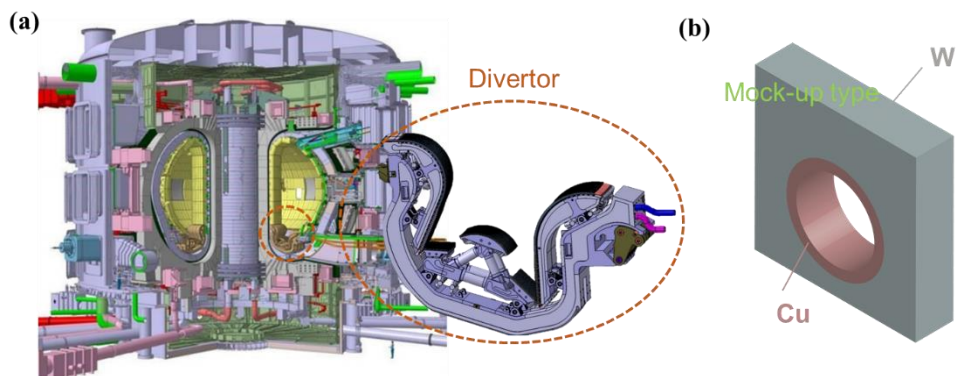


Figure 1 (a) ITER Tokamak cutaway (The dashed brown line indicates divertor area and is enlarged next to it) [25], (b) a typical mock-up type divertor component in ITER Tokamak fusion reactor.

1.2. Issues in tungsten materials

Tungsten (W) and W-based materials have been the main subject of interests and focus of research programs for fusion applications because of their good thermomechanical and thermophysical properties. They satisfy several requirements for PFMs, such as a high melting point, high creep-resistance, high thermal stress resistance, good thermal conductivity, low vapor pressure, good sputtering properties, and good erosion resistance [26]. However, they should also have faced the great challenge to solve inherent drawbacks such as low fracture toughness and a high ductile-to-brittle transition temperature (DBTT), as well as recrystallization embrittlement [27, 28]. For these reasons, W will behave in a brittle manner when the application temperature is lower than the DBTT, showing less resistance to pre-cracking or surface damage [28, 29]. The brittle behavior can be a limiting factor when operating any tungsten-based PFMs in a tokamak [30]. To prevent crack propagation, a relatively high ductility/toughness is a critical requirement.

For a DEMO reactor, it has been predicted that neutron damage levels in a PFC material in the divertor region could reach the values up to 6–7 dpa/fpy [6, 31] or 0.7–1.6 dpa/fpy based on [32]. These doses may probably be high enough to cause a significant degradation of material properties. Therefore, the prime requirements for the materials of highly loaded PFCs are a high thermal conductivity (174 W/(m·K), between copper 401 W/(m·K) and steel ~43 W/(m·K)), a low sputtering yield, and sufficient mechanical properties even under neutron irradiation.

According to the literature [33], the DBTT of tungsten shifts to nearly 650 K at a moderate neutron fluence of 1. When further recrystallization occurs, the tungsten components hardly withstand structural load at temperatures of several hundred degrees. For a typical mono-block [34, 35], only the top part of an exposed mono-block is within the allowable temperature range due to the actively cooling system. [36]. This means that tungsten in the cooling solution temperature range is normally brittle. With that, once the crack initiates, it can easily propagate through the entire armor block from surface to cooling pipe. Failures of component usually occur suddenly and catastrophically without significant damage or warning, and has little residual load-bearing capacity. Hence, structures that satisfy a visual inspection may

fail suddenly at loads much lower than expected.

1.3. Chromium-based materials for fusion application

Chromium (Cr), listed in same group VI with W, has also the body centered cubic-(BCC) lattice structure. Cr and Cr-based alloys have been studied for decades as candidates for high-temperature applications in jet engines [37, 38] and in plasma facing components of the fusion reactor vessel [39, 40]. Cr exhibits a number of good properties such as high strength-to-density ratio, high melting point (being 1907 °C [41]), as well as an excellent corrosion resistance [42, 43], which makes it potential candidate for the application in the plasma facing components. Due to the protective Cr_2O_3 layer which remains stable up to 1400 °C, the material is extremely resistant to environmental corrosion. According to the neutronic calculations, an application of Cr is also favorable from the viewpoint of the neutron irradiation activation, and plasma-facing components for fusion reactor made of Cr can already be classified as low-level waste after 50 years of cooling [40, 44].

Despite the above attractive features, an application of Cr has several challenges that need to be overcome before it can be considered as the material for divertor application. First, the low hardness and the low strength at high temperatures should be strengthened for the thermal stress resistance. Second, the tritium retention behaviors need to be explored which has never been studied yet, e.g., the reasonable amount of hydrogen isotope should be retained. This can also be very important since the tritium retention is more accelerated after the impact of 14 MeV neutrons on the materials, which is caused by a lot of hydrogen trapping sites due to the defect generation [45]. Third, there needs the solution of harsh erosion by intense plasma. The erosion under an intense particle flux of hydrogen isotopes in a fusion reactor, the wall surface undergoes severe microstructural modification by causing material loss, but also changes its composition. This can simply be solved by using a Cr-based material in the mid-heat flux region rather than the direct heat flux region (e.g., coating on the top of the materials). However, the first 2 issues which is related to the intrinsic properties for the mechanical and hydrogen related resistances should have satisfied the minimum requirements. Otherwise, the special challenges such as the further development of existing material concepts are required to satisfy the diverse requirement for the PFM application.

1.4. Spark plasma sintering

The bulk W and Cr are generally produced through a classical powder metallurgy in which the desired properties with dense microstructure is difficult to obtain. The bulk samples with high sintered density is achievable via SPS process, a novel powder metallurgy technique utilizing a pulsed electric current along with mechanical pressure. With the electric current directly passing through a powder compact placed in graphite die and punches, a sintered W with a near-theoretical density can be achieved in only a few minutes. This can be enhanced by the current flow through the specimen might enhances the diffusion process (electromigration) [46–50]. The schematic diagram of the SPS device is shown in Figure 2. For the SPS, the graphite mold is very widely used due to the excellent performance characteristics. The combination of exceptional thermal and electrical conductivities and a low coefficient of thermal expansion at a wide range of temperatures is an essential element to ensure the dimensional stability of sintering molds. In addition, the graphite mold used to manufacture a sintering mold is selected based on the process temperature and pressure requirements. With the good machinability with a cheap cost, graphite mold can commercially be available in the SPS process. What is noteworthy here is that W and Cr are a strong carbide-forming element [51, 52]. The inevitable carbon (C) absorption of W and Cr during the SPS induces W and/or Cr carbide segregation at the grain boundary, thereby reducing the ductility and leading to a brittle intergranular fracture [24, 53, 54, 55]. Furthermore, the high content of C in the materials adversely affects deuterium exposure [56]. Therefore, it is very important to suppress the C diffusion into the materials during the SPS process.

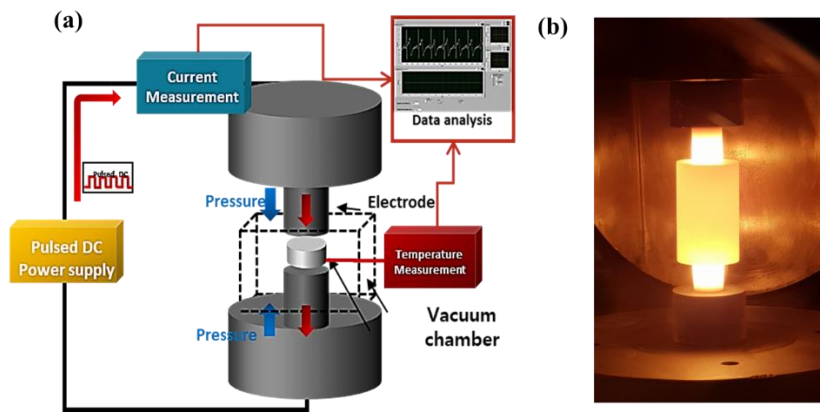


Figure 2 (a) Schematic diagram of SPS system [49]; (b) The image for consolidation of powder in graphite mold during SPS

1.5. Research objectives and structure of thesis

In this work, for the first time, we proposed and developed a new composite material based on the microstructural design concept, which achieves both strength and elongation by reinforcing Cr with W. In order to achieve both properties, we fabricated a two-phase material in which Cr and W exist, separately. Here, the materials developed in this thesis will be called to as “Cr-W dual-phase composites”. Since the microstructural features are complicated and it is challenge to fabricate these microstructures by casting technology, a powder metallurgical process using SPS was used as a fabrication method. The aims of this thesis are to develop a new Cr-W dual-phase composite based on the characterization of microstructures and properties. Before the development of Cr-W dual-phase composites, the issues of C diffusion in the SPS process will firstly be explored by introducing C diffusion barriers, and this concept will be applied to the following chapters. In addition, the pure W and Cr were fabricated together with developed materials for the comparison. This thesis is comprised of three main parts.

In chapter 2. The metallic foils as a C diffusion barrier were introduced in SPSed W to minimize the C diffusion. In the beginning, the several metallic foils were applied to the different sintering temperature to observe the effect of each metallic foil. Then the secondary phases formed in the different systems will be identified. Based on this information, thermodynamic and kinetic analysis are discussed based on kinetic simulation and literature data. Finally, the applicability to Cr is explored.

In chapter 3. Cr-W dual-phase composites are fabricated through a high-energy mill and SPS. For the fabrication, all process parameters such as optimal powder size, milling time, and sintering temperatures were controlled. The milled powders and sintered products are physically and chemically characterized through electron microscopy and X-ray diffraction. In addition, the basic properties such as hardness and density were measured. Compacts of the as-milled powders are SPSed with several heating rate and their length change is measured to estimate the sintering kinetics. The sinterability of W in Cr-W dual-phase composites is accelerated by the Cr diffusion.

In chapter 4. Cr-W dual-phase composites are characterized to observe their

potential applicability as PFMs. First, the mechanical properties by the 3-point bending test were estimated at RT (under DBTT) and 300 °C (near DBTT). Second, the deuterium retention behaviors were understood based on plasma exposures, nuclear reaction analysis, and thermal desorption spectroscopy. With that, we can obtain the deuterium amounts for near the surface and deep in the bulk, which can help us understand the deuterium diffusion behaviors of the fabricated materials.

1.6. References

- [1] U. Schumacher, Status and problems of fusion reactor development, *Sci. Nat.* 88(3) (2001) 102–112.
- [2] T.S. Reshid, Study of some structural fusion materials for (n, 2n) reactions, *J. Fusion Energy* 34(4) (2015) 746–750.
- [3] W.J. Nuttall, *Fusion as an energy source: Challenges and Opportunities*, Institute for Physics, London, UK (2008).
- [4] ITER, EDA. Documentation Series No. 24 ITER Technical Basis, IAEA, Vienna (2002)
- [5] G. Federici, W. Biel, M.R. Gilbert, R. Kemp, N. Taylor, R. Wenninger, European DEMO design strategy and consequences for materials, *Nucl. Fusion* 57(9) (2017) 092002.
- [6] D. Stork, P. Agostini, J.L. Boutard, D. Buckthorpe, E. Diegele, S.L. Dudarev, C. English, G. Federici, M.R. Gilbert, S. Gonzalez, A. Ibarra, Ch. Linsmeier, A. Li Puma, G. Marbach, P.F. Morris, L. W. Packer, B. Raj, M. Rieth, M.Q. Tran, D.J. Ward, S.J. Zinkle, Developing structural, high-heat flux and plasma facing materials for a near-term DEMO fusion power plant: the EU assessment, *J. Nucl. Mater.* 455(1–3) (2014) 277–291.
- [7] D. Maisonnier, D. Campbell, I. Cook, L. Di Pace, L. Giancarli, J. Hayward, A. Li Puma, M. Medrano, P. Norajitra, M. Roccella, P. Sardain, M.Q. Tran, D. Ward, Power plant conceptual studies in Europe, *Nucl. Fusion* 47(11) (2007) 1524.
- [8] M. Keilhacker, ASDEX Team, The ASDEX divertor tokamak, *Nucl. Fusion* 25(9) (1985) 1045.
- [9] K. Ikeda, ITER on the road to fusion energy, *Nucl. Fusion* 50(1) (2009) 014002.
- [10] R.A. Pitts, S. Carpentier, F. Escourbiac, T. Hirai, V. Komarov, A.S. Kukushkin, S. Lisgo, A. Loarte, M. Merola, R. Mitteau, A.R. Raffray, M. Shimada, P.C. Stangeby, Physics basis and design of the ITER plasma-facing components, *J. Nucl. Mater.* 415(1) (2011) S957–S964.
- [11] M.A. Pick, J. Team, The technological achievements and experience at JET, *Fusion Eng. Des.* 46(2–4) (1999) 291–298.
- [12] O. Gruber, ASDEX Upgrade enhancements in view of ITER application, *Fusion*

Eng. Des. 84(2-6) (2009) 170–177.

[13] J. Winter, F. Waelbroeck, P. Wienhold, H.G. Esser, L. Könen, M. Braun, B. Emmoth, H.E. Säterblom, Wall conditioning of TEXTOR, J. Nucl. Mater. 128 (1984) 841–850.

[14] S. Wu, EAST team, An overview of the EAST project, Fusion Eng. Des. 82(5–14) (2007) 463–471.

[15] Y. Shimomura, K. Shimizu, T. Hirayama, M. Azumi, H. Ninomiya, JT-60 program, J. Nucl. Mater. 128 (1984) 19–25.

[16] H. Bolt, V. Barabash, G. Federici, J. Linke, A. Loarte, J. Roth, K. Sato, Plasma facing and high heat flux materials—needs for ITER and beyond, J. Nucl. Mater. 307 (2002) 43–52.

[17] R.P. Wenninger, M. Bernert, T. Eich, E. Fable, G. Federici, A. Kallenbach, A. Loarte, C. Lowry, D. McDonald, R. Neu, T. Pütterich, P. Schneider, B. Sieglin, G. Strohmayer, F. Reimold, M. Wischmeier, DEMO divertor limitations during and in between ELMs, Nucl. Fusion, 54(11) (2014) 114003.

[18] J. Riesch, Y. Han, J. Almanstötter, J.W. Coenen, T. Höschen, B. Jasper, P. Zhao, Ch. Linsmeier, R. Neu, Development of tungsten fibre-reinforced tungsten composites towards their use in DEMO—potassium doped tungsten wire, Phys. Scr. 2016(T167) (2016) 014006.

[19] J. Roth, E. Tsitrone, A. Loarte, T. Loarer, G. Counsell, R. Neu, V. Philipps, S. Brezinsek, M. Lehnen, P. Coad, Ch. Grisolia, K. Schmid, K. Krieger, A. Kallenbach, B. Lipschultz, R. Doerner, R. Causey, V. Alimov, W. Shu, O. Ogorodnikova, A. Kirschner, G. Federici, A. Kukushkin, EFDA PWI Task Force, ITER PWI Team, Fusion for Energy, ITPA SOL/DIV, Recent analysis of key plasma wall interactions issues for ITER, J. Nucl. Mater. 390 (2009) 1–9.

[20] Y. Ueda, K. Schmid, M. Balden, J.W. Coenen, T. Loewenhoff, A. Ito, A. Hasegawa, C. Hardie, M. Porton, M. Gilbert, Baseline high heat flux and plasma facing materials for fusion, Nucl. Fusion 57(9) (2017) 092006.

[21] C. Linsmeier, B. Unterberg, J.W. Coenen, R.P. Doerner, H. Greuner, A. Kreter, J. Linke, H. Maier, Material testing facilities and programs for plasma-facing component testing, Nucl. Fusion 57(9) (2017) 092012.

[22] O. El-Atwani, N. Li, M. Li, A. Devaraj, J.K.S. Baldwin, M.M. Schneider, D. Sobieraj, J.S. Wróbel, D. Nguyen-Manh, S.A. Maloy, E. Martinez, Outstanding

radiation resistance of tungsten-based high-entropy alloys, *Sci. Adv.* 5(3) (2019) eaav2002.

[23] M. Binder, G. Calabro, R. De Luca, P. Fanelli, R. Neu, G. Schlick, F. Vivio, Tailored tungsten lattice structures for plasma-facing components in magnetic confinement fusion devices, (2020) 146–147.

[24] D. Terentyev, T. Khvan, J.-H. You, N. Van Steenberge, Development of chromium and chromium-tungsten alloy for the plasma facing components: Application of vacuum arc melting techniques, *J. Nucl. Mater.* 536 (2020) 152204.

[25] N. Alexander, B.P. Bromley, M. Delage, T. Howard, R. Fedosejevs, A.A. Offenberger, Y. Tsui, H. Gaber, A. Smolyakov, C. Xiao, A. Wallace, M. Dalzell, Fusion 2030: A roadmap for Canada to develop fusion energy, In 37th Annual Conference of the Canadian Nuclear Society and 41st Annual CNS/CNA Student Conference. (2017).

[26] I. Smid, M. Akiba, G. Vieider, L. Plöchl, Development of tungsten armor and bonding to copper for plasma-interactive components, *J. Nucl. Mater.* 258 (1998) 160–172.

[27] Y. Oh, N. Kwak, K. Lee, W.-S. Ko, H.N. Han, Ductility enhancement of tungsten after plastic deformation, *J. Alloys Compd.* 787 (2019) 801–814.

[28] G. Pintsuk, I. Bobin-Vastra, S. Constans, P. Gavila, M. Rödiger, B. Riccardi, Qualification and post-mortem characterization of tungsten mock-ups exposed to cyclic high heat flux loading, *Fusion Eng. Des.* 88(9–10) (2013) 1858–1861.

[29] M. Li, J.-H. You, Interpretation of the deep cracking phenomenon of tungsten monoblock targets observed in high-heat-flux fatigue tests at 20 MW/m², *Fusion Eng. Des.* 101 (2015) 1–8.

[30] J. Linke, T. Loewenhoff, V. Massaut, G. Pintsuk, G. Ritz, M. Rödiger, A. Schmidt, C. Thomser, I. Uytendhouwen, V. Vasechko, Performance of different tungsten grades under transient thermal loads, *Nucl. Fusion* 51(7) (2011) 073017.

[31] M.R. Gilbert, S.L. Dudarev, D. Nguyen-Manh, S. Zheng, L.W. Packer, J.-C. Sublet, Neutron-induced dpa, transmutations, gas production, and helium embrittlement of fusion materials, *J. Nucl. Mater.* 442(1–3) (2013) S755–S760.

[32] J.-H. You, G. Mazzone, Ch. Bachmann, D. Coccoresse, V. Cocilovo, D. De Meis, P.A. Di Maio, D. Dongiovanni, P. Frosi, G. Di Gironimo, S. Garitta, G. Mariano, D. Marzullo, M.T. Porfiri, G. Ramogida, E. Vallone, R. Villari, M. Zucchetti, *Progress*

in the initial design activities for the European DEMO divertor: Subproject “Cassette”, *Fusion Eng. Des.* 124 (2017) 364–370.

[33] H. Bolt, V. Barabash, G. Federici, J. Linke, A. Loarte, J. Roth, K. Sato, Plasma facing and high heat flux materials—needs for ITER and beyond, *J. Nucl. Mater.* 307 (2002) 43–52.

[34] R.A. Pitts, S. Carpentier, F. Escourbiac, T. Hirai, V. Komarov, S. Lisgo, A.S. Kukushkin, A. Loarte, M. Merola, A. Sashala Naik, R. Mitteau, M. Sugihara, B. Bazylev, P.C. Stangeby, A full tungsten divertor for ITER: Physics issues and design status, *J. Nucl. Mater.* 438 (2013) S48–S56.

[35] J. Linke, High heat flux performance of plasma facing materials and components under service conditions in future fusion reactors, *FST* 49(2T) (2006) 455–464.

[36] J.W. Coenen, S. Antusch, M. Aumann, W. Biel, J. Du, J. Engels, S. Heuer, A. Houben, T. Hoeschen, B. Jasper, F. Koch, J. Linke, A. Litnovsky, Y. Mao, R. Neu, G. Pintsuk, J. Riesch, M. Rasinski, J. Reiser, M. Rieth, A. Terra, B. Unterberg, Th. Weber, T. Wegener, J.-H. You, Ch. Linsmeier, Materials for DEMO and reactor applications—boundary conditions and new concepts, *Phys. Scr.* 2016(T167) (2015) 014002.

[37] W.D. Klopp, Recent developments in chromium and chromium alloys, *JOM* 21(11) (1969) 23–32.

[38] W.D. Klopp, A review of chromium, molybdenum, and tungsten alloys, *J Less Common Met* 42(3) (1975) 261–278.

[39] P. Rocco, M. Zucchetti, The impact of low-activation criteria on the development of novel materials for fusion, *J. Nucl. Mater.* 212 (1994) 649–654.

[40] M. Zucchetti, M. Merola, Low-activation properties of novel Cr-based materials for fusion reactors, *J. Nucl. Mater.* 233 (1996) 1486–1490.

[41] T. Massalski, P.R. Subramanian, Hf (Hafnium) Binary Alloy Phase Diagrams, ASM international, Cleveland (1990).

[42] R. Eck, H.P. Martinz, T. Sakaki, M. Kato, Powder metallurgical chromium, *Mater. Sci. Eng. A* 120 (1989) 307–312.

[43] H.P. Martinz, R. Eck, J. Eiter, T. Sakaki, M. Kato, Corrosion Behaviour of Powder Metallurgically Produced Chromium, *Werkst. Korros.* 40(12) (1989) 715–719.

- [44] D. Terentyev, T. Khvan, J.-H. You, N. Van Steenberge, Development of chromium and chromium-tungsten alloy for the plasma facing components: Application of vacuum arc melting techniques, *J. Nucl. Mater.* 536 (2020) 152204.
- [45] G.R. Tynan, R.P. Doerner, J. Barton, R. Chen, S. Cui, M. Simmonds, Y. Wang, J.S. Weaver, N. Mara, S. Pathak, Deuterium retention and thermal conductivity in ion-beam displacement-damaged tungsten, *Nucl. Mater. Energy*. 12 (2017) 164–168.
- [46] R. Orru, R. Licheri, A.M. Locci, A. Cincotti, G. Cao, Consolidation/synthesis of materials by electric current activated/assisted sintering, *Mater. Sci. Eng. R Rep.* 63(4–6) (2009) 127–287.
- [47] N. Kwak, G. Min, Y. Oh, D.-W. Suh, H.C. Kim, S.-G. Kang, H.N. Han, Tantalum and molybdenum barriers to prevent carbon diffusion in spark plasma sintered tungsten, *Scr. Mater.* 196 (2021) 113759.
- [48] J. Choi, H.-M. Sung, K.-B. Roh, S.-H. Hong, G.-H. Kim, H.N. Han, Fabrication of sintered tungsten by spark plasma sintering and investigation of thermal stability, *Int. J. Refract. Hard Mater.* 69 (2017) 164–169.
- [49] Y.J. Lee, H.-M. Sung, Y. Jin, K. Lee, C.R. Park, G.-H. Kim, H.N. Han, Improvement of mechanical property of air plasma sprayed tungsten film using pulsed electric current treatment, *Int. J. Refract. Hard Mater.* 60 (2016) 99–103.
- [50] M.-J. Kim, S. Yoon, S. Park, H.-J. Jeong, J.-W. Park, K. Kim, J. Jo, T. Heo, S.-T. Hong, S.H. Cho, Y.-K. Kwon, I.-S. Choi, M. Kim, H.N. Han, Elucidating the origin of electroplasticity in metallic materials, *Appl. Mater. Today* 21 (2020) 100874.
- [51] L. Zhong, X. Zhang, S. Chen, Y. Xu, H. Wu, J. Wang, Fe–W–C thermodynamics and in situ preparation of tungsten carbide-reinforced iron-based surface composites by solid-phase diffusion, *Int. J. Refract. Hard Mater.* 57 (2016) 42–49.
- [52] S. Cho, K. Kikuchi, T. Miyazaki, A. Kawasaki, Y. Arami, J.F. Silvain, Epitaxial growth of chromium carbide nanostructures on multiwalled carbon nanotubes (MWCNTs) in MWCNT–copper composites, *Acta Mater.* 61(2) (2013) 708–716.
- [53] J.W. Coenen, Y. Mao, S. Sistla, J. Riesch, T. Hoeschen, C. Broeckmann, R. Neu, C. Linsmeier, Improved pseudo-ductile behavior of powder metallurgical tungsten short fiber-reinforced tungsten (Wf/W), *Nucl. Mater. Energy*. 15 (2018) 214–219.
- [54] J.R. Stephens, Effect of oxygen on mechanical properties of tungsten, National Aeronautics and Space Administration, Washington D. C., US (1963).

[55] J.R. Stephens, Effects of interstitial impurities on the low-temperature tensile properties of tungsten (Vol. 2287), National Aeronautics and Space Administration, Washington D. C., US (1964).

[56] Y. Ueda, T. Shimada, M. Nishikawa, Impacts of carbon impurities in hydrogen plasmas on tungsten blistering, Nucl. Fusion 44(1) (2003) 62.

Chapter 2. Metallic foils as a C diffusion barrier

2.1. Introduction

Already mentioned above chapter 1, tungsten (W) and chromium (Cr) have become a significant material in nuclear fusion energy industries, with extreme environmental applications [1–5]. Because of their high melting temperature of over 3400 and 1900 °C, bulk W and Cr are generally obtained by a classical powder metallurgy, which cannot provide the desired properties and dense microstructure [2]. Bulk W and Cr with high density can be achieved only in a few minutes using spark plasma sintering (SPS). However, for the SPS, a powder compact should be placed in a graphite mold (die and punches) [6–11]. What is noteworthy here is that W and Cr are strong carbide-forming elements [13]. The carbon (C) absorption of W and Cr during the SPS cannot be avoided. Coenen et al. [13] and Mao et al. [14] showed that the W foil effectively reduced the C uptake in sintered W during the SPS. However, it was a simple physical barrier introduced for C diffusion. In this study, we introduce tantalum (Ta) and molybdenum (Mo) protective foils in addition to W protective foils, which can suppress the C diffusion physically and thermodynamically. W, Ta, and Mo are well-known carbide-forming elements that can inhibit C diffusion at the foil/W interface. We thoroughly investigated the C distribution at the foil/W interface by keeping the foil and W subsurface adhered to the sample, unlike previous studies that did not focus on the W subsurface. Cross-sectional elemental mapping and thermodynamic-kinetic analysis identify the underlying requirements for suppressing the C diffusion. With this background, we finally proceed to apply this concept to the Cr system whether it can be generalized or not. We believe this study provides a critical insight to select the appropriate protective foil for spark plasma sintered (SPSed) W and Cr with a highly controlled impurity content, and also set a fundamental guideline to design the carburization resistant structural materials for extreme environmental applications such as petrochemistry, organic chemistry, and nuclear fusion fields.

2.2. Experimental procedures

2.2.1 Materials and methods

For the protective foil materials, we chose Ta, and Mo by considering their thermodynamic stability, implying Ta and Mo are stable carbide-forming elements (Figure 3). In addition, the W protective foil, which was effective in the spark plasma sintered W [13], was also studied for the comparison. To investigate the effect of protective foils as a C diffusion barrier, we prepared 4 samples: a conventional W-C system and foil-protected W-W-C, W-Mo-C, and W-Ta-C systems. In every sample, the W powder (Taegu Tec) with an average particle size of $\leq 0.5 \mu\text{m}$ and a high purity of $>99.9\%$ was used. To minimize C diffusion into W during the SPS, two processes were utilized. For the conventional W-C system, a W powder compact covered by a C foil is placed in a graphite mold (die and punches) (Figure 4 (a)). For the foil-protected system, we placed commercial-grade Ta, Mo foils (Alfa Aesar), and W foil (Goodfellow) with $25 \mu\text{m}$ thickness between the C foil and W powder compact (W-W-C, W-Ta-C, and W-Mo-C systems, respectively). (Figure 4 (b)). Before inserting the foils, they were gently polished to the same level to minimize the surface effect.

The SPS was conducted in the temperature range of $1700\text{--}1900\text{ }^{\circ}\text{C}$ with a heating rate of $100\text{ }^{\circ}\text{C}/\text{min}$, under an applied stress of 65 MPa for 10 min . We set these process parameters based on our previous research work in which a highly densified SPSed W with relative density of $>99\%$ was obtained [6]. The SPSed W had a cylindrical shape, as shown in Figure 4 (c).

To observe the applicability to Cr powder with the use of this concept, commercially available Cr powder (Goodfellow) with an average particle size of $45\text{--}150 \mu\text{m}$ and a purity of 99% was used. The Ta protective foil, which will be confirmed as the most effective C diffusion barrier, was applied to the Cr powder. The SPS was conducted in the temperature range of $1300\text{ }^{\circ}\text{C}$ with a heating rate of $100\text{ }^{\circ}\text{C}/\text{min}$, under an applied stress of 65 MPa for 10 min .

2.2.2 Characterization

The microstructure was observed in view of the axial direction (AD) of the cylindrical surface, keeping the foil and/or the subsurface adhered to the sample to trace C diffusion, as shown in Figure 4 (c). We analyzed the microstructural changes and C diffusion along the radial direction (RD) of the cylindrical SPSed W and Cr. To prepare samples on which this analysis could be conducted, we polished the top surfaces of the all samples with colloidal silica and observed the outer surface including the foils and W subsurface in the AD using a field-emission scanning electron microscope (FE-SEM, MERLIN Compact, ZEISS, Germany) and an electron probe microanalyzer (FE-EPMA, JXA-8530F, JEOL Ltd, Japan).

For W system, thermodynamic-kinetic simulations were performed using the Thermo-Calc linked with a diffusion module (DICTRA) that employed the TCFE9 thermodynamic and MOBFE4 mobility databases. We constructed a diffusion model with a 75 μm thick W matrix in contact with a 25 μm thick protective foil as a C diffusion barrier and assumed an infinite C source on the opposite side of the foil. The carbide formation by C diffusion over time was set as the output, and substitutional diffusion was neglected. The dwell time and temperature were 600 s and 1700 °C, respectively.

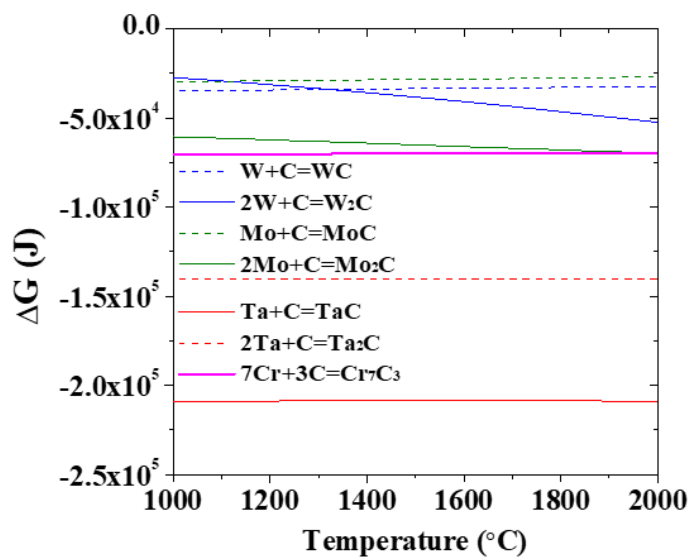


Figure 3 Variation of Gibbs free energy (ΔG) as a function of temperature for possible reactions during the sintering of the system.

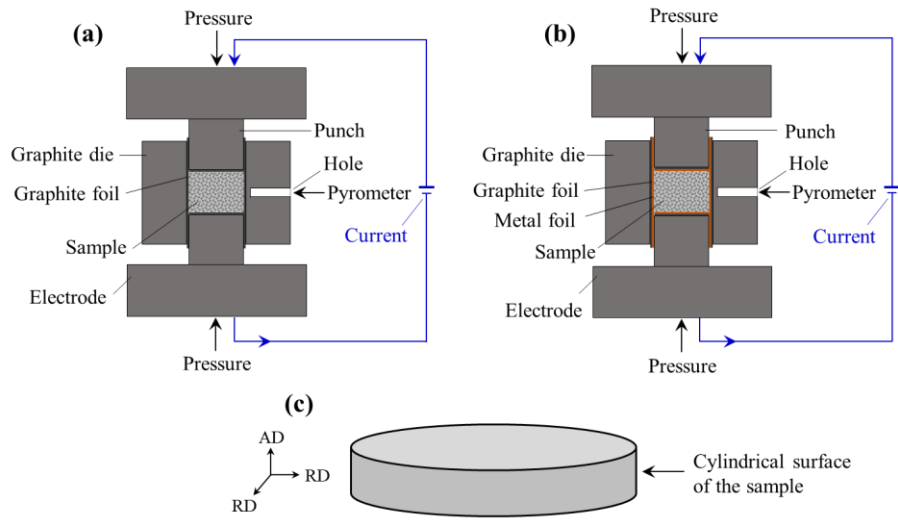


Figure 4 Schematic illustration of graphite mold assembly used in SPS for (a) without a C diffusion barrier and (b) with W, Ta, or Mo as a C diffusion barrier. The sintered sample is cylindrical and (c) the microstructure is observed with the view in the AD of the cylindrical surface.

2.3. Results and discussion

2.3.1 The effect of protective foils in W powders

SPSed W protected by a Ta foil showed a distinctively different microstructure compared to that of the W-C, W-W-C, and W-Mo-C systems. This could be seen clearly from a subsurface in the SPSed W. Figure 5 shows cross-sectional SEM images of W-C, W-C, W-Mo-C, and W-Ta-C systems sintered at 1700, 1800, and 1900 °C. The C foil is located at the right edge of each SEM image (surfaces in contact with the C foil and protective foils are marked by green and yellow dashed lines, respectively). The W-C system sintered at 1700 °C has a 50 µm thick subsurface in contact with the C foil (Figure 5 (a), boundary between the W matrix and subsurface is indicated by the white dashed line). This subsurface became thicker as the sintering temperature increased. The thicknesses of the subsurface were 70 and 150 µm for sintering temperatures of 1800 and 1900 °C, respectively (Figure 5 (b) and (c)). These results are similar to the previously identified subsurfaces in different alloy systems possessing carbide-forming elements [15–19]. The thickening of the subsurface in the W-C system can be attributed to the increasing C uptake of W with the sintering temperature. In W-W-C system, the subsurfaces are similar to the W-C system, but it observed to be thinner at all temperatures (Figure 5 (d-f)). Even in the W-Mo-C system, we observed a similar subsurface in the SPSed W. In this case, the subsurface is in contact with the Mo foil, and the thicknesses are 75, 100, and 140 µm for sintering temperatures of 1700, 1800, and 1900 °C, respectively (Figure 5 (g-i)). However, for the W-Ta-C system, there is no subsurface in SPSed W, but various second phases are present in the Ta foil. The SEM image of the W-Ta-C system sintered at 1700 °C in Figure 5 (j) shows second phases distributed near Ta/C and Ta/W interfaces (indicated by yellow, blue, and white arrows in red squares (A) and (B)). These second phases still exist with sintering temperatures of 1800 and 1900 °C (Figures 5 (k) and (l)). Distinctive differences in the microstructure of each SPSed W are attributed to the C diffusion during the SPS, which can be confirmed by the cross-sectional elemental mapping.

The Ta foil successfully suppressed the C diffusion to W during the SPS. Figure

6 shows the cross-sectional SEM images and corresponding EPMA elemental mapping images of W-C, W-W-C, W-Mo-C, and W-Ta-C systems sintered at 1700 °C. In each SEM image (Figure 6 (a-d)), the region of interest for EPMA analysis is outlined by red squares. As expected, the subsurface originated from direct carbide formation in W (WC or W₂C). The elemental mapping image in Figure 6 (e) shows that the subsurface of SPSed W for W-C system has a high C content. The local chemical composition in Table 1 suggests that the phases of W (Point 1) and W subsurface (Point 2) (denoted by orange circles in Figure 6 (a)) are W and W₂C, respectively, which means that W is converted to W carbide. This is consistent with previous studies where severe carbide formation in W occurred during the SPS [17]. In Figure 6 (f), the subsurface of SPSed W for W-W-C system has high C content even beyond W protective foil. The local chemical composition indicates that the phase of Point 3 is W, and that of W subsurface (Point 4) and W foil (Point 5) are W₂C, which means the conversion to W carbide was proceeded from W foil to SPSed W, sequentially. The use of W foil can help suppress the C diffusion compared to W-C system, but its role in SPSed W might only act as a physical barrier because sintered material is the same. Therefore, the sluggish diffusion C into W was contributed only by the physical dedication of W foil, not by another important function. Interestingly, this carbide formation also occurred in the W-Mo-C system. Figure 6 (g) shows that the Mo protective foil and the subsurface have a high C content. The local chemical composition of W (Point 6), W subsurface (Points 7 and 8), and Mo protective foil (Point 9) are identical to those of W, W₂C, WC, and Mo₂C, respectively (Table 1). Thermodynamically, Mo can be converted into η-MoC and/or Mo₂C (Figure 7 (a)). Considering the local chemical composition and C concentration gradient in the Mo foil, the outermost surface of the Mo foil in contact with the graphite mold appears to be converted into MoC. This suggests that the high flux of C carburizes not only the Mo protective foil but also the W during the SPS. Note that there are monocarbides (WC) at the W subsurface in direct contact with the Mo₂C phase. The WC formation before W₂C is due to the well-known carburization step of W [20, 21]. Unlike the Mo foil, which is not effective as a C diffusion barrier, the Ta foil suppresses the C diffusion and the W carbide formation during the SPS. Figure 6 (h) shows the highly concentrated C content in the Ta protective foil. The chemical composition of W (Point 10) shows the lowest C

content compared to that of the W-C, W-W-C, and W-Mo-C systems (Table 1). However, the Ta surface in contact with C foil is enriched with C, and there are C concentrated islands within the Ta foil (denoted by green dashed line and pink dashed ellipses in Figure 6 (h)). The chemical composition of the C-concentrated island (Point 11) and C-enriched surface (Point 14) within the foil are identical to Ta₂C and TaC (Table 1), which can be formed thermodynamically by the C uptake (Figure 7 (b)). A similar microstructure can be obtained by the thermal carburization of Ta [22]. During the carburization, a bilayer of TaC on the surface and Ta₂C below is formed by the direct C flux. During further annealing and cooling, owing to the C solubility of Ta, the dissolution of Ta₂C layer and re-precipitation of Ta₂C within the Ta matrix occur. Accordingly, the discontinuous Ta₂C islands in this study can be attributed to the thermal history of SPS. Furthermore, as the Ta is also a strong oxide-forming element, it protects the SPSed W from O diffusion as well. In the W-Ta-C system, O content of SPSed W is remarkably lower than that in the W-C, W-W-C, and W-Mo-C systems. Also, there are O-enriched regions in Ta foil where the chemical composition is identical to Ta₂O₅ (Point 13). It should be noted that the C and O contents of Ta foil are still low except the regions with secondary phases (Point 12 in Figure 6 (c)), suggesting that the Ta foil is capable of taking C and/or O even after the SPS. Since the Ta protective foil did not allow C diffusion into W, no WC and/or W₂C was found in the W-Ta-C system after the SPS. Both Mo and Ta are carbide-forming elements, but the carbide growth in W-Mo-C and W-Ta-C systems was vastly different from one another.

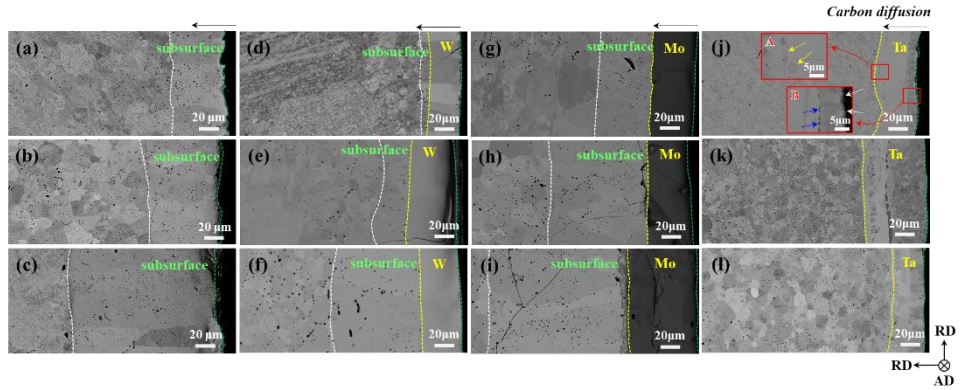


Figure 5 Cross-sectional SEM images of SPSed W samples with the view of the AD of cylindrical surface. The diffusion of C begins with the cylindrical surface and extends inside the samples, its direction is indicated by the black arrows, and the green dashed lines denote the region of direct contact with C: (a–c) W-C, (d–f) W-W-C, (g–i) W-Mo-C, and (j–l) W-Ta-C systems. Sintering temperatures of (a), (d), (g), (j) = 1700 °C ; (b), (e), (h), (k) = 1800 °C; (c), (f), (i), (l) = 1900 °C, and the dwell time = 10 min for all. The subsurfaces of the SPSed W affected by C flux are lined by white and green dashed lines for (a–c) and white and yellow dashed lines for (d–i), respectively. The original metallic foil regions are covered by yellow and green dashed lines for (d–l). The red squares of A and B in (g) show microstructural development in Ta foil during sintering (indicated by yellow, blue, and white arrows).

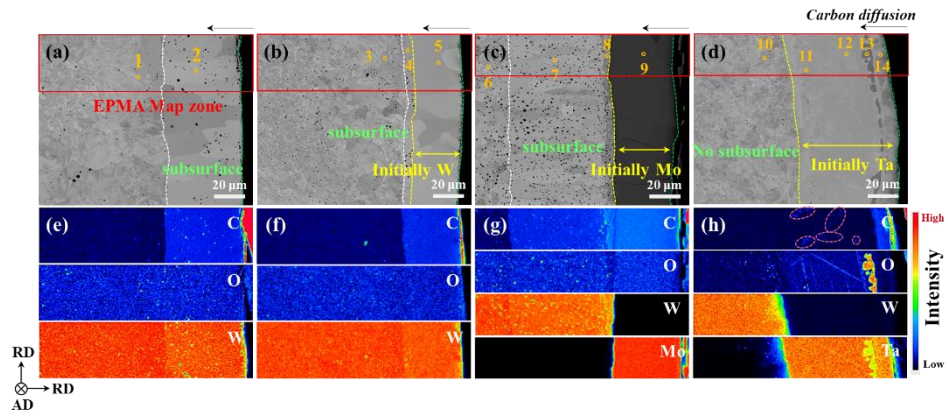


Figure 6 SEM images (up) and EPMA elemental mappings (down) of the W samples sintered at 1700 °C for 10 min. with the view in the AD of cylindrical surface: (a), (e) W-C, (b), (f) W-W-C, (c), (g) W-Mo-C, and (d), (h) W-Ta-C systems. Black arrows indicate the direction of C diffusion. In (a–d), the red squares denote EPMA map zones and various points (1 to 14) marked by orange circles indicate local regions distinguished by different phases. Local chemical compositions at various points are shown in Table 1.

Table 1 Local chemical compositions (at.%) of W system at various points (1 to 14) indicated in Figure 6 (a–d) to identify the different phases after sintering at 1700 °C for 10 min.

System	Point	W	Ta	Mo	C	O	Phase
W-C	1	96.2	0	0	2.65	1.15	W
	2	72.8	0	0	26.4	0.8	W ₂ C
W-W-C	3	99.6	0	0	0.3	0.1	W
	4	25.9	0	0	73.9	0.2	W ₂ C
	5	24.5	0	0	75.1	0.4	W ₂ C
W-Mo-C	6	96.4	0	0.1	3.5	0	W
	7	71.2	0	0.1	28.1	0.6	W ₂ C
	8	48.9	0	5.6	45.5	0	WC
	9	0.1	0	65.2	34.7	0	Mo ₂ C
W-Ta-C	10	98.7	0.5	0	0	0.8	W
	11	2.4	69.6	0	26.9	1.1	Ta ₂ C
	12	3.3	92.2	0	0	4.5	Ta
	13	1.1	31.9	0	1.1	65.9	Ta ₂ O ₅
	14	1.7	46.2	0	50.6	1.5	TaC

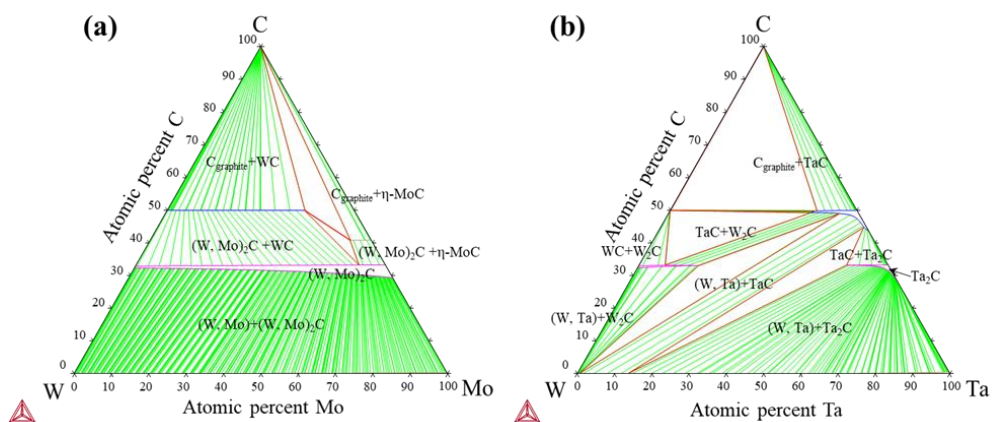


Figure 7 Calculated ternary phase diagram using Thermo-Calc® (TCFE9 database): isothermal section of (a) W-Mo-C and (b) W-Ta-C system at 1700 °C.

2.3.2 Understanding of C diffusion in W through thermodynamic and kinetic data

The carbide growth is highly dependent on the C diffusivity in the metal protective foil. We can approximate the carbide growth rate from the C flux balance at the carbide-metal interface. In terms of C flux in carbide (J_{carbide}) and metal (J_{metal}), one-dimensional carbide growth can be expressed as follows:

$$\Delta C \cdot v = J_{\text{carbide}} - J_{\text{metal}} = -D_{\text{carbide}} \frac{\partial C_{\text{carbide}}}{\partial x} + D_{\text{metal}} \frac{\partial C_{\text{metal}}}{\partial x} \quad (1)$$

where ΔC is the concentration difference between the metal and carbide at the interface, v is the growth rate of carbide, D_{metal} and D_{carbide} are the C diffusivities in the metal and carbide, respectively. C_{metal} and C_{carbide} are the concentrations of C in the metal and carbide at the interface, respectively, and x is the diffusion distance of C. The second term is negligible as the C solubilities of Mo and Ta are low (Figure S5). Then, the total growth reaction can be approximated as follows:

$$\Delta C \cdot v \approx -D_{\text{carbide}} \frac{\partial C_{\text{carbide}}}{\partial x} \quad (2)$$

suggesting that the carbide growth rate is proportional to the C diffusivity in the metal carbides. Figure 8 shows the C diffusivity in the metal and carbide as a function of temperature [23–38]. The C diffusivity is approximately 5 times lower in Ta than that in Mo (semi-transparent green and red areas in Figure 8 (a)). The values differ by 1000 times in carbide forms (semi-transparent green and red areas in Figure 8 (b)), implying a slow carbide formation in Ta protective foil according to Equation (2). This is consistent with the shallow TaC layer near the Ta/C interface (Figure 8 (c)). Ta₂C islands located deeper in Ta foil possibly originate from fast C diffusion at the grain boundary. Therefore, the delayed carbide growth in Ta foil leads to suppressed carbon diffusion to the W matrix during the SPS. In addition, the solubility of C refers to the ability for C to dissolve in the elements. Figure 9 shows how the temperature influences solubility of C in the system. The solubility of C in the elements increases with an increase in temperature. However, the amount of

increment here is different from each elemental system. Ta is showing a sudden increase with temperature, allowing a C concentration about 0.6 at.% at sintering temperature. While, C is soluble in Mo only half amount of Ta (about 0.3 at.%). These differences with diffusivity and thermodynamic stability of C (Figures 8 and 3) would make large difference of the evolution of microstructure, as shown in Figures 5 and 6. In addition, it may also be explained that the reason for the present of discontinuous Ta_2C as mentioned in the chapter 2.3.1.

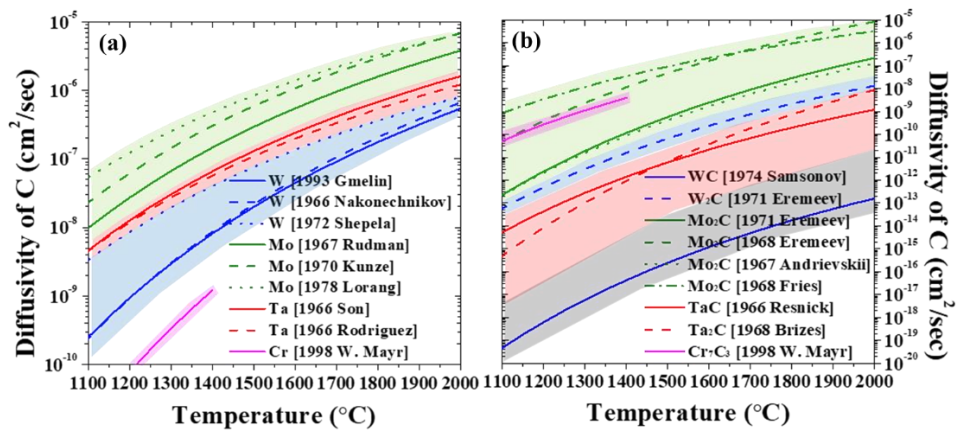


Figure 8 Diffusivity of C in metal (a) and carbide (b) in the system as a function of temperature. All data are from previous reports. The semi-transparent green, red, and blue areas represent C diffusivity in Mo and its carbides, Ta and its carbides, and W and its carbides, respectively. The corresponding area highlighted by semi-transparent grey indicate C diffusivity in WC.

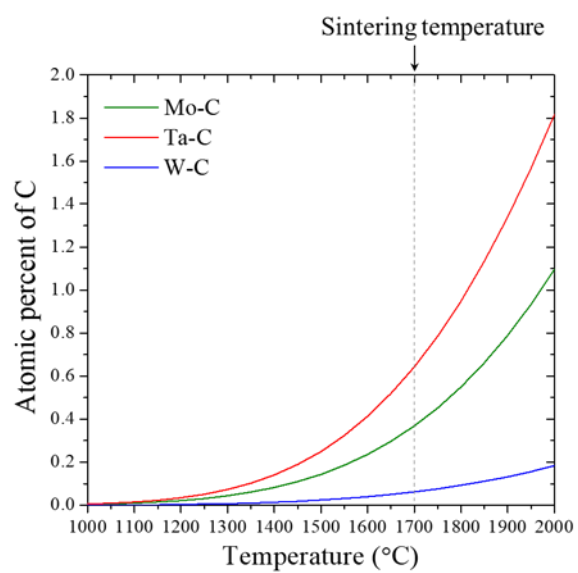


Figure 9 The C solubility curves of elements (Mo, Ta, and W) in the system as a function of temperature with the use of Thermo-Calc software (TCFE9 database).

2.3.3 The prediction of C diffusion by DICTRA simulation

Finally, we computationally demonstrate the C diffusion in W-Mo-C and W-Ta-C systems using thermodynamic-kinetic simulations (DICTRA). Although it is difficult to completely model the SPS, the simulation provides a simple approximation of the C diffusion at elevated temperatures. As expected, the C diffusion and resulting carbide growth are slow in the Ta foil. Figure 10 shows the changes in C diffusion and resultant microstructure depending on the protective foils at 1700 °C. In the W-Mo-C system, C diffuses rapidly to induce carbide formation in the W as well as in the Mo foil. The concentration profile at the Mo foil and W after 1 s (Figure 10 (a)) shows that C diffuses to a depth of 10 μm into the Mo foil. The stoichiometric ratio at the surface is identical to that of the Mo_2C . After 50 s, the W in contact with the Mo foil begins to convert into carbide (W_2C) by the incoming C flux from the Mo_2C (Figure 10 (b)). The W carbide grows with increasing time at 100 s (Figure 10 (c)), and it covers the entire system after 600 s (Figure 10 (d)). However, for the W-Ta-C system, the C diffusion in Ta foil is slow and in W matrix is suppressed. The C diffusion depth in Ta foil after 1 s is approximately 8 μm , similar to that in the Mo foil (Figure 10 (e)). The stoichiometric ratio at the surface is the same as that of the TaC. With increasing time of up to 50 s, the growth rate of TaC was slow compared to that of the Mo_2C , as predicted in Figure 10 (f). After 100 s, most of the Ta foil was converted into Ta carbide (Figure 10 (g)). Interestingly, even after 600 s, the W matrix was intact and free from carbide (Figure 10 (h)), suggesting that further C diffusion from the Ta foil to the W matrix was strongly suppressed. This could be attributed to the high thermodynamic stability of Ta carbide (Figure 3), which suggests that the C diffusion to W matrix at the W/foil interface will be suppressed until the entire Ta foil is converted into Ta carbide. Conversely, in the W-Mo-C system, the C diffusion from the Mo foil to W matrix at the interface is relatively easy because of the similar thermodynamic stability of carbides (Figure 3). Therefore, the slow C diffusion and high thermodynamic stability of the Ta carbide provide a potential advantage, that is, the Ta foil can protect the W matrix during the SPS at higher temperatures and longer times.

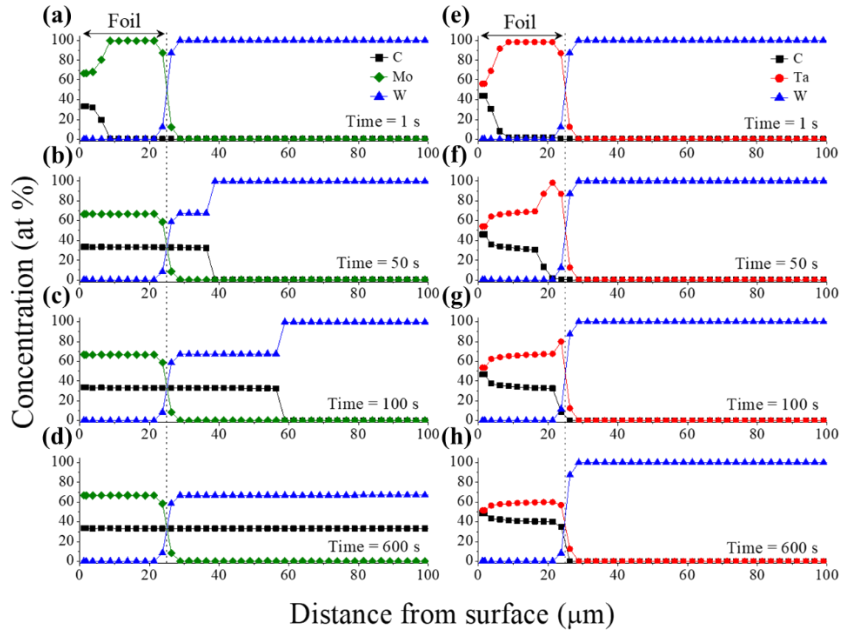


Figure 10 DICTRA prediction of concentration profiles of depth by C diffusion: (a–d) W-Mo-C, and (e–h) W-Ta-C systems. The profiles are representative snapshots of specific times (1, 50, 100, and 600 s)

2.3.4 The application to the Cr powder

Based on the results above, we understood required thermodynamic and kinetic properties for the application of protective foil. The relation of Cr with C is same as that of W, as shown in Figures 3 and 8, which means it is worth to use the Ta protective foil as a C diffusion barrier. Figure 11 shows the cross-sectional SEM images and corresponding EPMA elemental mapping images of Cr-C and Cr-Ta-C systems sintered at 1300 °C. In each SEM image (Figure 11 (a, b)), the region of interest for EPMA analysis is outlined by red squares. The elemental mapping image in Figure 11 (c) shows that the subsurface of SPSed Cr for Cr-C system has a high C content. The local chemical composition in Table 2 suggests that the phases of Cr (Point 1) and Cr subsurface (Point 2) (denoted by orange circles in Figure 11 (a)) are Cr and Cr₇C₃, respectively, which means that Cr is converted to Cr carbide by the direct C diffusion. For Ta foil-protected system, as expected, the Ta suppresses the C diffusion and the Cr carbide formation during the SPS. The elemental mapping image in Figure 11 (d) shows the highly concentrated C content in the Ta protective foil as similar as W-Ta-C system. The chemical composition of Cr (Point 3) shows the lowest C content compared to that of the Cr-C system (Table 2). However, the Ta surface in contact with C foil is enriched with C, and there are C concentrated islands within the Ta foil. The chemical composition of the C-concentrated island (Point 4) and C-enriched surface (Point 6) within the foil are identical to (Cr, Ta) and TaC (Table 2). The formation of C concentrated islands in Cr/foil interface suggests that further C diffusion from the Ta foil to the Cr matrix was strongly suppressed. This could be attributed to the high thermodynamic stability of Ta carbide (Figure 3), as similarly observed in W-Ta-C system. Considering the Ta foil has relatively high C content (Point 5), the suppression of C diffusion can be valid until the entire Ta foil is converted into Ta carbide, suggesting that the Ta foil is capable of taking C even after the SPS. Accordingly, the Ta protective foils can effectively suppress the C diffusion for SPSed Cr as well as W.

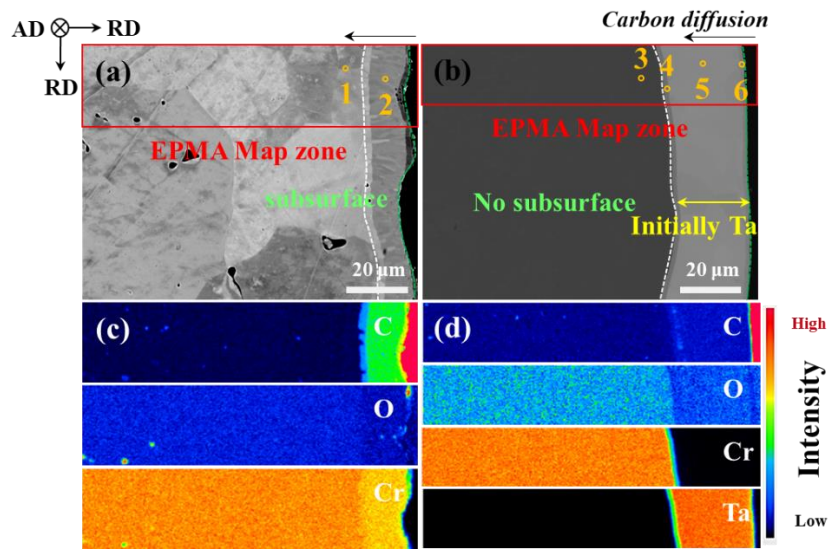


Figure 11 SEM images (a, b) and EPMA elemental mappings (c, d) of the Cr samples sintered at 1300 °C for 10 min. with the view in the AD of cylindrical surface: (a), (c) Cr-C, (b), (d) Cr-Ta-C systems. Black arrows indicate the direction of C diffusion. In (a, b), the red squares denote EPMA map zones and various points (1 to 6) marked by orange circles indicate local regions distinguished by different phases. Local chemical compositions at various points are shown in Table 2.

Table 2 Local chemical compositions (at.%) of Cr systems at various points (1 to 6) indicated in Figure 11 (a–b) to identify the different phases after sintering at 1300 °C for 10 min.

System	Point	Cr	Ta	C	O	Phase
Cr-C	1	96.8	0	3.2	0	Cr
	2	69.5	0	30.5	0	Cr ₇ C ₃
Cr-Ta-C	3	97.5	0	2.5	0	Cr
	4	61.5	29.2	9.3	0	(Cr,Ta)
	5	0.3	84.6	10.9	4.2	Ta
	6	0.3	43.2	56.5	0	TaC

2.4. Conclusions

We conducted a comparative study of three different protective foils to suppress carbide formation in SPSed W. By introducing W, Mo, and Ta foils as a protective layer, we investigated the microstructural change of W after the SPS process. The W-W-C system can suppress the C diffusion compared to W-C system, but the complete suppression is not possible because it is attributed by only physical suppression. Notably, the carbide formation in W-Ta-C system is strongly suppressed, in contrast to that in W-Mo-C system. It can be attributed to the slow C diffusion in Ta and Ta carbide. Furthermore, the suppression of C diffusion at the Ta/foil interface suggests that the Ta foil can protect W matrix during SPS process due to the high thermodynamic stability of Ta carbide compared to that of W carbide. Conversely, C diffused faster not only in the Mo, but also at the Mo/W interface. For this reason, unlike Ta foil, Mo foil is not effective as a C diffusion barrier. Due to the same thermodynamic and kinetic relation of W and C, the Ta foil can be applicable in the Cr system.

2.5. References

- [1] A. Koutsospyros, W. Braida, C. Christodoulatos, D. Dermatas, N. Strigul, A review of tungsten: from environmental obscurity to scrutiny, *J. Hazard. Mater.* 136 (1) (2006) 1–19.
- [2] G. Pintsuk, A. Hasegawa, Chapter 6, in: R.J.M. Konings, R.E. Stoller (Eds.), *Comprehensive Nuclear Materials*, 6, Elsevier, San Diego, 2020, pp. 19–53.
- [3] Y. Oh, N. Kwak, K. Lee, W.-S. Ko, H.N. Han, Ductility enhancement of tungsten after plastic deformation, *J. Alloys Compd.* 787 (2019) 801–814.
- [4] W. Chrominski, L. Ciupinski, P. Bazarnik, S. Markelj, T. Schwarz-Selinger, TEM investigation of the influence of dose rate on radiation damage and deuterium retention in tungsten, *Mater. Charact.* 154 (2019) 1–6.
- [5] M. Kim, S. Kim, J. Kang, S.H. Song, D. Lee, Effects of ZrN and W particle sizes on the mechanical and ablation properties of ZrN/W composites, *Met. Mater. Int.* 25 (3) (2019) 733–739.
- [6] J. Choi, H.-M. Sung, K.-B. Roh, S.-H. Hong, G.-H. Kim, H.N. Han, Fabrication of sintered tungsten by spark plasma sintering and investigation of thermal stability, *Int. J. Refract. Hard Mater.* 69 (2017) 164–169.
- [7] S. Deng, R. Li, T. Yuan, S. Xie, M. Zhang, K. Zhou, P. Cao, Direct current-enhanced densification kinetics during spark plasma sintering of tungsten powder, *Scr. Mater.* 143 (2018) 25–29.
- [8] Y.J. Lee, H.-M. Sung, Y. Jin, K. Lee, C.R. Park, G.-H. Kim, H.N. Han, Improvement of mechanical property of air plasma sprayed tungsten film using pulsed electric current treatment, *Int. J. Refract. Hard Mater.* 60 (2016) 99–103.
- [9] R. Orrù, R. Licheri, A.M. Locci, A. Cincotti, G. Cao, Consolidation/synthesis of materials by electric current activated/assisted sintering, *Mater. Sci. Eng. R Rep.* 63 (4–6) (2009) 127–287.
- [10] H.-J. Jeong, M.-J. Kim, S.-J. Choi, J.-W. Park, H. Choi, V. T. Luu, S.-T. Hong, H.N. Han, Microstructure reset-based self-healing method using sub-second electric pulsing for metallic materials, *Appl. Mater. Today* 20 (2020) 100755.
- [11] M.-J. Kim, S. Yoon, S. Park, H.-J. Jeong, J.-W. Park, K. Kim, J. Jo, T. Heo, S.-T. Hong, S.H. Cho, Y.-K. Kwon, I.-S. Choi, M. Kim, H.N. Han, Elucidating the

origin of electroplasticity in metallic materials, *Appl. Mater. Today* 21 (2020) 100874.

[12] L. Zhong, X. Zhang, S. Chen, Y. Xu, H. Wu, J. Wang, Fe–W–C thermodynamics and in situ preparation of tungsten carbide-reinforced iron-based surface composites by solid-phase diffusion, *Int. J. Refract. Hard Mater.* 57 (2016) 42–49.

[13] J.W. Coenen, Y. Mao, S. Sistla, J. Riesch, T. Hoeschen, C. Broeckmann, R. Neu, C. Linsmeier, Improved pseudo-ductile behavior of powder metallurgical tungsten short fiber-reinforced tungsten (W_f/W), *Nucl. Mater. Energy* 15 (2018) 214–219.

[14] Y. Mao, C. Chen, J.W. Coenen, J. Riesch, S. Sistla, J. Almanstötter, A. Terra, Y. Wu, L. Raumann, T. Höschen, H. Gietl, R. Neu, C. Linsmeier, C. Broeckmann, On the nature of carbon embrittlement of tungsten fibers during powder metallurgical processes, *Fusion Eng. Des.* 145 (2019) 18–22.

[15] D.V. Dudina, B.B. Bokhonov, A.V. Ukhina, A.G. Anisimov, V.I. Mali, M.A. Esikov, I.S. Batraev, O.O. Kuznechik, L.P. Pilinevich, Reactivity of materials towards carbon of graphite foil during spark plasma sintering: A case study using Ni–W powders, *Mater. Lett.* 168 (2016) 62–67.

[16] X. Boulnat, D. Fabrègue, M. Perez, S. Urvoy, D. Hamon, Y. de Carlan, Assessment of consolidation of oxide dispersion strengthened ferritic steels by spark plasma sintering: from laboratory scale to industrial products, *Powder Metall.* 57 (3) (2014) 204–211.

[17] B.B. Bokhonov, A.V. Ukhina, D.V. Dudina, A.G. Anisimov, V.I. Mali, I.S. Batraev, Carbon uptake during spark plasma sintering: investigation through the analysis of the carbide “footprint” in a Ni–W alloy, *RSC Adv.* 5 (98) (2015) 80228–80237.

[18] A.J. Mackie, G.D. Hatton, H.G.C. Hamilton, J.S. Dean, R. Goodall, Carbon uptake and distribution in spark plasma sintering (SPS) processed Sm (Co, Fe, Cu, Zr) z, *Mater. Lett.* 171 (2016) 14–17.

[19] B. Mouawad, M. Soueidan, D. Fabrègue, C. Buttay, V. Bley, B. Allard, H. Morel, Full densification of molybdenum powders using spark plasma sintering, *Metall. Mater. Trans. A* 43 (9) (2012) 3402–3409.

[20] L.V. McCarty, R. Donelson, R.F. Hehemann, A diffusion model for tungsten powder carburization, *Metall. Mater. Trans. A* 18 (6) (1991) 969–974.

[21] G. Mühlbauer, G. Kremser, A. Bock, J. Weidow, W.-D. Schubert, Transition of

W₂C to WC during carburization of tungsten metal powder, *Int. J. Refract. Hard Mater.* 72 (2018) 141–148.

[22] L. Carette, P. Jacquet, D. Cotton, V. Vignal, S. Faure, (TaC/Ta₂C) bilayer formed on carburized and annealed tantalum; development of a numerical growth model, *Appl. Surf. Sci.* 467 (2019) 84–88.

[23] G. Czack, G. Kirschstein, W. tungsten, Supplement Volume A4 Surface Properties. Electron Emission. (Gmelin Handbook of Inorganic and Organometallic Chemistry), eighth ed., Springer, Berlin Heidelberg, 1993.

[24] A.I. Nakonechnikov, L.V. Pavlinov, V.N. Bykov, Diffusion of carbon in refractory metals with a BCC lattice, *Phys. Met. Metallogr.* 22 (2) (1966) 73–77.

[25] A. Shepela, The diffusion of carbon-14 in tungsten and tungsten-rhenium alloys, *J. Less Common Met.* 26 (1) (1972) 33–43.

[26] P.S. Rudman, SOLUBILITY LIMIT AND DIFFUSIVITY OF CARBON IN MOLYBDENUM, *Trans. Metall. Soc. AIME* 239 (1967) 1949–1954.

[27] J. Kunze, W. Reichelt, Untersuchungen über die dekarburierung von kohlenstoffhaltigem molybdän im festen zustand, *J. Less Common Met* 20 (1970) 327–338.

[28] G. Lorang, J.P. Langeron, Diffusion and solubility of carbon in molybdenum and TZM, *High Temp. High Press.* 10 (2) (1978) 165–177.

[29] P. Son, S. Ihara, M. Miyake, T. Sano, *Jpn. I. Met.* 30 (1966) 1137–1140.

[30] P.J. Rodriguez, Characterization and Refinement of Carbide Coating Formation Rates and Dissolution Kinetics in the Ta-C System, Los Alamos National Lab. (LANL), Los Alamos, 1996.

[31] G.V. Samsonov, V.K. Vitryanyuk, F.I. Chaplygin, Tungsten carbides, Kiev: Naukova Dumka (1974) 176.

[32] V.S. Eremeev, P.L. Gruzin, A.S. Panov, Reactive diffusion in the W-C systems, in: *Uses of the Isotope Indicator Technique in Research and Industrial Production* [in Russian], Atomizdat, Moscow, 1971, pp. 60–65.

[33] V.S. Eremeev, A.S. Panov, DIFFUSION OF CARBON IN MOLYBDENUM CARBIDE, *Izv. Akad. Nauk SSSR Neorg. Mater.* 4 (1968) 1507–1512.

[34] R.A. Andrievskii, V.S. Eremeev, V.N. Zagryazkin, Diffusion of carbon in carbides of Groups IV–VI transition metals, *Izv. Akad. Nauk SSSR, Neorg. Mater.* 3 (12) (1967) 2158–2161.

- [35] R.J. Fries, The chemical diffusion of carbon in the group VI-B metal carbide, Metall. Gesellschaft 36 (1968) 31.
- [36] R. Resnick, L. Seigle, Trans. Metall. Soc. AIME 236 (1966) 1732–1738.
- [37] W.F. Brizes, Diffusion of carbon in the carbides of tantalum, J. Nucl. Mater. 26 (2) (1968) 227–231.
- [38] W. Mayr, W. Lengauer, P. Ettmayer, D. Rafaja, J. Baue, M. Bohr, Phase equilibria and multiphase reaction diffusion in the Cr-C and Cr-N systems, J Phase Equilibria Diffus 20(1) (1999) 35-44.

Chapter 3. Fabrication of Cr-W dual-phase Composites

3.1. Introduction

For the next-generation fusion reactor, developing an appropriate structural material for the divertor heat sink is one of the major engineering challenges. To realize the development of advanced materials that can cover the complex interactions between plasma and the materials, following properties should be satisfied as much as possible [1]:

- High thermal conductivity
- High strength and toughness at elevated temperatures
- Ductility
- Sufficient fatigue life
- Corrosion resistance
- Moderate activation level acceptable for recycling
- Moderate swelling
- Low helium transmutation rate
- Moderate irradiation effect and ability of damage recovery
- Low tritium solubility
- Sufficiently high melting point
- Availability and reasonable cost

Surely, a long list of these various requirements can hardly be met with a single material. Therefore, the engineering strategy to develop the materials that satisfy the requirements as much as possible and utilizes them for an appropriate application as a PFM may be of the first importance. As explained above introduction, one of the most important issues for the PFM that should be solved is the brittleness caused by high DBTT. For the brittle W material, once the crack initiates, it can easily propagate through the whole armor block. Failure is usually sudden and catastrophic,

with no significant damage or warning and little residual load-bearing capacity. Structures that satisfy a visual inspection may fail suddenly at loads much lower than expected. Therefore, the materials should have both adequate strength and elongation for the suppression of both crack opening and propagation.

With respect to such limitations, the dual-phase composites so-called tungsten heavy alloys consisting of W powder particles in a matrix of a Ni/Fe alloy [2–5], which is produced by liquid phase sintering have been employed as an alternative divertor target material. However, it is very undesirable from the viewpoint of the neutron irradiation, which Ni becomes long-term neutron activation product. Hence, another element should be considered for the substitution of Ni. Cr can replace this restriction due to the low neutron activation [6, 7]. In addition to that, Cr has been satisfied diverse requirements such as ductility at low temperature, moderate activation, and high corrosion resistance. However, the Cr is known to have low strength at high temperatures. Therefore, the new materials should be developed to satisfy diverse requirements as many as possible. Therefore, in this work, for the first time, we produced Cr-W dual-phase composites which potentially possess both strength of the W and elongation of the Cr.

3.2. Experimental procedures

3.2.1 Materials and methods

Commercially available Cr powder (99% purity, average particle size of 45~150 μm , gas atomized, Goodfellow, UK) and W powder (>99.9% purity, average particle size of $\leq 0.5 \mu\text{m}$, TaeguTec, Korea) were used as a starting material. For the selection of optimal W powder size, the different W powder (>99.9% purity, average particle size of 2.4 and 8 μm , TaeguTec, Korea) was additionally used. A high-energy mill (SPEX 8000D, USA) was used to prepare the Cr-W powder mixtures. To avoid the oxidation of powder mixtures, milling was conducted under an ultra-high-purity argon (Ar) atmosphere (99.9999%) in stainless steel vial without ball. The milling time was carried out for 10 hours based on the point where there is no specific surface changes in microstructure. For pure Cr and W, we used as-received powders without milling.

Subsequently, the Cr-xW (x=10 and 20 vol.%) composites and Pure Cr and W were consolidated by SPS. The compositions of Cr-W composites were selected by the Cr diffusion distance in W and average size of Cr powder. The Cr diffusion distance was estimated by measuring the average length based on the microstructure images sintered at different temperatures and at least 500 positions were considered to obtain a reliable value. The average size of Cr powder was measured using a laser diffraction particle size analyzer (Mastersizer 3000E, Malvern Panalytical, UK). All these optimizations were proceeded with the Cr-to-W ratio of 5 to 5. Based on above reasons, the SPS was performed at an optimized temperature of 1300 $^{\circ}\text{C}$ for Cr and Cr-W composites and 1900 $^{\circ}\text{C}$ for W with a heating rate of 200 $^{\circ}\text{C}/\text{m}$, under an applied stress of 65 MPa for 5 min. The size of samples was consolidated with the diameter of 12 mm for material development and plasma exposure and of 20 mm for mechanical testing. The thickness is all the same of 3 mm. Moreover, the ductility of W and Cr are very sensitive to the C content, we introduced Ta foil in the inner part of the graphite mold as a C diffusion barrier described in [8]. To counter the possibility of oxide formation, all process of SPS was conducted in a reducing atmosphere ($\text{Ar}+3\text{H}_2$).

3.2.2 Characterization

For microstructure observation, the surface of all specimens was carefully polished with colloidal silica. The specimens were observed by using several different types of field-emission scanning electron microscopy (FE-SEM). An SU70 FE-SEM from Hitachi equipped with an EDAX/TSL electron backscatter diffraction (EBSD) system (Hikari, Japan) and Helios Nanolab 600 from FEI equipped with a Ga⁺ focused ion beam (FIB) were used for imaging of the microstructures. In addition, the surface morphology was examined using a LEXT OLS 4000 confocal laser scanning microscope (CLSM) from Olympus. High-angle annular dark-field (HAADF) images and diffraction patterns for each phase were acquired using a JEM-2100F scanning transmission electron microscope (STEM) from JEOL Ltd. Energy dispersive spectroscopy (EDS) was performed to obtain local elemental maps and line scans of W and Cr. The STEM specimens were prepared using a Helios G4 FIB (Thermo Fisher Scientific, USA). X-ray diffraction (XRD) patterns were obtained using a D8-Advance diffractometer (Bruker, USA) with Cu-K α radiation at 40 kV and 40 mA. The specimens were scanned from 30 to 90 ° using a step size of 0.02 ° and time per step of 60 s.

The master sintering curve method was used to estimate the apparent sintering activation energy. For the evaluation, several density profiles as a function of temperature were obtained at different heating rate of 50, 100, and 200 °C/m. The mass density was measured by the Archimedes principle, which describes that the buoyancy force of a body immersed into a liquid medium (G_b) equals to the weight of the liquid medium that the body displaces:

$$G_b = V_b \cdot \rho_f \cdot g \quad (1)$$

In which the V_b is the volume of the body, ρ_f is the density of the liquid medium and g is the gravity constant. In principle, closed porosity is required to realize the measurement.

During the sample density measurement, the buoyancy force of the sample can be calculated by measuring the weight variation when the sample placed in the liquid medium. Together with equation (14) the sample density (ρ_s) can be calculated:

$$\rho_s = m/V_b \quad (2)$$

where m is the mass of the sample. The density measurement is carried out with the help of a precision balance with the density measurement package. The fluid medium is pure Ethanol (99.5%). The relative sample density can be then calculated:

$$\rho = \rho_s/\rho_i \quad (3)$$

in which ρ is the relative sample density, ρ_i is the ideal density. Ideal density of pure tungsten and pure chromium was used as 19.25 and 7.14 g/cm³, respectively. the theoretical density of Cr-10W and Cr-20W is roughly estimated by the mixture rule and the estimated value is 8.351 and 9.562 g/cm³, respectively.

During the measurement, it has been observed the measured weight starts to change slowly and continuously after immersing the sample in the Ethanol. This is because the open pores are filled with the ethanol. To obtain the valid measurement, the measured weight is recorded after the samples is immersed in the ethanol for 120 s. In this way, only limited open pores are filled by the ethanol, but the surface is also well wetted.

3.3. Results and discussion

3.3.1 The powder size and milling times

To observe the effect of the Cr diffusion on the densification of different size of W powder, we observe the diffusion distances sintered at 1300 °C for 5 min using W powder of 0.5, 2.4, and 8 μm sizes. The use of W powder with 0.5 μm showed a distinctively different microstructure compared to that of 2.4 and 8 μm . This could be seen clearly from a diffusion enhanced zone in the W region. Figure 12 (a–c) show SEM images of W powder with 0.5, 2.4, and 8 μm sintered at 1300 °C for 5 min and the corresponding enlarged areas marked by green lines are shown in Figure 12 (d–e). The densification enhanced zones in W are located at the interface of Cr particles of each SEM image (The densification enhanced zones are marked by yellow dashed lines, respectively). The W powder with 0.5 μm has an approximately 5 μm thick diffusion enhanced zone (Figure 12 (d), boundary between the W matrix and Cr particles is indicated by the yellow arrow). This densification enhanced zone became thinner as the size of W powder was larger with 2.4 μm . Here, the thickness of the densification enhanced zone becomes approximately 1.5 μm (Figure 12 (e)). However, for the case of W powder with 8 μm , there is no densification enhanced zone observed in W region. From these results, the use of W powder having large particle size is not effective to enhance the sinterability of W. In this regard, the grain boundaries in the initial powder agglomerates considered as a fast diffusion path during sintering, and a smaller powder that has a large surface area can accelerate this. With that, we used the W powder with 0.5 μm to maximize the densification during sintering cycle. Furthermore, the use of the W powder with 0.5 μm can effectively maximize the hardness compared to the other sizes of W powder because it would correspond to the small grain size when the composites are consolidated.

Cr and W powders were mechanically milled through a high-energy milling equipment. To determine proper milling time, we used the content of Cr at 50 vol.%, which the content of W is quite enough to cover the Cr powder. Figure 13 shows the SEM images of as-received Cr and W powders and Cr-50W powder mixtures as a function of milling time (Figures 13 (a) and (b) are as-received Cr and W powders,

respectively). With 1 h milling time, the W appears to be smoothly coated on the Cr surface (Figure 13 (c)), and the coated layers are gradually thickened. After 5 h milling, the thickened layers are rough and uneven, as shown in Figure 13 (d). However, once the milling time was reached at 10 h, the thickened layers become rough and even (Figure 13 (e)) and it is shown that further milling up to 20 h was no longer effective (Figure 13 (f)). Therefore, a baseline was set with the same milling time for 10 h based on the microstructure with no changes in the thickened layers.

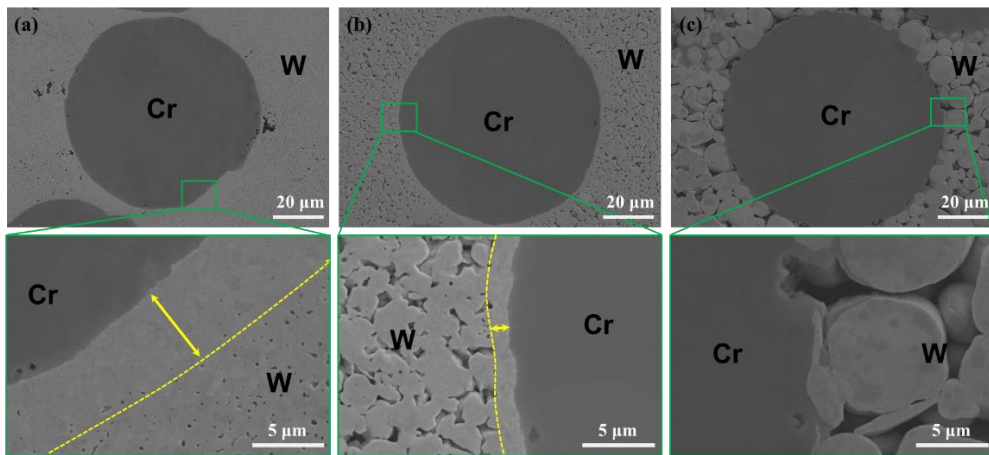


Figure 12 The densification enhanced zones depending on the W powder size. (a) with 0.5 μm , (b) with 2.4 μm , and (c) with 8 μm . Yellow areas indicated diffusion enhanced zones in W.

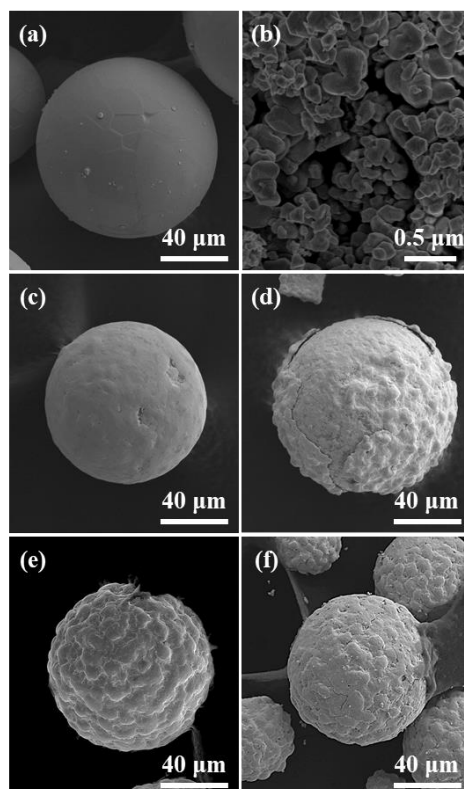


Figure 13 Powder morphology evolution during mechanical milling. As-received (a) Cr powder and (b) W powder and mechanically milled at (c) 1 h, (d) 5 h, (e) 10 h, and (f) 20 h.

3.3.2 The optimization of sintering temperature and W addition level

Since this thesis is concerned with development of Cr-W dual-phase composites, the SPS temperature should be determined, which can maximize the independent properties of W and Cr. We therefore are interested specifically in the temperature at which the sinterability of W can be enhanced while the diffusion of W into Cr is minimized. Again, the composition used here was the same as the content of Cr at 50 vol.%. To optimize the SPS temperature, we SPSed the Cr-W powder mixtures at the temperatures ranging from 1100 to 1500 °C. The soaking time was all set as 5 min. Figure 14 shows the SEM images of Cr-50W composites SPSed at 1100, 1200, and 1300 °C. Here, the densification enhanced zone in W were estimated over 500 positions based on the microstructures. It is shown that the thickness of densification enhanced zone increases with increasing SPS temperatures. The densification enhanced zone SPSed at 1100 °C was shown with a high porosity, and the thickness was estimated as $2.2 \pm 1.6 \mu\text{m}$ (Figure 14 (a, d)). At the temperature SPSed at 1200 °C, the thickness was similarly estimated as $2.3 \pm 1.5 \mu\text{m}$ with the temperature SPSed at 1100 °C, but the dense microstructure is shown in the diffusion enhanced zone (Figure 14 (b, e)). The SPS temperature with 1300 °C increased the thickness of this zone up to $5.9 \pm 1.6 \mu\text{m}$ (Figure 14 (c, f)), confirming the possibility to promote the densification of Cr-W dual-phase composites at the specific composition of interest. Following results in Figures 15 and 16 show the XRD and SEM-EDS results SPSed at 1300 to 1500 °C. In SPSed at 1300 °C, the peak shift in Cr was almost not visible, which is also consistent with the EDS mapping. However, it was found that the peak shift in Cr toward W start to be detected from the SPS temperature at 1400 °C. This peak shift is more noticeably detected SPSed at 1500 °C. The peak shift of Cr in Cr-W composites is mainly due to the W diffusion into Cr, which is also confirmed by the EDS mapping. In Figure 16 (b), the W element is detected even deep in the center of Cr particles, unlike the results SPSed at 1300 °C. In this regard, the SPSed temperature should carefully be considered for the sake of not having undesired behavior in Cr particles, and therefore the SPS temperature here is set to 1300 °C which is desirable to accelerate consolidation of W without losing the Cr properties.

Apart from the varying the sintering parameters, the selection of composition to have higher densities for Cr-W dual-phase composites is also important in order to achieve the desired properties. The initial Cr powder has a wide size distribution, as shown in Figure 17. Here, the D_{10} , D_{50} , and D_{90} are percentile values which are statistical parameters that can be read directly from the cumulative particle size distribution. They represent the size below which 10, 50, and 90% of all particles are found – D_{50} is known as the median powder size by volume. Based on the median size of 92.1 μm and the diffusion distances of Cr in W, we considered a Cr-to-W ratio of approximately up to 8:2. The ratio of Cr-W composites at the given system was estimated based on the following assumption as

$$\frac{4}{3}\pi r^3 : \frac{4}{3}\pi(R^3 - r^3) \rightarrow r^3 : (r + x)^3 - r^3 \quad (4)$$

where r is the radius of Cr, R is the radius of Cr and densification enhanced zone in W, and x is the diffusion distance of Cr in W. Equation (4) becomes shortened as follow:

$$Cr : W = \frac{r^3}{(r+x)^3} : \frac{(r+x)^3 - r^3}{(r+x)^3} \quad (5)$$

With the use of the densification enhanced zone sintered at 1300 °C and the mean powder size of Cr, the estimated values for Cr : W ratio using this calculations is 7.68 : 2.32, which means the Cr particles can cover the max 23.2 volume % W for the densification. Therefore, the selected composition of Cr-W dual-phase composites in this study was Cr-10 vol.% W and Cr-20 vol.% W, which can cover all the W present in Cr-W dual-phase composites.

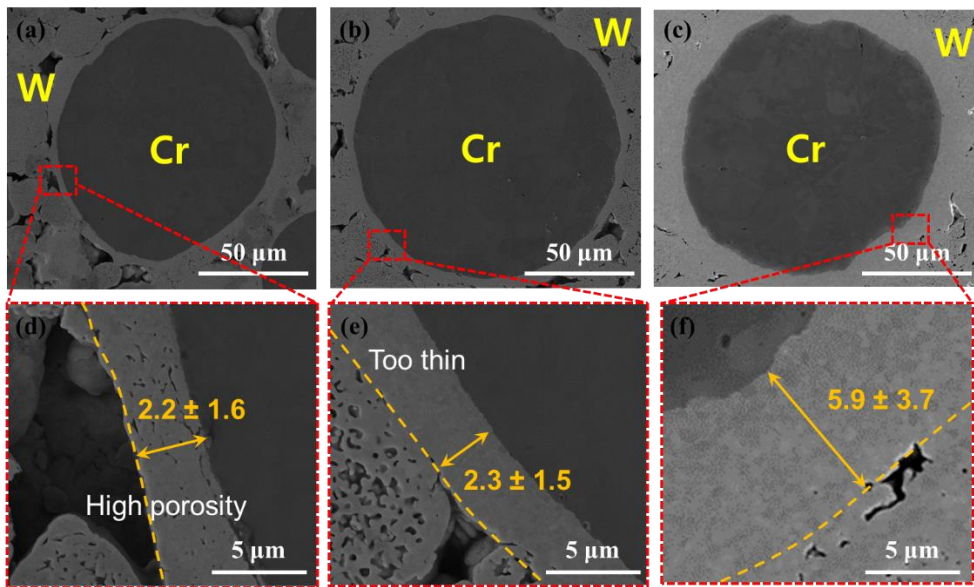


Figure 14 The Cr diffusion distances in W depending on different sintering temperatures. (a), (d) 1100 °C, (b), (e) 1200 °C, and (c), (f) 1300 °C

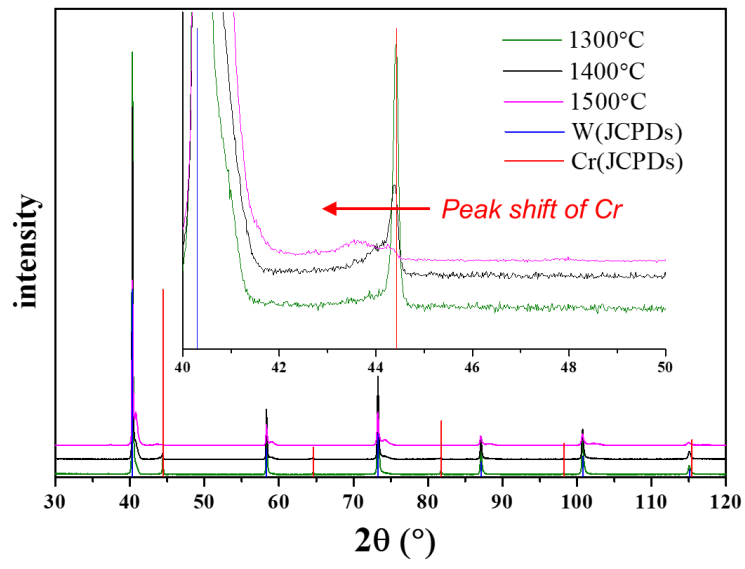


Figure 15 XRD patterns of Cr-W composite with different sintering temperature.

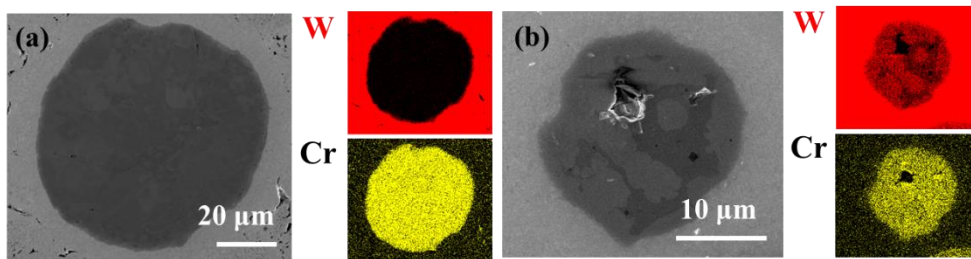


Figure 16 SEM-EDS mapping results. Sintered at (a) 1300 °C, (b) 1500 °C.

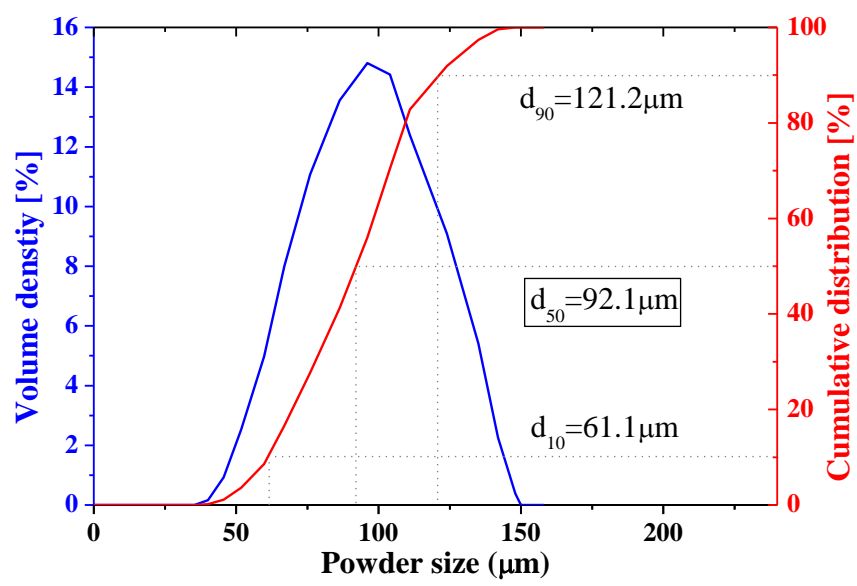


Figure 17 Powder size distribution of as-received Cr powder.

3.3.3 Initial microstructures and basic properties

As explained in the aforementioned results, the Cr-10W and Cr-20W were fabricated at the sintering temperature of 1300 °C for 5 min, together with pure Cr and W for the comparison. Since it is difficult to obtain dense microstructure for pure W at the 1300 °C, the SPS of pure W was employed at the 1900 °C for 5 min.

The microstructures of bulk samples are displayed in Figure 18. SEM images and EBSD inverse pole figure (IPF) maps consolidated using different powders are presented in Figures 18 (a–d) and Figure 18 (e–h), respectively. The pure Cr sample showed a coarse-grained (CG) and uniform microstructures with an average grain size of 32.1 μm , and it has a wide distribution of grain (Figure 18 (a, e)). In addition, some micron-sized pores are observed in the microstructures, as marked by orange arrows. In contrast, the Cr-10W exhibits a unique microstructure in which dark grey particle are surrounded by bright grey network that is continuously connected in a three-dimension (Figure 18 (b)). In the Cr-20W, the volume fraction of bright grey network was increased, maintaining the unique three-dimensional network structure, as shown in Figure 18 (c). Here, the bright grey network represents W region, while the dark grey particles indicate Cr region. The EBSD IPF maps in Cr-W composites provides a grain size information of each phase. The W region in Cr-W composites is mainly comprised of equiaxed ultra-fine grained (UFG) with a mean grain size of $<0.8 \mu\text{m}$. Similar to the pure Cr, the Cr regions in Cr-10W and Cr-20W have a CG and homogeneous microstructures with a wide grain size distribution, and their mean grain size was relatively about 28.6 and 27.7 μm , respectively. The Cr/W interface region in Cr-20W composite was further observed at much higher magnification, as shown in Figure 18 (i). Here, we can observe this unique microstructure more in detail, which CG Cr is surrounded by the UFG W. For pure W as shown in Figure 18 (h), it has a grain size of approximately 14.7 μm and a homogeneous microstructure with a narrow grain size distribution is observed. The differences of W grain size with Cr-W is attributed by the SPS temperature consolidated at 1900 °C. Figure 18 (j) summarized all the grain size of each phase and its corresponding hardness ($\text{HV}_{0.1}$). The trends of grain size are observed same as aforementioned results, and the hardness profiles show the differences among the samples, significantly. The W

phase in Cr-W composites exhibit over 700 HV_{0.1}, while the hardness of W in pure W shows about 465.7 HV_{0.1}, which was directly contributed by their grain size differences. The hardness of Cr is all shown to be approximately 180 HV_{0.1} for all samples, which is affected by their grain size that is within a similar range.

Apart from the basic properties of each phase, the bulk hardness and density of all samples prepared from various powders were provided, as shown in Figure 19. The average density of Cr, Cr-10W, Cr-20W, and W is 99.1, 99.9, 99.5, and 99.1%, respectively (Figure 19 (a)). All system can be achieved to nearly full densification after consolidation. The small differences of density among the samples seem to be contributed by the packing of the initial powder compacts. Because W in Cr-W powder mixtures can fill the open spaces between the Cr particles. From this, the rapid diffusion can easily be achieved and the sinterability for Cr-W composites can be accelerated. The bulk hardness of all samples is dependent on the W content, as shown in Figure 19 (b). However, it was confirmed that the increase in hardness of Cr-W composite was significantly observed as the W content increased, which was attributed by the UFG W. Therefore, benefiting from the unique microstructures comprised of UFG W and CG Cr, the Cr-W composites has a good advantage in terms of achieving high hardness as well as high densification.

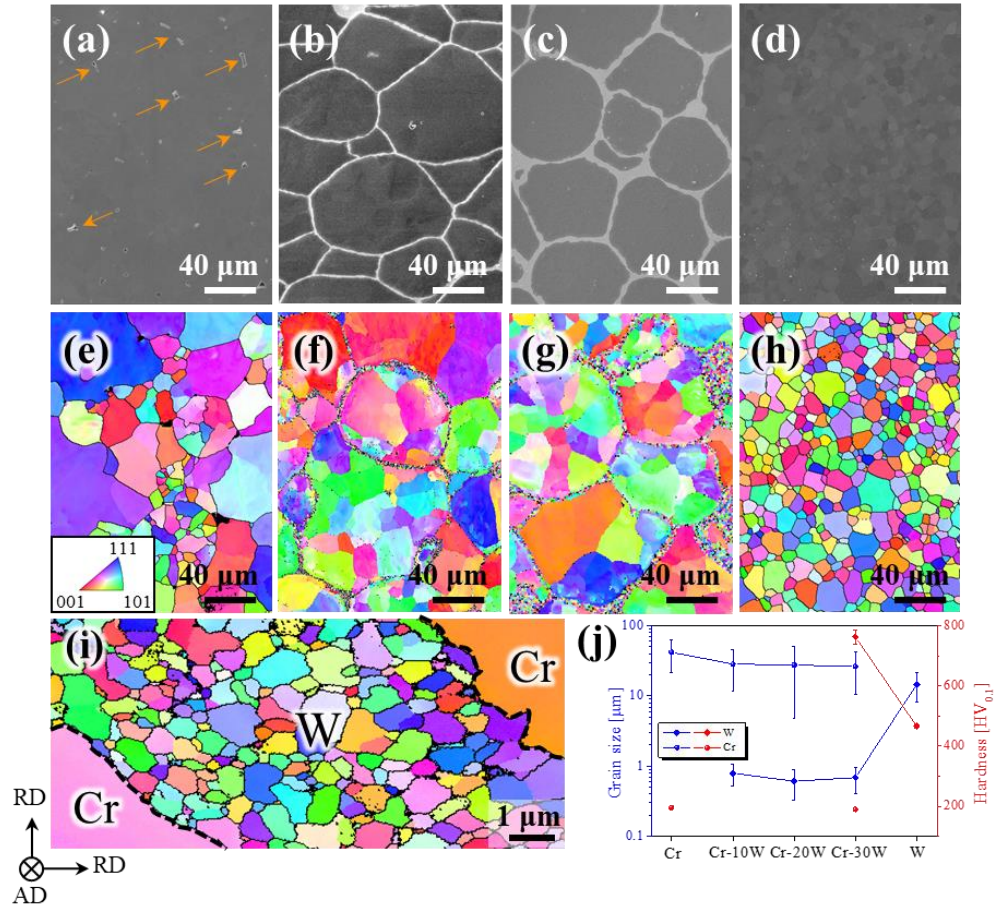


Figure 18 SEM+EBSD IPF maps and corresponding grain size and hardness maps of each phase for the bulk samples: (a, e) Cr; (b, f) Cr-10W; (c, g) Cr-20W and (d, h) W. (i) EBSD IPF map of the Cr/W interface region in the Cr-20W sample. (j) Grain sizes and hardness (HV_{0.1}) of W and Cr each phase with respect to composition. Orange arrows in (a) indicates micron-sized pores.

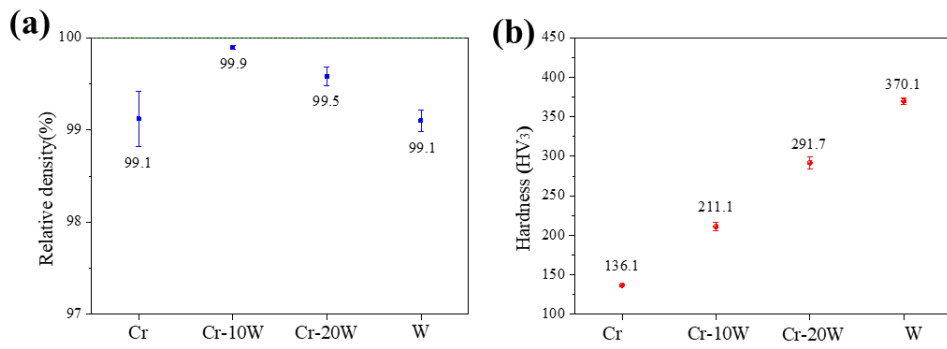


Figure 19 (a) Density and (b) Hardness of the bulk specimens

3.3.4 Cr/W interface characterization

To understand how the densification of W are enhanced at the Cr/W interfaces, we performed the microstructural characterization by STEM-HAADF analysis with thermodynamic characteristics aligning with those of the equilibrium W-Cr phase diagram. Figure 20 (a) shows the STEM-HAADF images of Cr/W interface in Cr-20W composite and the corresponding diffraction patterns of selected areas 1 and 2 are shown in Figure 20 (b, c). The selected area 1 exhibits diffraction rings from a W BCC solid solution while Cr's is not visible, suggesting that Cr atoms are dissolved into W. This can be confirmed by the STEM-EDS results obtained by the composition line scan and mapping. The elemental maps show the distribution of Cr in W and the concentration of Cr diffused in W is approximately 20 at.% by line scan. The Cr diffusion profile in W is uniform along the line scan of the specimen. This composition is also in the reliable ranges with the composition in solubility maps from W-Cr phase diagram (Figure 21). Here, the solubility of Cr in W is approximately 18.6 at.% at 1300 °C, and the slightly higher W content in Cr would be attributed by the effect of electric current. M. Park et al [9]. revealed the sintering mechanism that densification in the W-Cr system can be achieved at a low sintering temperature with the rapid rate. This is because the Cr phase separation at the W interface generates fast diffusion path for W atoms. Therefore, once the Cr-rich phase has been poised at the W inter-particle neck, the solubility of W in the neck increases as temperatures increases, suggesting that it is capable of dissolving W atoms and providing a transport pathway [10]. Here, the enhanced sinterability of W in the Cr/W composites would be the effect of Cr atoms that poised at the W inter-particle neck, which enables to sinter the Cr-W composites at such a low temperature. In the selected area 2, the diffraction pattern is shown with a Cr BCC solid solution while W's is not visible. Unlike the W and Cr did not show the high W content but gradient concentration profiles were observed from the Cr/W interface, as shown in the results of composition line scan and mapping. Although the diffusion of W was made at the Cr/W interface, the W did not diffuse deep in the Cr. Therefore, we believe the Cr particles still have the potential to behave its function properly.

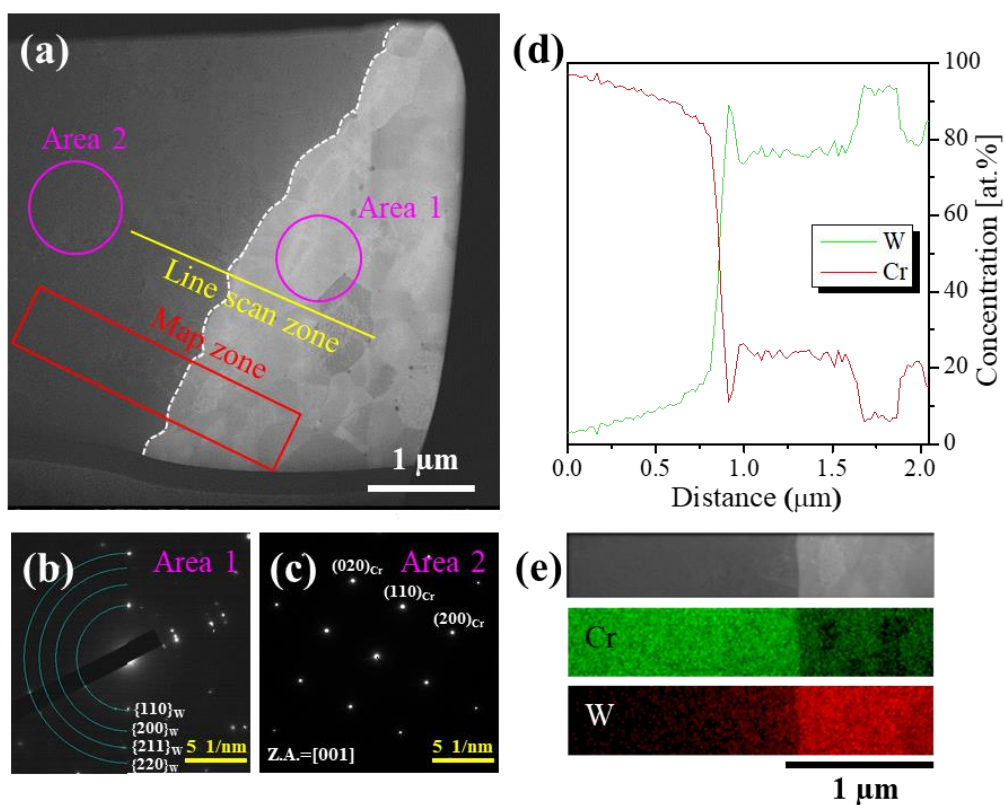


Figure 20 STEM-HAADF Images of Cr-20W interface are shown in (a) and corresponding diffraction patterns of different area 1 and 2 are shown in (b) and (c). EDS Line scan and mapping marked by yellow line and red box in (a) are shown in (d) and (e), respectively.

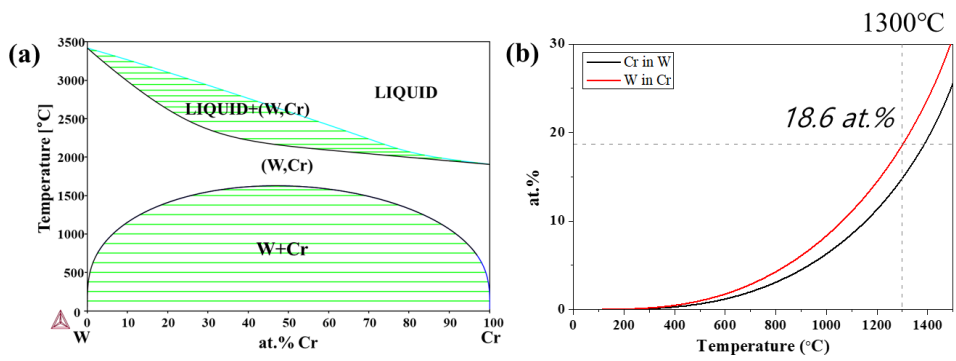


Figure 21 (a) W-Cr phase diagram, (b) The solubility of Cr in W and W in Cr. The solubility on Cr in W at 1300 °C is approximately 18.6 at.%.

3.3.5 Sintering kinetics

To assess the sintering kinetics, the determination of shrinkage curves is priority work that needs to be performed. For the development of time-dependent relative density curves, actual shrinkage data of the given powder compact was required. In SPS, the axial displacement data of the bottom punch during sintering of the powder can be recorded. However, in order to obtain a reliable result, the thermal expansion of graphite mold (die and punches) and samples should be taken into account. For this, the entire graphite mold was cooled down to room temperature and reheated to the target temperature with same sintering cycle, keeping the sintered compact inside the mold. Therefore, the displacement recorded in this second cycle corresponds only to the thermal expansion of the graphite mold and samples. The length of the sintered sample was measured after the first and second run and found to be nearly the same, indicating that no further densification of the sintered sample occurred during the second run. Finally, the powder shrinkage data were obtained by subtracting the thermal expansion of the graphite mold and samples during the second run from the original displacement data in the first run. The schematic raw data for sintered compact and the graphite mold are shown in Figure 22 (a). In terms of the die displacement, positive values indicate shrinkage while negative values indicate expansion. The powder shrinkage curve (black line) was obtained by subtracting the graphite expansion curve (blue line) from the original total specimen plus graphite shrinkage curve (red line).

With regard to the actual shrinkage evolution, the final height of sintered compact was measured. Then, the time-dependent relative density data was calculated based on the following equations:

$$\rho_i = \frac{(\rho_f l_f)}{l_f - h_i} \quad (6)$$

where ρ_i is the instantaneous relative density, ρ_f is the final density which is measured by the Archimedes method, l_f is the final length of the sintered pellet, l_i is the instantaneous length, and h_i is the displacement difference between final state and instantaneous state, i.e., actual shrinkage curve can be read from Figure 22 (a). These

data will be used in the following master sintering curve (MSC) construction.

We identify the characteristic atomic processes which form the rate-limiting step during sintering by determining the sintering activation energy, and corroborate the proposed sintering mechanism. To determine the sintering activation energy, the master sintering curve method [11, 12] was employed. The master sintering curve is developed based on the combined-stage sintering model [13] and the atomic flux contributing to filling the pores is related to instantaneous shrinkage rate of a compact.

$$-\frac{dL}{Ldt} = \frac{\gamma\Omega}{kT} \left(\frac{\delta D_b \Gamma_b}{G^4} + \frac{D_v \Gamma_v}{G^3} \right) \quad (7)$$

where γ is the surface energy, Ω is the atomic volume, k is the Boltzmann constant, T is the temperature, G is the average particle or grain size, ρ is the relative density, t is time, δ is the grain boundary thickness, D_v and D_b are the coefficients for volume and grain boundary diffusion, Γ is a parameter which relates the driving force, mean diffusion distance, and other geometric features of the microstructures. Assuming isotropic shrinkage, Eq. (7) can be related to the integral form of the instantaneous densification rate as follows:

$$\Phi(\rho) \equiv \frac{k}{\gamma\Omega D_0} \int_{\rho_0}^{\rho} \frac{(G(\rho))^n}{3\rho\Gamma(\rho)} d\rho \quad (8)$$

$$\Theta(t, T(t)) \equiv \int_0^t \frac{1}{T} \exp\left(-\frac{Q}{RT}\right) dt \quad (9)$$

where Q is the sintering activation energy, R is the gas constant, ρ is the relative density, $(D_v)_0$ and $n = 3$ for volume diffusion, and $D_0 = (\delta D_b)_0$ and $n = 4$ for grain boundary diffusion. Eq. (8) can be rearranged into an equivalence of two terms: one including all microstructural and materials properties (Eq. (8)) and the other which depends only on Q and the heating time- temperature profile, $T(t)$ (Eq. (9)). If a single sintering activation energy exists, then the correct value of Q will collapse all the heating profiles of Eq. (8) onto a single curve. To assess the sintering activation energy in the SPSed Samples, the mean residual squares of the fitting process as a

function of Q were employed [14], as shown in Figure 22 (c). Figure 22 (d) illustrates normalized heating profiles at sintering activation energies denoted in Figure 22 (c). The best convergence of heating profiles to a single curve occurs for a sintering activation energy of Cr, Cr-10W, Cr-20W, and W is 449, 451, 455, and 556 kJ/mol (Table 3). The activation energies obtained for pure Cr is close to that for Cr self-diffusion [15], 442 kJ/mol. The effect of electric current is known to reduce the activation energy because the mobility of atoms is kinetically enhanced. This phenomenon is more accelerated if the defects in the material are highly saturated [16, 17]. In powder metallurgy process, the most of the defects that exist in the system corresponds to the grain boundary where the effect of electric current can be maximize. However, the Cr powders used here is spherical powder with relatively large size, and the defect density will not be the as many as the conventional powder that has a high surface area. Therefore, the effect of electric current in the Cr powder compact can be minimal and this could be one of the reasons that cannot reduce the activation energy much in pure Cr system. Unlike this, the activation energy assessed for pure W is minimum value compared to the W self-diffusion, 550-670 kJ/mol [18]. This could be attributed by a small W powder size of $<0.5\mu\text{m}$ that has a high surface area, which the effect of electric current can be significant. In Cr-10W and Cr-20W composites, three activation energies will contribute the total activation energy in Cr-W because Cr is all isolated by the W network in this composite. The activation energies are higher than W diffusion in Cr, 386 ± 33 kJ/mol [19] which is lower than Cr diffusion in W, 547 kJ/mol [20] and even farther from that for W self-diffusion. The W self-diffusion would not be effective since the sintering was employed only at 1300 °C which temperature is difficult to densify the pure W. Therefore, the total kinetics may mainly be affected by the W diffusion in Cr and Cr diffusion in W, which assessed activation energies are in-between value as 451 and 455 kJ/mol for Cr-10W and Cr-20W, respectively. Although the dominant diffusion for densification in this study is difficult to conclude, the diffusion of Cr phases in W neck is a fundamental factor controlling sintering, providing a fast diffusion pathway for Cr to W and vice versa. Therefore, Cr-W composites exhibit a good sinterability at low temperature to the level of pure Cr, unlike pure W sintering itself.

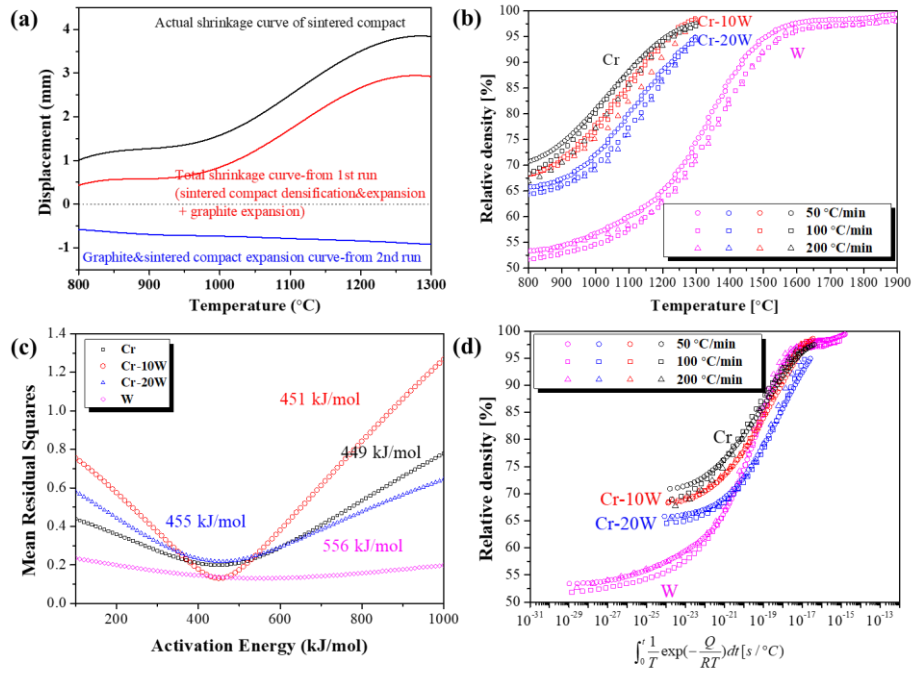


Figure 22 (a) Shrinkage curves of sintered compact and graphite during SPS. The actual shrinkage curve is obtained by subtracting graphite expansion from total shrinkage curve. (b) Evolution of relative density as a function of temperature for Cr, Cr-10W, Cr-20W, and W. (c) The mean residual squares as function of sintering activation energy. (d) normalized heating profiles at the best convergence activation energy denoted in (c).

Table 3 Activation energies obtained by MSC curves (up) and references (down)

	Cr	Cr-10W	Cr-20W	W
Activation energy (kJ/mol)	449	451	455	556
	W in Cr ^[19]	W in W ^[18]	Cr in W ^[20]	Cr in Cr ^[15]
Activation energy (kJ/mol)	386±33	550-670	547	442

3.4. Conclusion

A new Cr-W dual-phase composites were fabricated via mechanical milling and subsequent spark plasma sintering. By introducing W into Cr as a sintering additive, the sinterability of W was accelerated by the Cr diffusion, while the W diffusion in Cr is minimized. The sintering parameters are systematically optimized. The enhancement of sinterability can be maximized with the smallest powder of $<0.5\mu\text{m}$, which cannot be achieved with large powders. With the experimental results for the diffusion distances and the mean powder size of Cr, the optimum composition was decided as Cr-10W and Cr-20W in vol.%. From the microstructural analysis and thermodynamic understanding aligning with phase diagram, we understood the sinterability of W in Cr is enhanced due to the Cr diffusion into W. To assess the sintering kinetics by using master sintering curve, the densification curves as a function of temperature at the different heating rates are obtained from the shrinkage curves. The apparent activation energies are assessed to understand the sintering behavior of Cr-W composites. Although it is difficult to conclude the dominant diffusion for densification in this study, the Cr diffusion in W neck is a fundamental factor controlling sintering and provides a fast diffusion pathway for Cr to W and vice versa. Finally, Cr-W composites exhibit good sinterability at low temperature to the level of pure Cr, unlike pure W sintering itself.

3.5. References

- [1] J.-H. You, A review on two previous divertor target concepts for DEMO: mutual impact between structural design requirements and materials performance, *Nucl. Fusion* 55(11) (2015) 113026.
- [2] Y. Şahin, Recent progress in processing of tungsten heavy alloys, *J. Powder Technol.* 764306 (2014) 22.
- [3] J.K. Park, S.-J.L. Kang, K.Y. Eun, D.N. Yoon, Microstructural change during liquid phase sintering of W–Ni–Fe alloy, *Metall. Trans. A* 20(5) (1989) 837–845.
- [4] J.V. Haag IV, D.J. Edwards, C.H. Henager Jr, W. Setyawan, J. Wang, M. Murayama, Characterization of ductile phase toughening mechanisms in a hot-rolled tungsten heavy alloy, *Acta Mater.* 204 (2021) 116523.
- [5] M.E. Alam, G.R. Odette, On the remarkable fracture toughness of 90 to 97W–NiFe alloys revealing powerful new ductile phase toughening mechanisms. *Acta Mater.* 186 (2020) 324–340.
- [6] D. Terentyev, T. Khvan, J.-H. You, N. Van Steenberge, Development of chromium and chromium-tungsten alloy for the plasma facing components: Application of vacuum arc melting techniques, *J. Nucl. Mater.* 536 (2020) 152204.
- [7] R. Wadsack, R. Pippan, B. Schedler, The effect of pre-deformation on the ductility of chromium, *J. Nucl. Mater.* 307 (2002) 701–704.
- [8] N. Kwak, G. Min, Y. Oh, D.-W. Suh, H.C. Kim, S.-G. Kang, H.N. Han, Tantalum and molybdenum barriers to prevent carbon diffusion in spark plasma sintered tungsten, *Scr. Mater.* 196 (2021) 113759.
- [9] M. Park, C.A. Schuh, Accelerated sintering in phase-separating nanostructured alloys, *Nat. Commun.* 6(1) (2015) 1–6.
- [10] P.E. Turchi, L. Kaufman, Z.K. Liu Modeling of Ni–Cr–Mo based alloys: Part I—phase stability, *Calphad* 30(1) (2006) 70–87.
- [11] T. Frueh, I.O. Ozer, S.F. Poterala, H. Lee, E.R. Kupp, C. Compson, J. Atria, G.L. Messing, A critique of master sintering curve analysis, *J. Eur. Ceram. Soc.* 38(4) (2018) 1030–1037.
- [12] H. Su, D.L. Johnson, Master sintering curve: a practical approach to sintering, *J. Am. Ceram. Soc.* 79(12) (1996) 3211–3217.

- [13] J.D. Hansen, R.P. Rusin, M.H. Teng, D.L. Johnson, Combined-stage sintering model, *J. Am. Ceram. Soc.* 75(5) (1992) 1129–1135.
- [14] D.C. Blaine, S.J. Park, R.M. German, P. Suri, Application of work-of-sintering concepts in powder metals, *Metall. Mater. Trans. A* 37(9) (2006) 2827–2835.
- [15] J.N. Mundy, H.A. Hoff, J. Pelleg, S.J. Rothman, L.J. Nowicki, F.A. Schmidt, Self-diffusion in chromium, *Phys. Rev. B Condens. Matter* 24(2) (1982) 658.
- [16] M.-J. Kim, S. Yoon, S. Park, H.-J. Jeong, J.-W. Park, K. Kim, J. Jo, T. Heo, S.-T. Hong, S.H. Cho, Y.-K. Kwon, I.-S. Choi, M. Kim, H.N. Han, Elucidating the origin of electroplasticity in metallic materials, *Appl. Mater. Today* 21 (2020) 100874.
- [17] H.-J. Jeong, M.-J. Kim, S.-J. Choi, J.-W. Park, H. Choi, V. T. Luu, S.-T. Hong, H.N. Han, Microstructure reset-based self-healing method using sub-second electric pulsing for metallic materials, *Appl. Mater. Today* 20 (2020) 100755.
- [18] J.N. Mundy, S.J. Rothman, N.Q. Lam, H.A. Hoff, L.J. Nowicki, Self-diffusion in tungsten. *Phys. Rev. B Condens. Matter* 18(12) (1978) 6566.
- [19] M. Park, K.C. Alexander, C.A. Schuh, Diffusion of tungsten in chromium: Experiments and atomistic modeling, *J. Alloys Compd.* 611 (2014) 433–439.
- [20] S. M. Klotzman, V.M. Koloskov, S.V. Osetrov, I.P. Polikarpova, G.N. Tatarinova, A.N. Timofeyev, Chromium and Molybdenum Diffusion in Tungsten Single-Crystals, *Phys. Met. Metallogr.* 67(4) (1989) 136–143.

Chapter 4. Characterization of Cr-W dual-phase Composites

4.1. Introduction

In order to be able to use as key components in magnetic fusion reactors, such as the divertor or the plasma-facing materials (PFMs), the aforementioned properties including low activation, high melting point, good thermomechanical properties, low sputter erosion, and low tritium retention are very important. In addition to those properties, the moderate fracture toughness with strength at high temperatures are stringently necessary to be usable in operating temperature window. W is the leading PFM candidate because of its various advantages such as high melting point, low erosion rates, and small tritium retention, but its brittleness, activation, and corrosion issues severely restrict application as PFM. Therefore, for DEMO divertor, Cr and Cr-based alloys have attracted considerable attention as promising candidate to substitute W-based materials, as they possessed the desired properties such as ductility at low temperature, moderate activation level, and excellent corrosion resistance, which W didn't have. However, the relatively low melting point and erosion behavior by intense plasma restrict the use of Cr as a direct heat flux region. Therefore, the concept that a Cr is utilized as a mid-heat flux region with the W coating on the top. The concept of mock-up for PFM is shown in Figure 23. To securely use Cr as a PFM, there needs also a certain degree of hardness that can resist to stress generated by high heat load. In this chapter, Cr-W dual-phase composites were assessed to confirm their potential use in fusion applications, together with pure Cr and W for comparison. The materials were prepared via mechanical milling and subsequent spark plasma sintering, as described in previous Chapter 3. The characterization was investigated for the mechanical strength and ductility and deuterium retention behaviors.

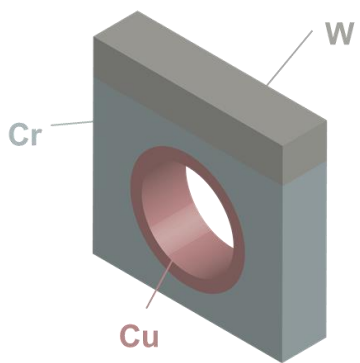


Figure 23 The concept of applying Cr-based materials to the middle heat flux region of mock-up

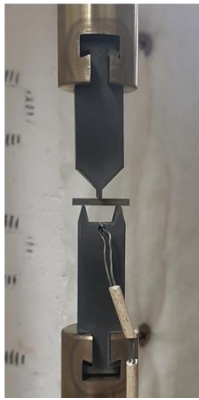
4.2. Experimental procedures

4.2.1 Materials and methods

4.2.1.1 Mechanical test (3-point bending test)

After the fabrication process, mechanical testing is performed for the as-fabricated samples. A 3-point (3PB) bending test is chosen to investigate the flexural strength and strain. Sample dimensions are $16 \times 1.5 \times 1 \text{ mm}^3$ (length \times width \times thickness, manufactured by electro discharge machining). The 3-point bending tests are performed by using an Instron 5584 universal testing machine together with a miniaturized 3-point bending pin system specially designed according to ASTM D790. The tests were performed in air in the temperature at RT and 300 °C (near DBTT). The temperature was measured with the thermocouple by drilling a gouge into the support. The pin-roller diameter is 0.5 mm. The strain rate is set to 10^{-5} s^{-1} . During the tests, the sample is set on two support pins with a distance of 10 mm. A pressing load from 1 load pin is applied in the middle of the sample. The configuration of 3PB bending tester are shown in Figure 24. The load pins move with a constant speed during the test. The load-displacement data of the test is record.

(a)



(b)

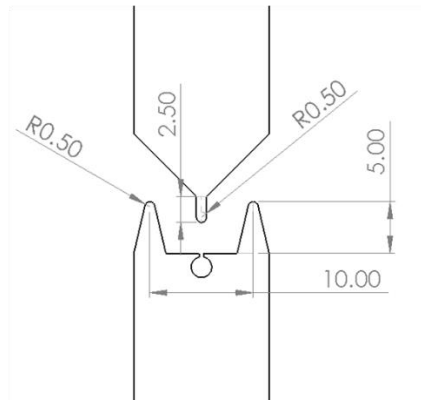


Figure 24 (a) Three-point bending test configuration with the specimen on it; (b) Schematics of the bending configuration and geometry with size.

4.2.1.2 Deuterium retention behaviors

The study of D retention in the SPSed samples (Cr, Cr-20W, and W) has been carried out in three series, following the same experimental procedure. The samples are finely polished with colloidal silica and annealed in vacuum for 2 h at 923 °C to outgas unnecessary gas, i.e., H, O, and etc. To understand deuterium (D) retention behavior of all specimens, we used plasma source device ‘PlaQ’ and ion source device ‘SIESTA’ described in [1, 2]. The ‘PlaQ’ device is a remote electron cyclotron resonance (ECR) discharge with a biased sample holder and allows for high particle flux densities to the target samples in the desired particle energy. However, the presence of impurities, multiple ion species and a not easily determinable flux of energetic neutrals along with the intrinsic energy spread of the particles can make the quantitative analysis of results difficult. In contrast, ‘SIESTA’ device has a number of distinct advantages over plasma devices, producing a mono-energetic beam which can be mass-filtered with magnetic sector fields, allowing for well-defined experiments. These differences allow ‘PlaQ’ device to use particle energies in the low energy region, while the ‘SIESTA’ device can be used in the high energy region. In this study, we used ‘PlaQ’ and ‘SIESTA’ devices for the energy of 10 and 200 eV/D, respectively. The energies were selected based on the SDTrimSP simulations [3], considering the sputtering threshold of Cr and W. The sputtering threshold for Cr and W is 40 and 230 eV/D, respectively, based on the simulation results, as shown in Figure 25. With these energies, the energy with 10 eV/D would not sputter the Cr atoms during exposures, while the energy with 200 eV/D would severely sputter the Cr atoms, but not W atoms. Based on the ITER specification, the fluence for D retention should satisfy the $\sim 10^{24}$ D/m² as much as possible. Therefore, the fluences were selected over 10^{24} D/m². Since the presence of impurities has an adverse effect on the D exposures in low energy [4], the comparable fluences were selected in terms of D retention for energies of 10 and 200 eV with 4×10^{24} and 4×10^{25} D/m², respectively. D loading was performed at a sample temperature of 200 °C, which temperature is in the range of actively-cooling environment in divertor. In addition to undamaged samples, the damaging was performed by W self-implantation with 20MeV W⁶⁺ ions in the TOF beamline of the 3 MV tandem

accelerator. W ions were created with a cesium sputter source from a W carbide target [5]. The damaging was performed up to 0.23 dpa (displacement per atoms), which corresponds to the level that D can be saturated in W. The schematic experimental strategy is shown in Figure 26.

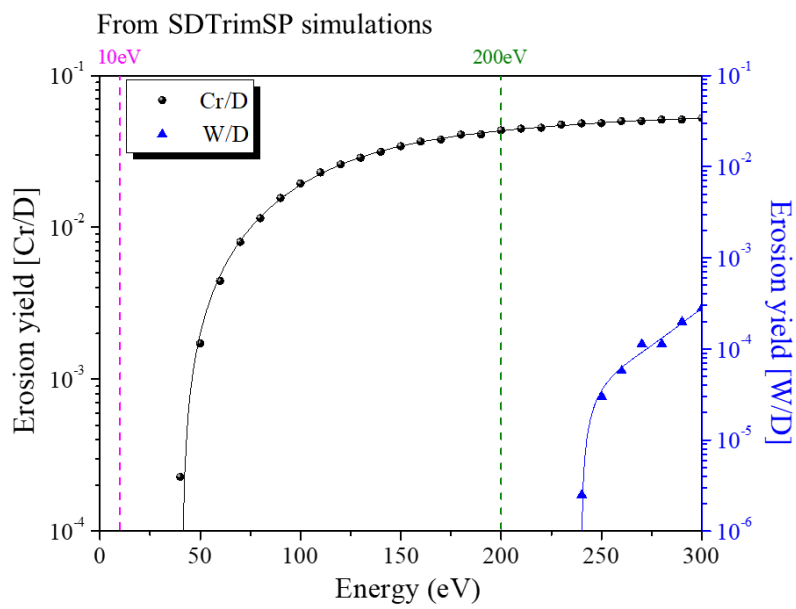


Figure 25 Sputtering yields of W and Cr for D calculated by the SDTrimSP simulations

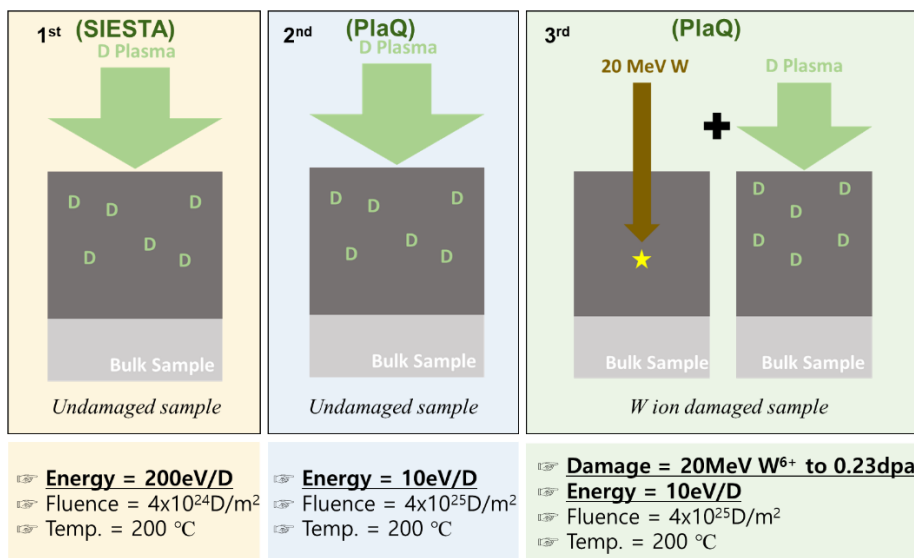


Figure 26 Experimental strategy for deuterium exposures.

4.2.2 Characterization

4.2.2.1 Mechanical test (3-point bending test)

Based on these tests the flexural strength and strain can be calculated as

$$\text{Flexural Stress } (\sigma) = \frac{3PL}{2bd^2} \quad (1)$$

$$\text{Flexural Strain } (\varepsilon) = \frac{6Dd}{L^2} \quad (2)$$

in which D is the maximum deflection of the 3PB specimen; d is the thickness of the specimen, L is the supporting span of the test stage (10mm), P is the load, and b is the width of the sample.

For the microstructural observation, one of side areas is finely polished and bending tested, and then observed crack propagation and fracture surfaces with SEM.

4.2.2.2 Deuterium retention behavior

The D concentration in the near surface of all samples is probed with a ^3He ion beam at the 3 MV tandem accelerator available at Max Planck Institute for Plasma Physics (IPP) Garching [5]. To quantify the D concentration of surface for all samples, the nuclear reaction analysis (NRA) using the $\text{D}(^3\text{He}, \text{p})\alpha$ reaction and detecting the high energy protons is performed. The energies of the ^3He beam were chosen to 690, 800, 1200, 2400, 3200, 3800, and 4500 KeV. Depending on the different energy, it can provide a maximum depth of D concentration of approximately 7.5 μm . The measured spot was square shape with roughly 2×2 mm in the center of each sample and the resulting proton spectra for each energy are recorded by two proton detectors at a scattering angle of 135° and analyzed using the reaction cross section, as shown in [6]. Finally, the depth profiles are constructed and D quantity in the surface are estimated by employing the NRADC [7] in combination with the SIMNRA software [8]. Following NRA analysis and microstructural characterization, the thermal desorption spectroscopy (TDS) measurement of all samples was conducted to quantify total D concentration for all samples with the use of the TESS device described in [9] For TDS measurement, the samples are placed inside a quartz glass tube under a high vacuum atmosphere ($\sim 10^{-6}$ Pa) and heated in an external tubular oven with a linear ramp rate of $3^\circ\text{C}/\text{min}$ to a maximum temperature of 727°C without soaking time. Total D retained in samples are expected to be released and desorbed gaseous species are detected by a quadrupole mass spectrometer (Balzers DMM422). To gain the D desorption flux, the individual D fluxes from the signals of the molecules HD, D_2 , HDO, and D_2O , which are the main contributors to the total D count, are estimated. Under the assumption that the mass spectrometer sensitivity relation from H_2 and H_2O is similar to D_2 and D_2O as well as HD and HDO, the sensitivity factors are taken from literature [10]

Using scanning electron microscopy (SEM) imaging, the microstructure with interest region for all samples in 200 eV/D was characterized to observe the modifications. For 10 eV/D, the microstructures were observed only after D loading. Since it is difficult to distinguish the microstructural differences in the resolution of

SEM scale for the W self-ion damaging and D loading, the microstructure was only observed for the undamaged samples. The microscope (Helios NanoLab600, FEI) allows secondary electron (SE) and backscattered electron (BSE) imaging and is equipped with a Ga^+ focused ion beam (FIB). In addition, the surface morphology was examined using a confocal laser scanning microscope (CLSM). The used CLSM (LEXT OLS4000, Olympus) also allows differential interference contrast microscopy (DIC). All microstructures were observed before TDS measurements, where the samples could be destroyed by heat.

4.3. Results and discussion

4.3.1 Mechanical test (3-point bending test)

The flexural strength and strain obtained in the bending test are shown in Figure 27. Figure 27 (a) gives the information tested at RT, and all samples show pure linear elastic deformation behavior with no plastic deformation until failure. These behaviors would be attributed by the brittle fractures since their DBTT is generally known for the higher temperatures [11]. Pure W exhibits very low stress with strain, which the DBTT is very far from the tested temperatures. In this temperature regions, the intergranular fracture stress of W is too low to have failure without reaching its intrinsic properties. The microstructures for crack propagation and fracture surfaces support this logic. Figure 28 (a, b) show the crack propagation of W, which has only intergranular fracture along grain boundaries. Also, a clear brittle intergranular fracture surface is observed, as shown in Figure 28 (c, d). In fracture surface of W, the nano to micron-sized pores are observed (dashed green lines), which again confirm the difficulties in densification of W without thermo-mechanical treatment [12]. These pores more easily enable to dominantly propagate crack along the boundaries in addition to the weak intergranular fracture stress. Note that the average density of pure W was 99.1%. For these reasons, as-sintered W is observed to be failed in a very brittle manner with low strength and strain. Pure Cr shows more strength and elongation than W at room temperature because its DBTT is lower than that of W. Therefore, the moderate strength with elongation were observed in the testing at RT. For Cr-10W and Cr-20W, both mechanical strength and elongation are even increased compared to the pure Cr. With high W content, the high strength can be obtained, without losing its elongation. It should be noted that the W fraction and the grain size of W are the two key parameters in determining the strength of Cr-W dual-phase composites. However, the low elongation compared to Cr-10W and Cr-20W cannot easily be understood by relation between strength and elongation, i.e., elongation is inversely proportional to hardness, strength, and modulus. The propagation of cracks in pure Cr is shown in the brittle manner (Figure 29 (a, b)), without any deflection. In Figure 29 (c, d), the fracture surface corresponds to the

pure cleavage and some micron-sized pores are also observed in fracture surfaces. The average density of Cr was measured as 99.1% in the chapter 3. Therefore, the probable reason for the low elongation is that the micron-sized pores in the initial microstructure (Figure 18 (a)). The Cr-10W and Cr-20W also show the propagation of cracks in the brittle manner, which is attributed by the DBTT temperatures, without any deflection, as shown in Figures 30 and 31 (a, b). Similarly as pure Cr and W, the fracture surfaces show the pure cleavage in Cr region and the intergranular fracture in W region, as shown in Figures 30 and 31 (c, d). Nevertheless, due to the benefit to highly densify the Cr-W composites, they show better mechanical properties than pure systems.

The mechanical testing at 300 °C rather show a different behavior from RT, as shown in Figure 27 (b). Pure W is nearly the same properties with the results that is tested at RT, implying that the testing temperature is still below the DBTT. However, pure Cr start to show plastic deformation, which this region might be in the range of above DBTT. As explained in the results at RT, the ductility reduction for the pure Cr would be attributed by the micron-sized pores which cannot be fully closed during sintering cycle. Unlike the pure systems, the mechanical properties of Cr-10W and Cr-20W were enhanced for both strength and elongation. These two samples are well-densified during SPS, therefore, the trends of strength and elongation were clearly shown at the 300 °C, which strength is dependent on the W content in Cr-W composites, while elongation is not. Nevertheless, it has shown potential abilities for withstanding both crack opening and propagation, since the flexural stress increases dramatically compared to pure Cr and moderate flexural strain is observed. We believe that if the testing temperature is well above the DBTT range, it will have more potential to have good elongation even in the higher temperature. Figures 32 and 33 (a, b) support these results, as Cr is now deflecting the crack propagation by making themselves deformed. The crack surface after this test is shown in Figure 32 and 33 (c, d). The fracture surfaces clearly show the differences from the results tested at RT. Here, the most of fractures are cleavage but river pattern is observed in Cr-10W. Furthermore, fracture surface shown in Cr-20W show the micro-cleavage rather than pure cleavage, implying that the testing temperature was in the range of DBTT. Even with this temperature, Cr-W composites show potentially applicable to PFM application in relatively low temperature compared to pure W. In addition,

depending on the desired properties in terms of stress and strain combination, the selection of Cr to W ratio is possible. Figure 34 shows the schematic diagram for the Cr-W dual-phase composites, indicating that strength and elongation can be achieved simultaneously and controllable according to the properties we desired.

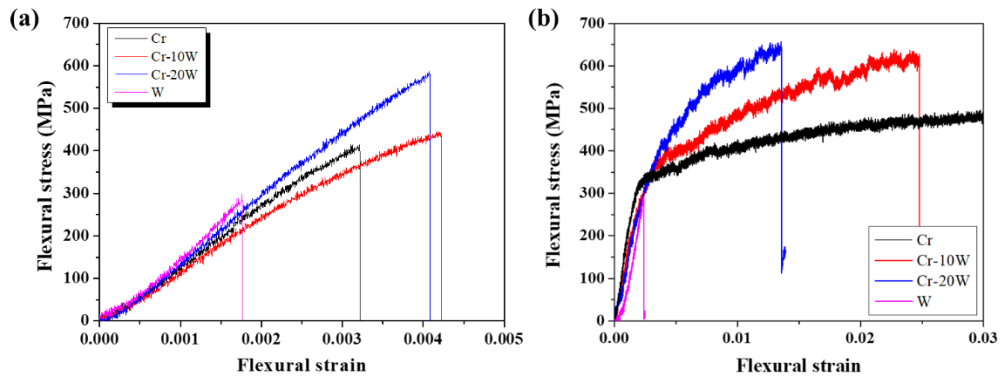


Figure 27 Flexural stress-strain curves obtained from 3PB test at (a) RT and (b) 300 °C. For each condition, at least more than three samples were tested.

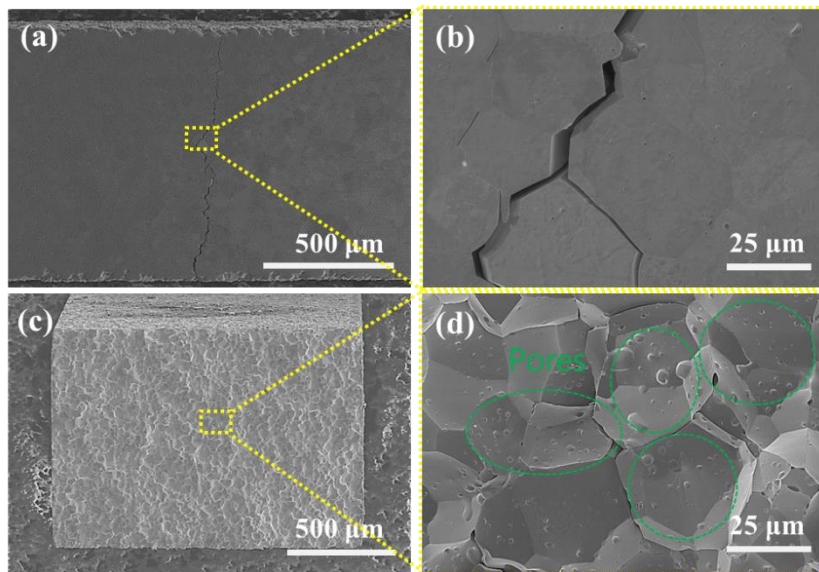


Figure 28 SEM images of crack propagation for (a, b) and of fracture surfaces for (c, d). All samples are pure Cr and tested at RT. Green dotted lines indicate nano to micron-sized pores.

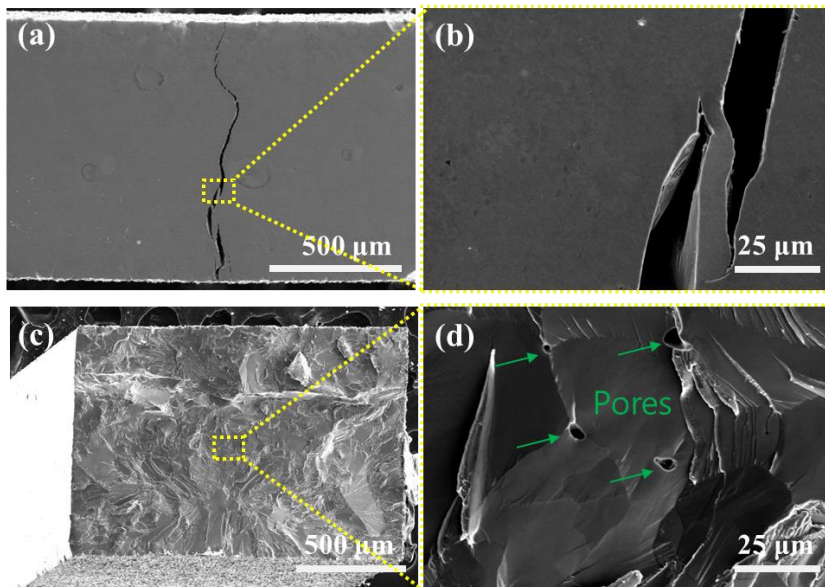


Figure 29 SEM images of crack propagation for (a, b) and of fracture surfaces for (c, d). All samples are pure W and tested at RT. Green arrows indicate micron-sized pores.

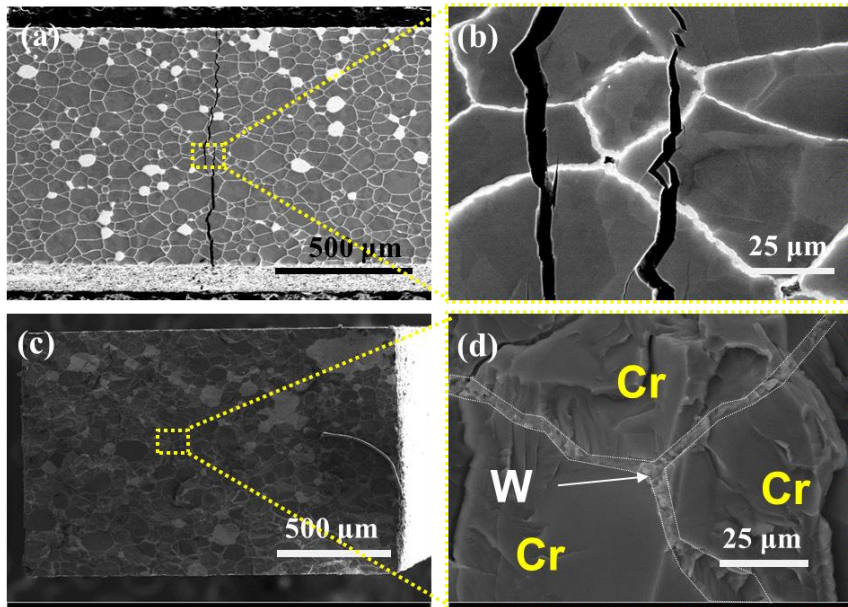


Figure 30 SEM images of crack propagation for (a, b) and of fracture surfaces for (c, d). All samples are Cr-10W and tested at RT.

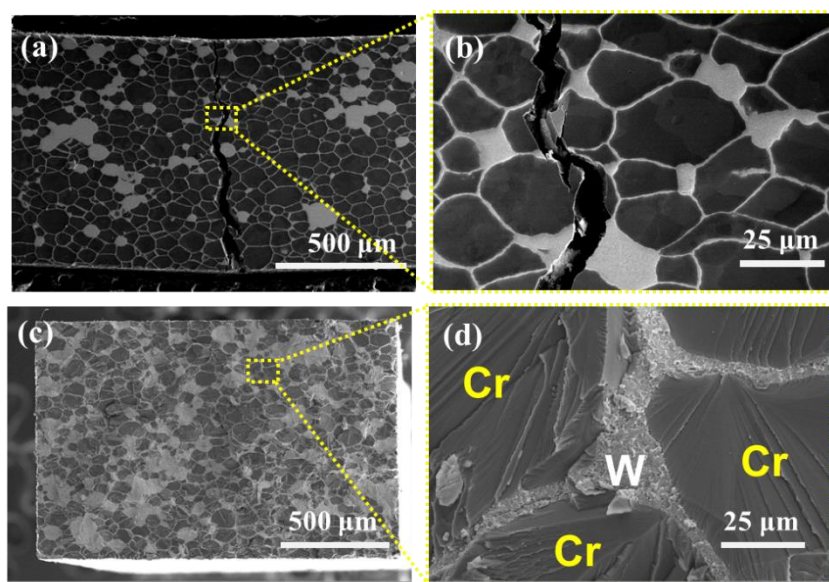


Figure 31 SEM images of crack propagation for (a, b) and of fracture surfaces for (c, d). All samples are Cr-20W and tested at RT.

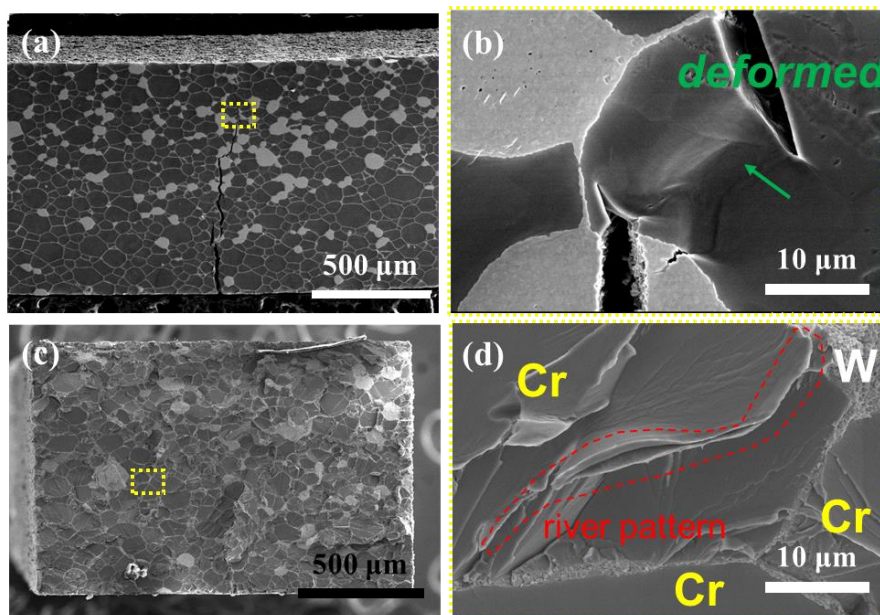


Figure 32 SEM images of crack propagation for (a, b) and of fracture surfaces for (c, d). All samples are Cr-10W and tested at 300 °C. Green arrow indicates the deformed region in Cr and Red dotted line indicates river pattern.

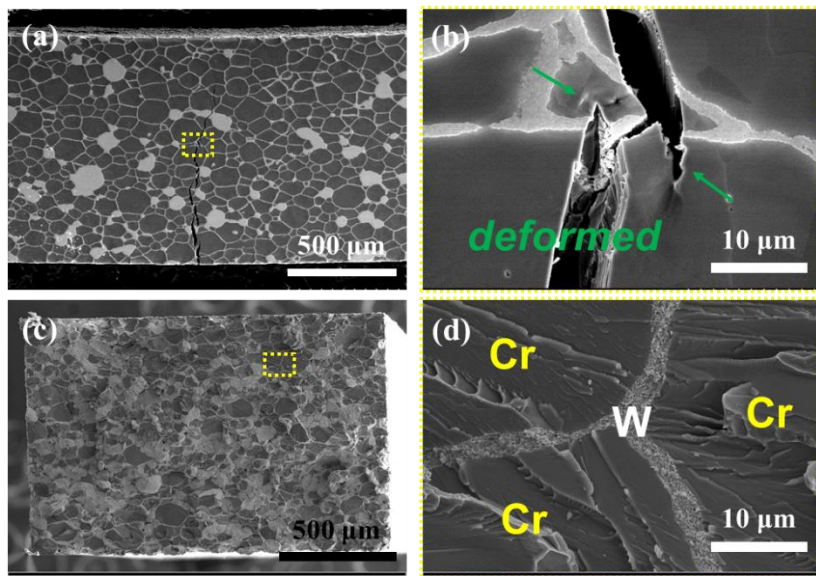


Figure 33 SEM images of crack propagation for (a, b) and of fracture surfaces for (c, d). All samples are Cr-20W and tested at 300 °C. Green arrows indicate the deformed region in Cr.

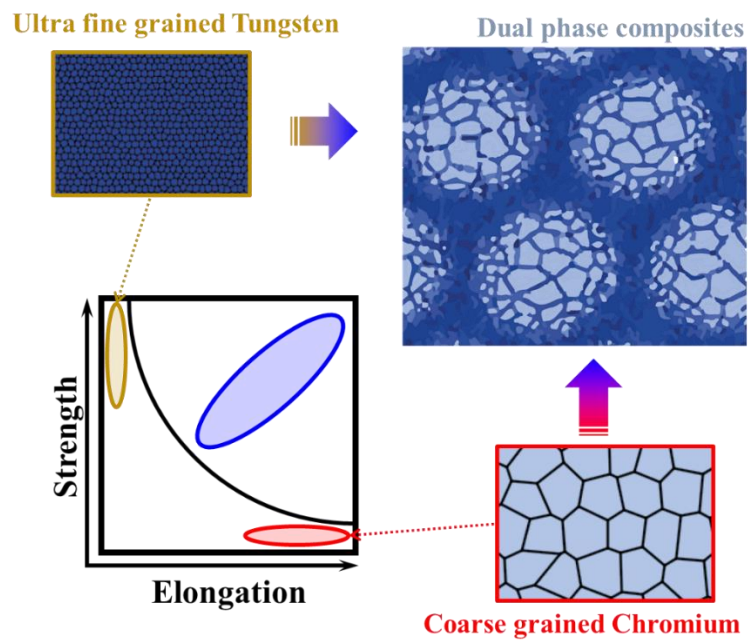


Figure 34 Strategy for the microstructures and corresponding mechanical properties

4.3.2 Deuterium retention behaviors

Microscopy

Figure 35 shows the microstructural changes before and after D plasma exposures with SEM and CLSM images (all CLSM images are displayed bottom left inset). In the case of exposure energy with 200 eV, the microstructures were all observed same region for all samples before and directly after D plasma exposures. The microstructure of the W sample shows no severely changing and some blisters are observed in the microstructures (orange circles), as shown in Figure 35 (a, b). Here, the formation of gas-filled cavities near the surface (so-called “blisters”). It is also observed from CLSM images that the changes in height are not dramatic. However, the microstructure of the Cr and Cr-20W samples are significantly changed for both SEM and CLSM images. These differences of the surface changes are contributed by the exposed energy that is far exceeding D threshold of Cr and not exceeding the D threshold of W. Therefore, the most of Cr atoms could physically be sputtered out by the intense D ions, as shown in Figure 35 (d, e, g, h). The surface of pure Cr that has been changed in the characteristic grain with grain boundary seems to be etched out. As explained, this is attributed by the physical erosion of Cr atoms exposed by the intense D ions. Therefore, the surface of grains is more observed in a way of flat and the surface of grain boundaries is more concretely shown in both SEM and CLSM images (Figure 35 (d, e)). Similarly, the Cr-20W shows the microstructural changes in Cr region, but the different microscopic aspects are shown in each W and Cr region. The Cr is physically eroded by the D ions, which the morphologies of surface are changed to flatter and deeper along the grain boundaries in SEM images (Figure 35 (g, h)). This change is also observed in CLSM images displayed in a small inset, showing the most of areas become blue areas with a lower height in Cr particles. However, the W appears as a green level rather than a blue level, meaning no severe physical erosion has occurred. In addition, a uniform and periodic white ash-like structures are observed on the Cr particles near the Cr/W interfaces. This white ash-like microstructural changes can be seen including some grain boundaries. In order to observe the white ash-like microstructural changes more in detail, high resolution SEM-EDS analysis, together with cross sectional

analysis by SEM-FIB were performed as presented in Figure 36 (a–e). The white ash-like structures are located on the Cr particles near the Cr/W interfaces, where these structures seem to be initiated from W to Cr, including grain boundaries. The white ash-like structures correspond to the W elements, as shown in EDS mapping images. However, it is not observed in the cross-sectional microstructure, as shown in Figure 36 (b, c), implying that the formation of white ash-like structures has only occurred after plasma exposures. With that, we can conclude that the formation of white ash-like structures is due to the physical erosion of Cr atoms. Since the Cr and W have very different D threshold at 200 eV, it is rather reasonable to be seen such a structure after D exposures. The existence of W atoms in Cr particle is probably due to the inter-diffusion during the fabrication via SPS. The elemental distribution of W in Cr is already observed in the previous chapter that W diffused into the Cr, gradually (Figure 20). We therefore believe the diffused W atoms during the production would be the one of the main reasons to make this white ash-like structures.

On the other hand, the energy with 10 eV didn't show any specific microstructural changes for all system, as shown in Figure 35 (c, f, i). In addition, it is observed that no blistering and no specific physical erosion were observed by SEM and CLSM, which is due to the exposed energy being far below the sputtering threshold.

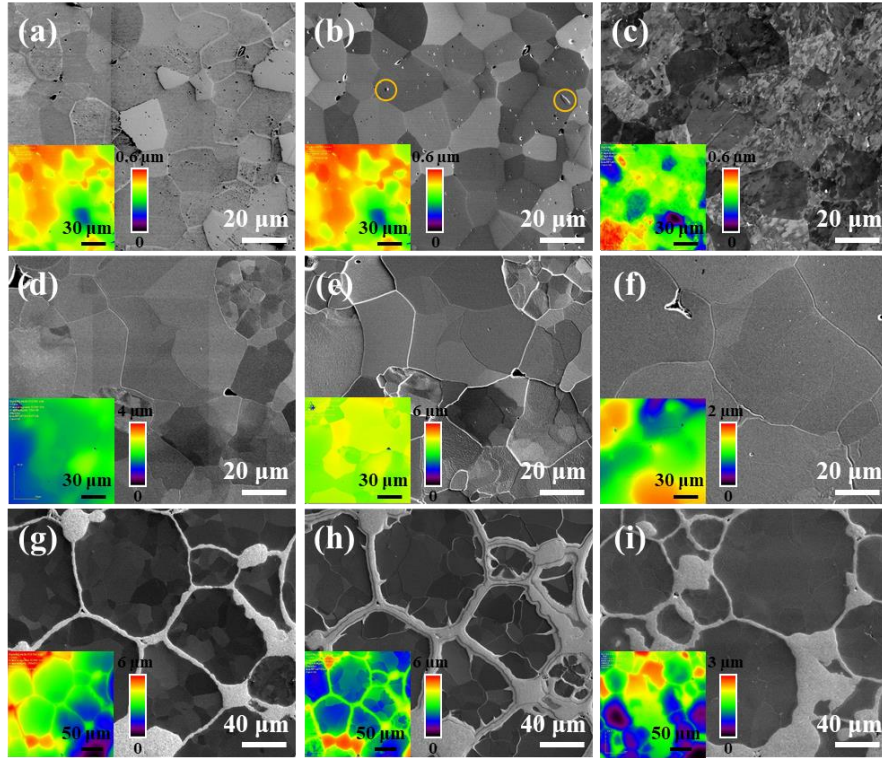


Figure 35 SEM images for before and after D exposures. (a, d, g) initial microstructures of W, Cr, and Cr-20W. (b, e, h) after D exposures with 200 eV/D energy. (c, f, i) after D exposures with 10 eV/D energy. All bottom left images displaced in the inset is CLSM images.

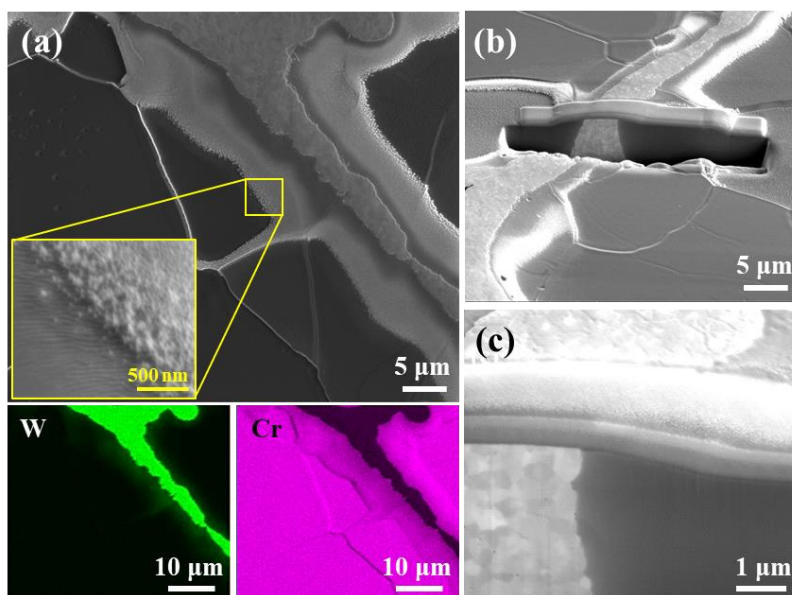


Figure 36 SEM images (a) and EDS elemental mapping (bottom of (a)) of the Cr-20W interface after D exposures. Yellow inset indicates enlarged area of white ash-like area. Cross-sectional SEM images are shown in (b, c)

D retention from NRA and TDS analysis

The D concentration depth profiles from NRA measurements and the D desorption spectra from TDS of selected condition is shown in Figure 37. In general, there should have large differences in concentration profile and TDS spectra between the different samples themselves, depending on the composition, grain size, defect densities, and diffusivities. The D concentration profile of the undamaged W (black) is located top-most region containing a high D concentration. At the surface and in larger depths, the concentration levels are relatively low while the D concentration is the highest at the depth of 1 to 3 μm (Figure 37 (a, b)). This trend is also similarly observed in damaged W, as shown in Figure 37 (c), implying that the as-sintered W has already many defects as D trapping sites. This is attributed by the low density and pores in fracture surfaces in previous Chapter. The damaged level calculated by SRIM for W and Cr is 2.3 and 3.2 μm , respectively. The differences of damage level are simply due to the atomic weight differences between W and Cr. The undamaged Cr samples (red) in Figure 37 (a, b) generally have higher D concentrations at the near-surface area than inside area. However, the D concentration level at the surfaces is very small that trapping of D is not severely observed. Unlike the W, the D concentration is almost more than a hundred times increased when D is exposed into damaged Cr (Figure 37 (c)), implying that the as-sintered Cr initially didn't have many defects as D trapping sites. This could be attributed by the use of well-densified as-received Cr powder, or the annealing effect during the outgassing process (annealed at 923 $^{\circ}\text{C}$ for 2 h). Nevertheless, D concentration in near surface of Cr is still minimum for all damaged samples (Figure 37 (c)). Cr-20W shows rather different trends that the most of D near-surface is in the similar ranges for both undamaged and damaged system.

Figure 37 (d–f) shows the TDS spectra that represents total released amount of D. TDS spectra indicate total D retained in the whole samples, unlike the NRA data indicates near-surface D content. For pure W, all corresponding the desorption spectra show higher desorption fluxes than Cr and Cr-20W for every condition, just like NRA results. Again, in Cr samples, the trend of retained D is similar with NRA analysis, showing small deuterium retention for undamaged samples and significant increment of D retention for damaged samples. Interestingly, Cr-20W shows no

severe changes for all conditions where a similar amount of D is maintained both for undamaged and damaged samples.

From the NRA and TDS results we obtained, we finally can calculate D areal density by integrating under the areas, which is the number of D divided by the exposed area. The results are summarized in Figure 38. The surface here indicates the areal density of D for the depth of $\sim 8 \mu\text{m}$. Whereas, the bulk indicates the area density of D for the depth larger than $8 \mu\text{m}$. It can simply be calculated by subtracting the surface areal density from the total areal density. At 200 eV with undamaged samples, the amount of D retained in Cr is very small. In addition, the deuterium inventory for surface is nearly not showing, the suspicion was made that physical erosion observed by microstructures could have a strong effect. In any case, the very small D uptake at the low ion energy at 10 eV with undamaged Cr sample shows a single trend, so that the microstructural changes caused by physical erosion can only have a negligible effect on the D retention in Cr. The D in undamaged Cr samples is mainly retained in the bulk of the specimen ($>8 \mu\text{m}$), not in the surface. For undamaged W at the 200 and 10 eV energies, the significant amount of D is retained, especially, the large amount of D inventory is contained in the surface of specimen rather than the bulk. This could be attributed by the defect density that has initially exist in the surface. This actually slowing down the diffusion of D in the bulk. For undamaged Cr-20W at the 200 and 10 eV energies, the opposite trends of D inventory are observed. At 200 eV, the large amount of D is contained in the bulk of specimen, whereas at 10 eV, it is contained more in the surface of the specimen. Here, we can point out two points. First, although pure Cr didn't have a strong effect on the physical erosion, the physical sputtering affects the D inventory in the surface of specimen. Second, the diffusion of D starts deeper at higher energy so that the diffused amount of D become more dominant for total D inventory. Rather surprisingly, for the damaged samples with 10 eV energy, three distinct features are visible: First, Cr has shown retained D in the surface, which make an unexpected enhanced D retention at the bulk of the specimen. Second, once the damage layer is generated by the W self-ion, an unexpected enhanced D retention at the bulk of the W ($>8 \mu\text{m}$) in addition to the surface is also revealed. Third, although Cr-20W increased D retention on the surface, it did not show an increase in D inventory in the bulk as much as the pure system, and the total D becomes the smallest of all

damaged samples. The enhanced D retention at the bulk of pure system is probably due to the introduction of a large number of defects, especially for the high fluence case, as described in [13–23].

Diffusion of hydrogen in metals is a complex problem that is still in the focus of numerous research groups, and cannot be explained by the solubility alone. Here, one fact is that the solubility of hydrogen in Cr is higher than that of W but diffusion of hydrogen in Cr is surprisingly fast more than 5 times than W, as described in Table 4. Although Cr has a large solubility than W, the unexpectedly fast diffusivity of D makes the Cr with low D inventory of surface as well as total for the undamaged samples. However, once the Cr is pre-damaged by W self-ion, the enhanced inward diffusion is observed in addition to the surface D retention. This probably attributed by the introduction of a large number of defects on the surface. The damaging Cr with W self-ion would be rather severe because the atomic radius for W is much larger than Cr, so that the damaging level by the W self-ion would easily achieve the highly saturated defect density. Due to this defect generation, Cr uptake D in the bulk. This is also observed in pure W system. The moderate defect at the surface retained D as much as possible, as shown in undamaged results. However, once the defects are highly saturated by the W self-ion damage, the unexpectedly enhanced D diffusion can be observed in the bulk. Even though the solubility is smaller, the presence of high D inventory in pure W is ascribed to the initial density and defect which cannot achieved desired properties without thermomechanical processing. The Cr-20W composites, which consists of 2 materials, should have competition for the D diffusion based on their thermodynamic, diffusivity, and solubility. From the view of heat of solution, thermodynamically, Cr is more stable than W to have D. However, as explained, the diffusivity is approximately 5 times faster in Cr than in W. The solubility of D in W is a half of the Cr. Therefore, when D enters the Cr-W dual-phase composites, the D diffusion from the Cr to W at the interface is strongly suppressed, which could be attributed to the higher thermodynamic stability of H with Cr than W. This will be suppressed until the entire Cr is filled as much D as possible. Conversely, the D diffusion from the W to Cr at the interface is relatively easy because of thermodynamic stability of D with Cr is higher than W. However, the delivery of D in W to Cr would relatively slow because diffusivity of D is 5 times slower. Therefore, the combination of tendency for Cr to retained D as much as

possible and the slow diffusion of D in the W minimize the bulk diffusion. This concept can be applied to the damaged samples, so that a relatively low D inventory can be obtained although the samples are pre-damaged. Therefore, the total D retained in damaged Cr-20W would be minimized. This suggests the irradiation damage of as-sintered pure system would contribute to the deterioration of the fuel cycle, and this effect will become more severe by extending operation duration. In contrast, the suppression of enhanced inward D diffusion after pre-damaged of Cr-20W would be beneficial to longer operation duration. Other than the material properties, the effect of the type of the defect on a given system could be main reasons, which is a direction for future research.

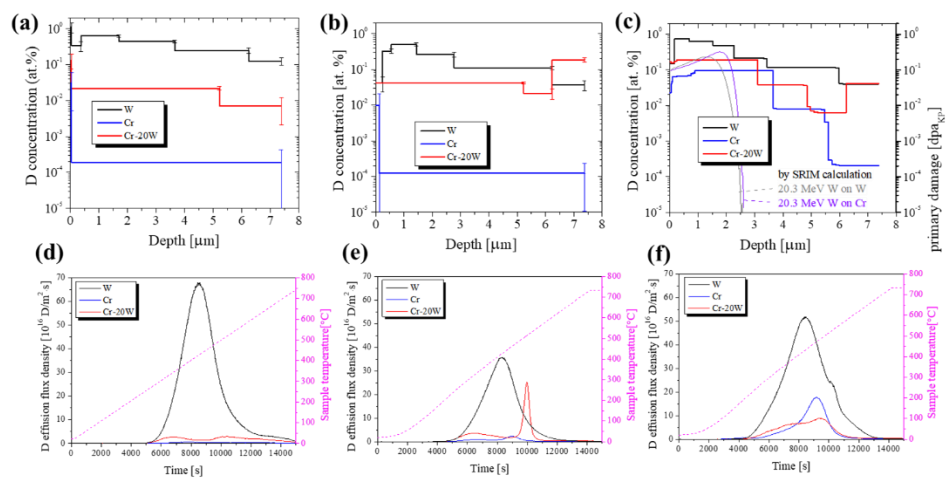


Figure 37 D concentration depth profiles for undamaged samples of (a) 200 eV/D and (b) 10 eV/D for damaged samples of (c) 10 eV/D. TDS Spectra of D desorption flux from D₂ and HD signals for undamaged samples of (d) 200 eV/D and (e) 10 eV/D for damaged samples of (f) 10 eV/D.

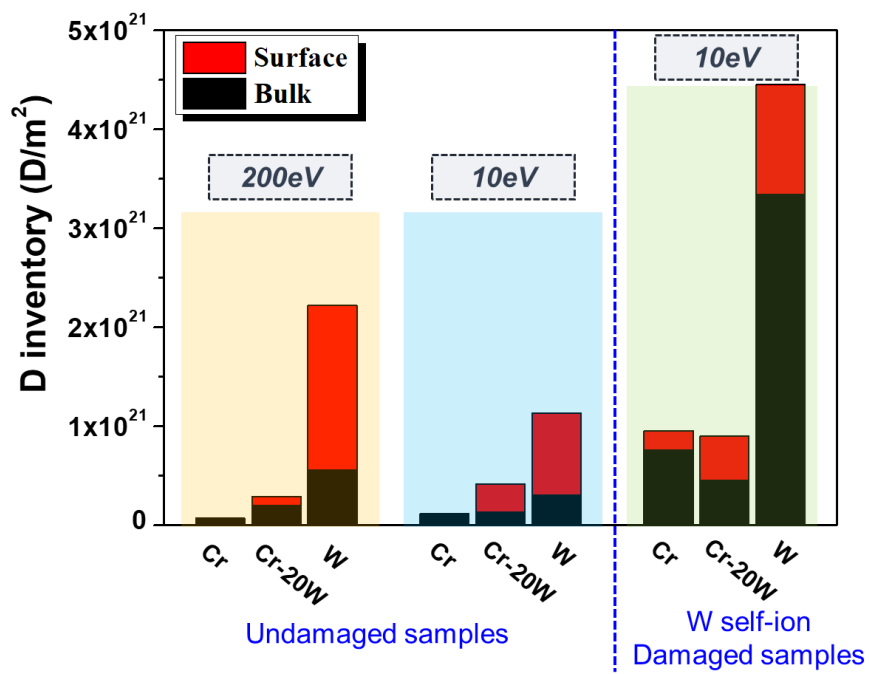


Figure 38 D retention measured by NRA and TDS. The surface of D inventory was obtained by the NRA analysis, while the bulk of D inventory was obtained by subtracting the surface of D inventory from the total D inventory measured by TDS

Table 4 The activation energies for heat of solution, diffusion, and solubility of hydrogen in W and Cr.

	Heat of solution (eV) [24]	Activation energy for diffusion (eV) [25]	Activation energy for solubility (eV) [26]
W	1.1	0.393	1.049
Cr	0.6	0.077	0.591

4.4 Conclusions

In this contribution, we have assessed the potential abilities of Cr-W dual-phase composites, together with pure Cr and W. The materials are all fabricated by the SPS, as described in previous Chapter 3. In the 3-point bending test, the Cr-W dual-phase composites behave in a brittle manner at room temperature, while high strength with moderate elongation were observed at 300 °C. The scanning electron microscopy was utilized to characterize the crack propagation and the fracture surface of the materials tested at RT and 300 °C. As a result, below the DBTT (RT), Cr did not deflect crack propagation, and pure cleavage fractures are observed. Whereas near the DBTT (300 °C), Cr deflects the crack propagation by making plastic deformation, and the micro-cleavage fractures and river patterns are observed, which is why Cr-W composite can possess high strength with moderate elongation.

In the deuterium retention, deuterium retention for the undamaged and heavy ion pre-damaged samples at low- and high energies has been studied with a high fluence of 4×10^{24} and 4×10^{25} D/m², respectively. Undamaged Cr samples have a small amount of D inventory in the bulk, which is attributed by the high diffusivity of D. In addition, undamaged W samples have a large amount of D inventory in the surface, implying that the initial defect density was already high. Undamaged Cr-20W show the different D inventory at the different energy. At 200 eV, the D inventory in the bulk is higher than in the surface, which is caused by the physical sputtering of Cr or D energy depth. However, the opposite trend was observed at 100 eV, which the combination of tendency for Cr to retain D as much as possible and the slow diffusion of D in the W minimize the bulk diffusion. Due to the highly saturated defect density, the damaged Cr and W enhance the D inward diffusion, which corresponds to the large amount of D inventory in the bulk. However, the damaged Cr-20W did not enhance the D inward diffusion due to the high thermodynamic stability with Cr with kinetic delay in the W phase.

4.5 References

- [1] A. Manhard, T. Schwarz-Selinger, W. Jacob, Quantification of the deuterium ion fluxes from a plasma source, *Plasma Sources Sci. Technol.* 20(1) (2011) 015010.
- [2] R. Arredondo, M. Oberkofler, K. Schmid, T. Schwarz-Selinger, W. Jacob, R. Neu, SIESTA: a high current ion source for erosion and retention studies, *Rev. Sci. Instrum.* 89(10) (2018) 103501.
- [3] A. Mutzke, R. Schneider, W. Eckstein, R. Dohmen, K. Schmid, U.V. Toussaint, G. Badelow, SDTrimSP Version 6.00, Max Planck Institute for Plasma Physics, Garching, Germany, 2019
- [4] A. Manhard, Deuterium inventory in tungsten after plasma exposure: a microstructural survey, Ph. D thesis, Augsburg University, 2012
- [5] T. Schwarz-Selinger, Deuterium retention in MeV self-implanted tungsten: Influence of damaging dose rate, *Nucl. Mater. Energy* 12 (2017) 683–688
- [6] B. Wielunska, M. Mayer, T. Schwarz-Selinger, U.V. Toussaint, J. Bauer, Cross section data for the D (^3He , p) ^4He nuclear reaction from 0.25 to 6 MeV, *Nucl. Instrum. Methods Phys. Res. B: Beam Interactions with Materials and Atoms* 371 (2016) 41–45.
- [7] K. Schmid, U.V. Toussaint, Statistically sound evaluation of trace element depth profiles by ion beam analysis, *Nucl. Instrum. Methods Phys. Res. B: Beam Interactions with Materials and Atoms* 281 (2012) 64–71.
- [8] M. Mayer, SIMNRA, a simulation program for the analysis of NRA, RBS and ERDA, *AIP Conf. Proc.* 475(1) (1999) 541–544.
- [9] E. Salançon, T. Dürbeck, T. Schwarz-Selinger, F. Genoese, W. Jacob, Redeposition of amorphous hydrogenated carbon films during thermal decomposition, *J. Nucl. Mater.* (2) (2008) 160–168.
- [10] H. Analytical LTD, Relative sensitivity, RS measurements of gases, Application Note 282, 2018
- [11] Y. Oh, N. Kwak, K. Lee, W.-S. Ko, H.N. Han, Ductility enhancement of tungsten after plastic deformation, *J. Alloys Compd.* 787 (2019) 801–814.

- [12] G. Pintsuk, A. Hasegawa, in: R.J.M. Konings, R.E. Stoller (Eds.), Tungsten as a plasma-facing material, *Comprehensive Nuclear Materials*, 6, Elsevier, San Diego, US, 2020, pp. 19–53
- [13] S. Wang, X. Zhu, L. Cheng, W. Guo, M. Liu, C. Xu, Y. Yuan, E. Fu, X.-Z. Cao, G.-H. Lu, Effect of heavy ion pre-irradiation on blistering and deuterium retention in tungsten exposed to high-fluence deuterium plasma, *J. Nucl. Mater.* 508 (2018) 395–402.
- [14] S. Wang, W. Guo, L. Cheng, T. Schwarz-Selinger, M. Liu, X. Zhu, Y. Yuan, E. Fu, G.-H. Lu, Dependence of blistering and deuterium retention on damage depth in damaged tungsten exposed to deuterium plasma, *Nucl. Fusion* 61(5) (2021) 056003.
- [15] X.-L. Zhu, Y. Zhang, L. Cheng, L.-Q. Shi, G.D. Temmerman, Y. Yuan, H.-P. Liu, G.-H. Lu, Suppression of deuterium-induced blistering in pre-damaged tungsten exposed to short-duration deuterium plasma, *J. Nucl. Mater.* 500 (2018) 295–300.
- [16] X.-L. Zhu, Y. Zhang, L. Cheng, Y. Yuan, G.D. Temmerman, B.-Y. Wang, X.-Z. Cao, G.-H. Lu, Deuterium occupation of vacancy-type defects in argon-damaged tungsten exposed to high flux and low energy deuterium plasma, *Nucl. Fusion* 56(3) (2016) 036010.
- [18] T. Schwarz-Selinger, J. Bauer, S. Elgeti, S. Markelj, Influence of the presence of deuterium on displacement damage in tungsten, *Nucl. Mater. Energy* 17 (2018) 228–234.
- [19] M.H.J. 't Hoen, B. Tyburska-Püschel, K. Ertl, M. Mayer, J. Rapp, A.W. Kleyn, P.A. Zeijlmans van Emmichoven, Saturation of deuterium retention in self-damaged tungsten exposed to high-flux plasmas, *Nucl. Fusion* 52(2) (2012) 023008.
- [20] S. Markelj, T. Schwarz-Selinger, M. Pečovnik, A. Založnik, M. Kelemen, I. Čadež, J. Bauer, P. Pelicon, W. Chromiński, L. Ciupinski, Displacement damage stabilization by hydrogen presence under simultaneous W ion damage and D ion exposure, *Nucl. Fusion* 59(8) (2019) 086050.
- [21] B. Wielunska, M. Mayer, T. Schwarz-Selinger, A.E. Sand, W. Jacob, Deuterium retention in tungsten irradiated by different ions, *Nucl. Fusion* 60(9) (2020) 096002.
- [22] J.L. Barton, Y.Q. Wang, R.P. Doerner, G.R. Tynan, Model development of plasma implanted hydrogenic diffusion and trapping in ion beam damaged tungsten, *Nucl. Fusion* 56(10) (2016) 106030.

- [23] X.-L. Zhu, Y. Zhang, A. Kreter, L.-Q. Shi, Y. Yuan, L. Cheng, C. Linsmeier, G.-H. Lu, Aggravated blistering and increased deuterium retention in iron-damaged tungsten after exposure to deuterium plasma with various surface temperatures, *Nucl. Fusion* 58(10) (2018) 106005.
- [24] E. Fromm and G. Hörz, Hydrogen, nitrogen, oxygen, and carbon in metals, *Int. Met. Rev.* 25(1) (1980) 269–311.
- [25] R. Frauenfelder, Solution and Diffuion of Hydrogen in Tungsten, *J. Vac. Sci. Technol.* 6 (1968) 388.
- [26] D. Stöver, H.P. Buchkremer, R. Hecker, Hydrogen and deuterium permeation through metallic and surface-oxidized chromium, *Surf. Coat. Technol.* 28 (1986) 281–290.

.

Chapter 5. Conclusions and Outlook

A new Cr-W dual-phase composite produced by powder metallurgy was developed. The control of the powder size, milling time, and sintering time of a sintered compact are permitted to optimize the sintering condition. The fast sintering kinetics was attributed by the Cr diffusion in W, providing a fast diffusion path for Cr to W and vice versa. After fabrication, the significantly increased mechanical properties has also been realized. Deuterium retention behaviors were assessed to confirm the potential applicability as a plasma facing material. Spark plasma sintering (SPS) is the main production process used here. The problem caused by carbon diffusion during SPS is the first important issue that must be solved. Otherwise, the degradation of materials may be observed after the fabrication. Here, we start to discuss the fundamental solution related to the C issue from the Chapter 2. The significant conclusions elicited from this thesis are discussed below.

In Chapter 2, the several metallic foils as a C diffusion barrier were introduced in spark plasma sintered tungsten to minimize the C diffusion. We show that the Ta-foil protected system effectively suppress the C diffusion into the W, while Mo and W did not. The W foil is only a physical barrier that suppress the C diffusion by the dedication of itself. The Ta foil overcome this disadvantage by suppressing C diffusion both physically and thermodynamically. The effect of Ta foil is attributed to low diffusivity of C. Furthermore, the thermodynamically stable Ta carbide prevents further C diffusion at the Ta/W interface. For the opposite reason, C diffused faster not only in the Mo, but also at the Mo/W interface. Finally, the Ta foil can be applicable in the Cr system due to the same thermodynamic and kinetic relation with W.

In Chapter 3, Cr-W dual-phase composites are fabricated through a high-energy mill and SPS and the sintering at low temperature and the rapid rate of densification is confirmed. The role of the Cr diffusion in W during consolidation is analyzed. Furthermore, the optimization of process parameter for high densification without losing Cr properties is crucial to realize the desired properties. The process parameters such as optimal powder size, milling time, and sintering temperatures is controlled based on electron microscopy and X-ray diffraction. The newly developed

Cr-W dual-phase composites consist of a morphology with isolated coarse-grained Cr particles surrounded by a continuous network of ultra-fine grained W.

In Chapter 4, Cr-W dual-phase composites are characterized to observe their potential applicability as PFMs. The mechanical properties assessed by the 3-point bending test at RT and 300 °C (near DBTT). In the test at RT (below DBTT), they show a brittle behavior, with no suppression of the crack propagation. While, at 300 °C, Cr particles suppress the crack propagation and a ductile behavior is observed. In addition, Cr-20W would be beneficial to the suppression of enhanced inward D diffusion after pre-damaged owing to the high thermodynamic stability with Cr, and kinetic delay in the W phase.

For the future fusion reactor, when using W as the armor block, a critical concern is the high heat flux fatigue load. For normal W material, once the crack initiates, it can easily propagate through the whole armor block because of the intrinsic low toughness of tungsten. This stress distribution and crack initiation mechanism make the crack resistance and a higher toughness the most urgent criteria for plasma facing materials. In this study, according to the initial purpose of development, the Cr-W dual-phase composite produced by powder metallurgy processes can fulfill this requirement. In addition, to assess the potential applicability as a plasma facing material, the deuterium retention behaviors were studied using different combination of ion energies.

As the PMCs, after the bulk material production, the Cr-W dual-phase composite can be machined into the required geometry or joined with other materials depending on the physical requirements. Here, we suggested these PFCs can be used in the mid-heat flux region, avoiding direct heat flux. On the other hand, with some special tool systems, SPS can also produce near net shape materials with complex geometries. This gives us another potential option of Cr-20W dual-phase armor production. With the above results, this novel composite shows great application potential in a future fusion reactor.

국문 초록

텅스텐(W)은 뛰어난 고온경도와 내마모성 등의 우수한 특성 조합으로 인해 차세대 핵융합로의 플라즈마 대향 부품에 선호되고 있는 대표 후보물질 중 하나이다. 그러나 재료 고유의 높은 연성-취성 천이온도(DBTT)에 따른 강한 취성은 극한의 핵융합 환경에서의 적용을 크게 제한한다. 이와 같은 단점을 극복하기 위해 구조 설계 및 새로운 복합재료 및 합금개발에 대한 연구가 지속적으로 수행되어져 왔다. 이러한 연구 노력에도 불구하고 텅스텐의 고질적인 취성을 완전히 극복하는데 여전히 많은 연구가 필요한 실정이다. 최근에는 상대적으로 낮은 DBTT에 의해 저온영역에서도 상당한 연성거동을 보이며, 우수한 내식성 및 낮은 중성자 활성화 등의 장점을 가지는 크롬(Cr)이 핵융합 대면재로 적용되기 위한 연구가 주목받고 있다. 크롬의 여러 우수한 장점에도 불구하고 낮은 고온 강도는 실제 조업환경에서 활용되기에 한계점이 존재한다. 본 연구에서는 위 두가지 재료를 이용하여 새로운 개념의 크롬-텅스텐(Cr-W) 이상 복합재료(Dual-Phase composites)를 개발 및 제안하고자 하였으며, 두 소재간 상호 단점을 극복하여 물성 향상을 꾀하고자 하였다. 또한, 대향 부품으로의 응용가능성을 확인하기 위하여 기계적 특성 및 중수소 저항성이 평가되었다. 더불어, 공정 중에 발생하는 탄소(C) 확산으로 인해 재료 내부에서 자연적으로 생성되는 탄화물은 재료의 기계적 및 중수소 저항 특성 저하에 치명적이므로 함께 해결되어야 한다.

첫째, 소재제조시 발생하는 C 확산을 억제하였다. 일반적으로, 고융점의 W(3422 °C)과 Cr(1907 °C)이 치밀한 미세구조 및 원하는 특성을 얻기 위해서는 분말 야금법을 활용하여 제작한다. 본 연구에서는 난 소결체의 소결에 효과적인 분말 야금 기술인 통전 활성화 소결법(SPS)을 주요 생산 공정으로 활용하였다. SPS는 펄스 전류와 기계적 압력을 동시에 인가하여 높은 소결 밀도를 가진 벌크 샘플을 단시간에 얻을 수 있는 공정기술이다. 그러나 소결시에 사용하는 흑연 몰드로 인하여 소결체 내부에 C 원자가 침입하게 된다. 여기서, 주목할 만한 점은 W와 Cr이 강한 탄화물 형성 원소라는 것이다. 따라서, 소결 동안 W 및 Cr 내 탄소확산은 불가피하게 발생하게 된다. C 확산은 W와 Cr의 입계에서 탄화물 편석을 유도하며, 이는 연성 감소 및 취성에 의한 입계 파괴를 야기한다. 이러한 문제를 해결하기 위하여, W, 몰리브덴(Mo) 및 탄탈럼(Ta) 호일을 W 소결체의 C 확산방지 호일로 활용하고자 하였다. 특히, C 확산 장벽으로써 Ta 호일이 효과적임을 확인할 수 있었으며, 이는 C에 대한 높은 열역학적 안정도 및

Ta 탄화물의 탄소 확산 키네틱(Kinetics) 지연에 의해서 제어된다는 것이 밝혀졌다. Mo 호일은 Ta의 열역학적 및 키네틱 특성과 반대의 이유로 C 확산 장벽으로써 비효과적임을 분석할 수 있었으며, W 호일은 탄소 확산의 물리적인 지연에만 기여하여 그 효과가 부족함을 확인하였다. 최종적으로, 이와 같은 개념은 동일한 열역학과 키네틱 관계에 따라 Cr의 소결체 제조에도 적용 가능함을 확인할 수 있었으며, SPS를 이용한 Cr-W 이상 복합재료 제조시 Ta 호일을 활용하면 C 확산을 효과적으로 억제 가능함이 밝혀졌다.

둘째, Cr-W 이상 복합재료의 제조를 진행하였다. Cr-W 이상 복합재료 제조를 위해 고에너지 밀링법을 이용하여 두 분말을 혼합하고 소결을 진행하였다. 이렇게 개발된 복합재료는 조대한 Cr 입자가 3차원적이고 연속적으로 연결된 초미세립 W 네트워크로 둘러싸인 독특한 미세구조를 나타낸다. 본 소재의 소결 조건 확립을 위해 소결 온도, 시간, 공정, 분말 조건 등 소결 인자의 영향을 도출하였다. 이를 통해 Cr-10 vol.% W 및 Cr-20 vol.% W의 조성에서 1300 °C에서 소결시 완전 치밀화가 가능함을 확인하였다. 또한, W의 소결온도가 1700 °C 이상인 점을 감안하면, 비교적 저온에서 Cr-W 이상 복합재료의 W상의 소결성이 매우 향상된 것을 확인할 수 있었다. 이처럼 독특한 미세구조의 발현과 소결성 향상의 메커니즘을 고찰하기 위해, 전자 현미경 및 X-선 회절 분석 결과를 토대로 상태도 분석 및 키네틱 해석을 함께 병행하였으며, 이는 소결 동안 Cr의 W 내 확산에 의해 소결성 가속화에 기인하는 것을 확인하였다.

셋째, Cr-W 이상 복합재료의 특성이 평가되었다. 본 연구에서 개발된 Cr-W 이상 복합재료의 잠재적 응용가능성을 평가하기 위해서 기계적 특성 및 중수소 흡착 특성을 진행하였으며, 모든 실험에 대해, 순수 Cr 및 W이 함께 비교되었다. 기계적 특성 평가에는 3점 굽힘 시험기(3-point bending tester)가 활용되었으며, Cr의 DBTT 근처(300 °C)에서 W상에 의한 강화효과 및 Cr상이 지배하는 변형율에 따른 기계적 특성이 향상될 가능성이 내재하고 있음을 확인하였습니다. 일반적으로, 핵융합 환경에서 저방사화용 소재로 활용되기 위해서는 반드시 우수한 중수소 흡착 저항성을 갖추어야 한다. 그리고 이 같은 흡착 특성은 중성자 조사시 발생하는 나노결함으로 인해 더욱 가속화될 수 있으므로 활용 전 반드시 평가되어야 한다. 본 연구에서는 플라즈마 및 이온원 장비를 활용하여 중수소 이온을 조사하였으며, 표면 및 전체 샘플의 중수소 흡착량을 정량화하여 그 확산 거동을 이해하고자 하였다. Cr-W 이상 복합재료는 Cr상과 중수소의 높은 열역학적 안정성과 W 상 내 중수소의 느린 확산은 중수소 흡착량을 감소시키는데 큰 영

향을 줄 수 있는 가능성을 확인할 수 있었다. 또한, 중성자 유사 이온(W^{6+} 이온)을 선 조사하여 표면 나노결함 밀도를 증가시킨 샘플에 대해서도 해당 개념이 적용되어 순수 Cr 및 W 보다 낮은 중수소 흡착량이 관찰되었다.

이 연구를 통해, 차세대 핵융합로용 플라즈마 대면재로 제안 가능한 Cr-W 이상 복합재료를 처음으로 개발하고 이에 대한 근본적인 이해가 확립되었다. 해당 소재에 대한 포괄적인 연구 및 미세구조 디자인 전략과 그에 따른 잠재적 물성 확보는 신개념 소재 개발에 대한 중요한 가이드라인을 제공할 수 있을 것으로 기대하고 있다. 또한, W 및 Cr 소재의 C 확산 억제 현상에 대한 심층적인 이해는 C환경에서의 고순도 소재를 위한 제조 공정 기술 개발을 위한 주춧돌이 될 것이라 예상된다. 마지막으로, 본 연구의 개념은 다양한 극한환경 대응용 소재 분야에서 획기적인 진전을 가져오고 새로운 분야를 개척할 수 있는 원동력을 제공할 것으로 기대한다.

핵심어 : Cr-W 이상 복합재료, 통전 활성 소결, 확산, 탄소, 미세구조, 기계적 특성, 중수소 흡착, 확산

Student Number : 2015-20798